Microstructure, Macrostructure, and Cognition. A walk in Diffusion MRI

Demian Wassermann

Microstructure, Macrostructure, and Cognition. A walk in Diffusion MRI

Thesis by
Demian Wassermann

In Partial Fulfillment of the Requirements for the
Degree of
Habilitation à Diriger des Recherches

SORBONNE UNIVERSITÉ
Paris, France

2019

Demian Wassermann
ORCID: 0000-0001-5194-6056

Table of Contents

CHAPTER 1

INTRODUCTION

Finding the corporeal substrate of the mind constitutes one of science's prime goals since the inception of medicine and natural philosophy (Gross, 1998; Wassermann, 2010). The first records relating body with brain function have been attributed to Imothep through the Edwyn-Smith papyrus circa 3000 b.c. (see e.g. Breasted, 1930; Wilkins, 1964). Despite centuries of advances studying the brain's composition and structure, namely neuroanatomy, its relation with cognition remains elusive. The complexity of this programme remains hard to grasp, however, the number of discoveries has been propelled since the second half of the XX century. This acceleration is, in great proportion, due to the rapid development of tools, such as magnetic resonance imaging (MRI), to analyse the human brain structure and function *in vivo*.

Relating tissue and function, despite being as ancient an enterprise as it can be, has drastically changed its paradigm in the past 200 years. The late XIX century witnessed the development of a research program, led by personalities such as Meynert (1867), Brodmann (1909), and von Economo et al. (1925), which aimed at conciliating the teleological brain structure and function approach proposed by Gall et al. (1810) and Broca (1861), with the cellular structure of the brain. Such enterprise, grounded on Schleiden and Schwann's cell theory and its derivative the *neuron doctrine*, aspired to characterise brain function through the examination of its "indivisible" parts. The reduction of a complex system to a set of indivisible parts and the ambition that by characterising such parts the macroscopic organization will emerge is not an isolated idea of neuroscience. The epistemological current of methodological reductionism has been a prevalent approach in XIX and early XX century science. Such theory also establishes an interesting, yet arguable, hierarchy of sciences where, for instance, chemistry can be reduced to atomic physics, or molecular biology to chemistry (Anderson, 1972). Neuroscience, like most other sciences, has, and still is, experiencing benefits from such an

intellectual framework. An example this is the evidence that different spatial and visual representations can be traced to single neurons representing a point in the retina or geometrical borders (see e.g. Hubel et al., 1962; Marr, 1969; Solstad et al., 2008). However, methodological reductionism has proven to be limited to grasp the full complexity of the mind (see e.g. Searle, 2004), or even physics (Anderson, 1972), and analyses taking into account the complex network of interactions in brain structure have been propelled as the "novel" paradigm of connectomics (Catani et al., 2013) or, more generally, systems neuroscience (Uddin et al., 2010).

As a counterpoint to the reductionist view, there is an emerging trend based on conceiving the human brain as a *system* of interconnected components. Despite its perceived novelty, this trend is by no means new (Catani et al., 2013). However, the shift from the meticulous study of the elemental particles of a phenomenon towards the study of its *complex systems* of interactions has been common in XX-century science, with a notable examples in statistical mechanics (Boltzmann, 1867) and systems biology (Bertalanffy, 1928). The focus of systems biology is to address the limitations entailed by grounding a research strategy solely on the study of molecules, cells, and pathways in isolation (De Backer et al., 2010). In neuroscience, this can be traced to Meynert (1867) proposing the associationist theory of brain function and (Wernicke, 1874) using a network model to capture the nature of higher cognitive functions. However, it was not until the late XX century when neuroanatomists like Felleman et al. (1991) proposed a network-based organization of processing in the monkey brain, and Raichle et al. (2001) and Greicius et al. (2003) wielded network theory and functional MRI (fMRI) to coin the term *systems neuroscience*. The systems view of neuroscience, which encompasses network neuroscience (Bullmore et al., 2009) as well as connectomics (Behrens et al., 2012), is then the expression of a general scientific program on the neuroscience community. It has produced numerous novel ideas and conceptualizations of brain function and structure (Uddin et al., 2010; Yeo et al., 2016)

This dissertation focuses on the research I conducted since 2014, with brief mentions, when appropriate, of preceding work. Since 2010, some of my work can be inscribed in the reductionist paradigm, as well as some in the complex systems approach. As it is common in current neuroscience research, my work dwells between both intellectual frameworks. From the large number of current technologies to analyze the brain's structure and function, this dissertation will focus on MRI. Specifically, on dMRI (Stejskal et al., 1965), a technique that has been proposed, from the start, to statistically and non-invasively quantify microstructure (Tanner et al., 1968; Latour et al., 1994); to trace axonal connections (see e.g. Conturo et al., 1999; Basser et al., 2000); and to quantify the probability that an axonal pathway connects two brain regions (see e.g. Behrens et al., 2003a; Parker et al., 2005). diffusion weighted magnetic resonance imaging is thus, a rich tool allowing us to transit the path between the methodological reductionist microstructural analysis of the brain tissue to the systems view of the brain and its macrostructure. Can we go from the microstructure to cognition? Can we use macrostructural analyses to isolate brain structures and improve early diagnoses in neurological diseases? These are the main questions that this dissertation focuses on. Chapter 2 is centered on

the development of dMRI-based techniques to ease the quantification of tissue microstructure *in vivo*. Chapter 3 is centered on the developing methodologies to delineate the macrostructure of the brain. It makes a specific point on when the perceived macrostructure is thought to capture the systems aspect of microscopic brain properties, and when it is reflecting a human-based taxonomy which enables the study of more complex phenomena. Finally, Chapter 4 shows two selected applications of the methodologies portrayed in this dissertation, one linking tissue microstructure with cognition; one macrostructure with early diagnosis of Huntington's disease.

CHAPTER 2

Brain Microstructure with Diffusion MRI

Examining cellular architecture of living tissue with dMRI was first proposed by Tanner et al. (1968) when they used their novel protocols to examine the cellular structure of an apple and a tobacco pith. However, the first to propose it as a tool to examine morphological characteristics of human tissue architecture were presented simultaneously by Latour et al. (1994), where they used the short-time behaviour of the time-dependent diffusion coefficient ansatz proposed by Mitra et al. (1993) to obtain the average surface-to-volume ratio of human red blood cells; and by Van Gelderen et al. (1994), who used the Gaussian phase approximation (GPA) to obtain nerve diameters in an excised rabbit leg. Following these steps, Assaf et al. (2008) proposed AxCaliber as a method based on the narrow pulse approximation (NPA) (Stejskal et al., 1965) to measure axonal diameters *in vivo*, applied to rat's corpus callosum. After these first proposals, numerous methods to obtain cytoarchitectural measurements *in vivo* using dMRI were proposed (see e.g. Aggarwal et al., 2012; Zhang et al., 2013; Avram et al., 2016)

Despite these advancements, the feasibility of obtaining microstructural, be them cyto- or myeloarchitectural, measurements from diffusion MRI, has been brought into questions. Mainly through three main arguments: the first one, grounded in measurement theory, upholds that the signal attenuation induced from intra-axonal water is several orders of magnitude below available MRI scanner's signal-to-noise ratio (SNR)(see e.g. Burcaw et al., 2015; Lee et al., 2017; Veraart et al., 2019); the second one, based on inverse problem theory, is based on the degeneracy of the first family of proposed models leading to an infinite solution space and hence uninterpretable fitted parameters (see e.g. Jelescu et al., 2015); finally, the third one, which is microarchitecturally-based, upholds that dispersion and tortuosity in axons void the tube-modeling paradigm (see e.g. Nilsson et al., 2012; Ronen et al., 2014).

Two contributions are presented in this chapter, both aim at improving signal representation for dMRI.

Our first contribution adds regularization harmonic representation of the signal in when the sampling space is gradient strength, or equivalently q-space (Fick et al., 2016a). By adding a Tikhonov/Ridge regularisation in the harmonic space we are able to obtain two advantages: 1) cast the estimation problem into a convex optimization one increasing the stability and precision of the representation; 2) independently of the previously mentioned open questions in the field, we are able to reduce the dMRI acquisition requirements for different microstructure estimation models.

Our second contribution extends the first one to the cross-product space between gradient strength and diffusion time (Fick et al., 2018b). The addition of the diffusion time dimension enables the extraction of finer micro- and meso-architecture traits (see e.g. Latour et al., 1994; Novikov et al., 2014). In this contribution, we wield tools from machine learning and/or compressive sensing to tame the parameter increase as well as the stability. Our method enables us to extract indices from the diffusion-time dMRI signal in a reproducible manner, as well as conceive a method to reduce the prohibitive acquisition time for such experiments (Filipiak et al., 2018).

In the following, we briefly introduce the nuts and bolts of the dMRI signal physics, followed by our two contributions. We leave the applications of such contributions to the analysis of the relationship between brain tissue (micro)structure and function to Chapter 4.

2.1 Background: The Diffusion MRI Signal

Diffusion encoding in MRI extends the Spin-Echo experiment proposed by Hahn (1950) and Carr et al. (1954) by using time-dependent field gradients to characterize spin diffusion (Stejskal et al., 1965). Through this characterization, nuclear magnetic resonance (NMR), and then MRI, can be used to characterize the self-diffusion coefficient of a fluid (Stejskal et al., 1965) as well as, in the case of restricted or hindered diffusion, the microscopic structure of where spins are confined (Tanner et al., 1968). Specifically, the pulsed field gradient diffusion encoding, induces an attenuation E on the T_2 (Stejskal et al., 1965) or T_1 (Frahm et al., 1985) decay which can be summarizes through its dependence on the amplitude and direction of the gradient vector $\mathbf{G}$, the length of the pulse, δ, and the pulse separation Δ. For the case of free diffusion, the induced attenuation is characterized by the simple formula (Stejskal et al., 1965):

$$\log E(\mathbf{G}, \delta, \Delta) = -(\|\mathbf{G}\|_2 \gamma \delta)^2 (\Delta - \delta/3) D \in \mathbb{R}, \tag{2.1}$$

with γ the gyromagnetic ratio of the spin and D the self-diffusion coefficient. However, to find closed formulae for the case of restricted, and hindered, diffusion, even in simple geometries, more hypotheses are required.

The first proposed approximation, currently known as narrow pulse approximation (NPA), is based on the hypothesis that the pulse length δ is short enough, such that the contribution to the dMRI signal

attenuation of spin diffusion during the pulse is negligible. This leads to the relationship:

$$E(\mathbf{G}, \delta, \Delta) = \iint \rho(\mathbf{r}_0) P(\mathbf{r}_0|\mathbf{r}, \Delta - \delta/3) \exp\left[i\mathbf{G}\gamma\delta(\mathbf{r} - \mathbf{r}_0)\right] d\mathbf{r}_0 d\mathbf{r} \tag{2.2}$$

where $\mathbf{r}_0$ and $\mathbf{r}$ are the initial and final position of a given spin after a diffusion time $\Delta - \delta/3$, ρ is the probability density function of initial spin positions and P is the probability that a spin had an initial position $\mathbf{r}_0$ given that its position after the diffusion time is $\mathbf{r}$. Then, taking $\mathbf{q} = \frac{1}{2\pi}\mathbf{G}\delta\gamma$, fixing δ, and $\Delta\mathbf{r} = \mathbf{r} - \mathbf{r}_0$, Equation (2.2) becomes (Kärger et al., 1983; Callaghan et al., 1988)

$$\begin{aligned} E(\mathbf{q}, \Delta) &= \int \mathbb{E}_{\mathbf{r}_0}\left[P(\mathbf{r}_0|\Delta\mathbf{r} - \mathbf{r}_0; \Delta - \delta/3)\right] \exp(-i\mathbf{q}\Delta\mathbf{r}) d\Delta\mathbf{r} \\ &= \int \bar{P}(\Delta\mathbf{r}; \Delta - \delta/3) \exp(-i\mathbf{q}\Delta\mathbf{r}) d\Delta\mathbf{r} \end{aligned} \tag{2.3}$$

hence E is the Fourier transform of the probability density function of net spin displacement $\Delta\mathbf{r}$ averaged over all initial positions $\mathbf{r}_0$, namely the Fourier transform of the ensemble average propagator (EAP) $\bar{P}$. For perfectly reflecting boundaries, this expression has an analytical formulation (Tanner et al., 1968; Callaghan et al., 1990; Cory, 1990)

$$E(\mathbf{q}, \Delta) = \sum_i \exp\left(-\beta_i \frac{D(\Delta - \delta/3)}{L^2}\right) B_i(\mathbf{q}, L) \tag{2.4}$$

where L is the characteristic length of the pore containing the spins along the direction of $\mathbf{q}$, and β_i and B_i depend on the eigendecomposition of Laplace's operator in a domain having the same shape as the pore containing the spins.

The second approximation, known as GPA, is based on the hypothesis that δ is short enough such that in that time most spins diffuse following a free water regime, i.e. these don't encounter any restriction (Murday et al., 1968; Neuman, 1973). Albeit less synthetic, this approximation agrees better with the experimental conditions for dMRI in living tissue as the ratio between the self-diffusion coefficient of the water in the tissue, δ, and cellular morphology is closer to the GPA hypothesis than the NPA one (Avram et al., 2008). The GPA approximation leads, through similar modeling, to the analytical expression for restricted geometries (Murday et al., 1968; Balinov et al., 1993; Van Gelderen et al., 1994)

$$E(\mathbf{G}, \delta, \Delta) = \exp\left(-\gamma^2 \|\mathbf{G}\|_2^2 \sum_i C_i(D, L, \delta, \Delta)\right), \tag{2.5}$$

where C_i depends on eigendecomposition of Laplace's operator in a domain having the same shape as the pore containing the spins.

The presented formalisms allow us to characterise boundary conditions of the diffusion signal under fixed δ and variable $\{\mathbf{G}, \Delta\}$:

- $\{\mathbf{G} \in \mathbb{R}^3, \Delta = 0\}$: When $\Delta = 0$ the spins have no time to diffuse and the EAP is a spike function at the origin, i.e, $\bar{P}(\Delta\mathbf{r}; \Delta = 0) = \delta(\Delta\mathbf{r})$ with δ only here the Dirac delta function.

Following Equation (2.3), the signal attenuation will not attenuate for any value of $\mathbf{G}$, i.e., $E(\mathbf{G}, \delta, \Delta = 0) = 1$.

- $\{\mathbf{G} \in \mathbb{R}^3, \Delta \rightarrow 0\}$: In the limit of very short times, spins diffuse either freely or in contact with restriction boundaries. In this case, the surface-to-volume ratio of containing pore and self-diffusion times can be computed from the signal (Mitra et al., 1992b, 1993).

- $\{\mathbf{G} \in \mathbb{R}^3, \Delta \rightarrow \infty\}$: In the case of long diffusion time, only signal contributions from restricted compartments remain (Callaghan, 1995). In this case, given infinite gradient strength, the NPA, and some assumptions on tissue composition, q-space indices to microstructural sizes (Özarslan et al., 2013; Fick et al., 2016b).

- $\{\mathbf{G} = 0, \Delta > 0\}$: When there is no diffusion sensitization then $E(\mathbf{G} = 0, \delta, \Delta) = 1$. With the Fourier relationship in Equation (2.3), this point also corresponds to the zeroth harmonic of the EAP, which as a probability density integrates to one.

- $\{\mathbf{G} \rightarrow \infty, \Delta \in \mathbb{R}^+\}$: In the case of very strong gradients even an infinitesimally small spin movement will attenuate the signal completely. This means that only trapped water particles still contribute to the signal attenuation. In *ex-vivo* tissues, a significant signal contribution of trapped water has been found (Alexander et al., 2010), meaning $\lim_{\mathbf{G}\rightarrow\infty} E(\mathbf{G}, \delta, \Delta) = f_{\text{trapped}}$ with f_{trapped} the trapped water volume fraction. In *in-vivo* tissues, this contribution has been found to be negligible (Veraart et al., 2019), meaning $\lim_{\mathbf{G}\rightarrow\infty} E(\mathbf{G}, \delta, \Delta) = 0$.

It's worth noting that more general approximations to the signal attenuation in simple geometries and for generic pulse shapes have been recently developed (see e.g. Grebenkov, 2008; Grebenkov, 2009). However, for the sake of this manuscript, the NPA and GPA will suffice as approximations for the dMRI signal in simple geometries.

2.2 Tissue Microstructure from the dMRI signal integral operators

Since the introduction of rotationally invariant measurements by Basser et al. (1996), a large part of the research program in dMRI has been to link the tissue structure of the living human brain with the dMRI signal (see e.g. Song et al., 2005; Alexander, 2008; Lebel et al., 2008; Zhang et al., 2013; Novikov et al., 2014). The diffusion tensor imaging (DTI)-based measures have shown to be sensitive but not specific enough to breach the level of detail needed for elucidating a close relationship between tissue structure and function except in some specific cases (see e.g. Assaf et al., 2002; Wang et al., 2011b). This lead to the birth of several alternatives based on more extensive sampling schemes of the diffusion space (see the reviews by Fick et al., 2017; Novikov et al., 2018a). However, the predominant take on such enterprise has been through solving ill-conditioned, and generally degeneracy-plagued, inverse models (Novikov et al., 2018a).

The pervasive degeneracy of inverse models for dMRI-based tissue microstructure estimation motivated the research program that we have pursued during the past years: to access tissue microstructure measurements through forward models, specifically integral operators of the dMRI signal in $\mathbf{q}$-space (see e.g. Mitra et al., 1995; Commowick et al., 2015; Novikov et al., 2018b). The first of these to be proposed, to the best of our knowledge, has been the RTOP. Mitra et al. (1995) defined RTOP as the probability that after a diffusion time τ a particle returns to its origin, i.e. $\Delta\mathbf{r} = 0$ according to the EAP definition in Equation (2.3). Furthermore, they showed that it is a measurement capable of quantifying the microstructure of porous structures. The earliest proposal of using RTOP as a biomarker can be attributed to King et al. (1994), Assaf et al. (2002), and Cohen et al. (2002), however it is only recently that dMRI protocols enable development and application of these measurements in high-resolution large-scale samples (see e.g. Setsompop et al., 2013). A fundamental advantage of this measure comes from its straightforward definition

$$\mathrm{RTOP}(\tau) \triangleq \bar{P}(0;\tau) = \int_{\mathbb{R}^3} d\mathbf{q} E(\mathbf{q},\tau), \quad \text{with } \tau = \Delta - \delta/3 \quad [\mathrm{m}^{-3}], \tag{2.6}$$

which implies that it is computable through a numerical integral on the dMRI signal. Under proper experimental conditions, e.g. relative maximum $\mathbf{q}$ with respect to the microstructure scale, RTOP is sensitive and specific to average pore volume, surface-to-volume ratio, and connectivity (Mitra et al., 1992a). All this, without the hassle of solving inverse models.

Recently other, less studied, measurements based on integral operators of the dMRI signal have been proposed (e.g. Commowick et al., 2015; Novikov et al., 2018b). Of these, Özarslan et al. (2013) proposed two derivations from RTOP: the return to axis probability (RTAP) and return to plane probability (RTPP). Formally, for a given unitary vector $\hat{\mathbf{r}}$, these are defined as

$$\mathrm{RTAP}(\tau;\hat{\mathbf{r}}) \triangleq \int_{\mathbb{R}} d\Delta r \bar{P}(\Delta r\hat{\mathbf{r}};\tau) \quad [\mathrm{m}^{-2}] \tag{2.7}$$

$$\mathrm{RTPP}(\tau;\hat{\mathbf{r}}) \triangleq \int_{\mathbb{R}^2} d\Delta\mathbf{r} \bar{P}(\Delta\mathbf{r}\cdot\hat{\mathbf{r}}_\perp;\tau) \quad \text{s.t.} \quad \hat{\mathbf{r}}_\perp\cdot\hat{\mathbf{r}} = 0,\ \|\hat{\mathbf{r}}_\perp\| = 1 \quad [\mathrm{m}^{-1}]. \tag{2.8}$$

When $\frac{1}{\mathbf{q}_{max}}$ is smaller than half the pore length in the $\hat{\mathbf{r}}$ direction and τ more than triples the time to diffuse across such length, RTAP quantifies the cross-sectional surface of the pores, e.g. the diameter of a set of aligned tubes with principal direction $\hat{\mathbf{r}}$. For equivalent experimental conditions, RTPP quantifies the length of these tubes if they are capped. Furthermore, mean squared displacement (MSD) measurement, which was recently borrowed from statistical mechanics (Wu et al., 2007),

$$\mathrm{MSD}(\tau) \triangleq \int_{\mathbb{R}^3} d\Delta\mathbf{r} \bar{P}(\Delta\mathbf{r};\tau)\|\Delta\mathbf{r}\|_2^2 \quad [\mathrm{m}^2] \tag{2.9}$$

quantifies, as its name states, the average displacement of particles for a given diffusion time τ.

To ease the requirements and reduce the noise influence of tissue microstructure estimation by means of dMRI indices based on integral operators of the signal, we developed two signal representation

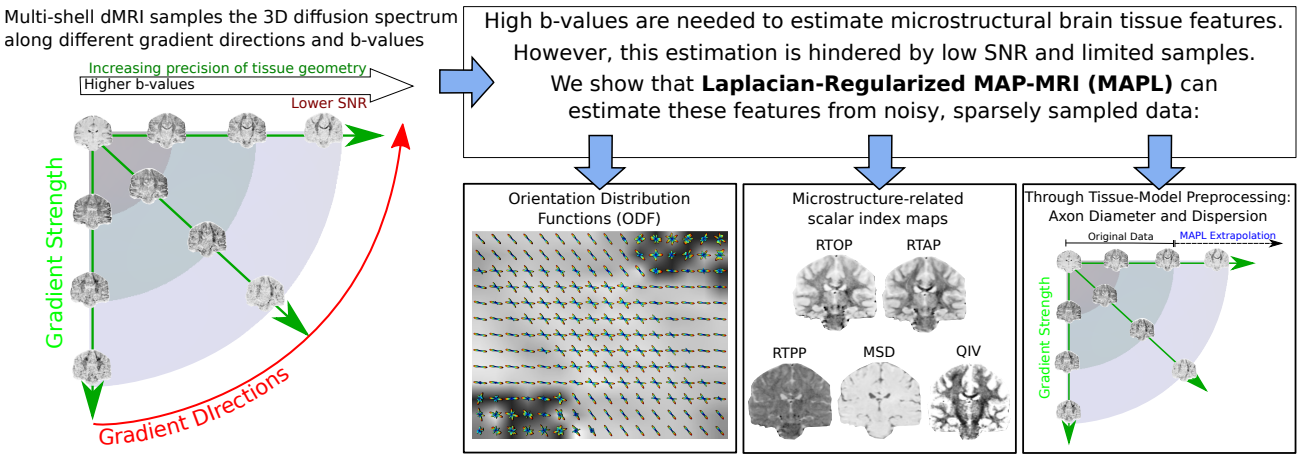

Figure 2.1: Visual abstract of the first contribution. On the left, we illustrate multi-shell dMRI, where diffusion-weighted images (DWIs) are measured along different gradient directions and b-values. DWIs at higher b-values (using strong gradients) provide information on smaller details in the tissue geometry, but also have lower SNR. We show that using Laplacian-Regularized MAP-MRI (MAPL) we can accurately estimate valuable microstructure features from noisy, subsampled data (bottom row).

methods: one for the analysis of dMRI images sampling q-space; and one for qτ-space images. Both are based on q-space representation of the dMRI space proposed by Callaghan et al. (1990), and based in the NPA approximation. Despite our goal being focused on forward models, we show that our contributions are also effective to improve inverse models.

2.3 First Contribution: Laplacian-Regularised dMRI signal representation in q-space

We improve EAP and q-space index estimation by regularizing the coefficient estimation of the mean apparent propagator imaging (MAP-MRI) functional basis (Özarslan et al., 2013) with the Laplacian of the reconstructed signal. We call our Laplacian-regularized MAP-MRI approach MAPL for brevity. In dMRI, this type of regularization has successfully been applied to several other techniques (see e.g. Descoteaux et al., 2007). We provide a brief summary of the MAP-MRI basis in Section 2.3.1, present our proposed Laplacian regularization in Section 2.3.2, and explain the generalized cross-validation (GCV) method to find optimal regularization weights in Section 2.3.3. This contrubtion is summarised in Figure 2.1.

We aim at representing the measured $\mathbf{q}$-signal attenuation $E(\mathbf{q}, \Delta)$ or $E(\mathbf{q})$ for brevity as Δ is fixed in this case, in terms of a continuous functional basis $\hat{E}_{\mathbf{c}}(\mathbf{q})$. Hence, we represent the attenuation in terms of coefficients $\mathbf{c} \in \mathbb{R}^{N_{\text{coef}}}$ with N_{coef} the number of coefficients. An effective representation $\hat{E}_{\mathbf{c}}(\mathbf{q})$ should be able to

1. closely approximate the measured $\mathbf{q}$-signal attenuation,

2. smoothly interpolate between and outside the measured $\{\mathbf{q}\}$ points,

3. and be able to reconstruct the EAP from the fitted signal.

In this work we propose to satisfy requirements 1–3 by finding the coefficients of the signal representation model and enforcing smoothness through Laplacian regularization, specifically by solving the convex problem:

$$\begin{aligned} &\operatorname{argmin}_{\mathbf{c}} \overbrace{\int_{\mathbb{R}^3} \left\| E(\mathbf{q}) - \hat{E}_{\mathbf{c}}(\mathbf{q}) \right\|_2^2 d\mathbf{q}}^{\text{(1) Data Fidelity}} + \lambda \overbrace{\int_{\mathbb{R}^3} \left\| \nabla_{\mathbf{q}}^2 \hat{E}_{\mathbf{c}}(\mathbf{q}) \right\|_2^2 d\mathbf{q}}^{\text{(2) Smoothness}} \\ &\text{subject to } \hat{E}_{\mathbf{c}}(0) = 1 \end{aligned} \tag{2.10}$$

with λ and α regularization weights. As stated in Section 2.1, the boundary constraints are important to respect the Fourier relationship between the fitted signal attenuation and the EAP. We now proceed to describe the representation model which was proposed by (Özarslan et al., 2013) and then detail our contribution which is the analytical Laplacian regularization.

2.3.1 MAP-MRI Functional Basis Description

MAP-MRI is a functional basis that reconstructs the EAP from the dMRI signal. It has the convenient property that its basis functions are eigenvectors of the Fourier transform. For this reason, it can describe both the signal and the EAP with the same coefficients as

$$\hat{E}_{\mathbf{c}}(\mathbf{q}) = \sum_i c_i \Phi_{N_i}(\mathbf{q}) \quad \text{and} \quad \bar{P}(\Delta\mathbf{r}) = \sum_i c_i \Psi_{N_i}(\Delta\mathbf{r}) \tag{2.11}$$

where $\Psi = \text{IFT}(\Phi)$ and $\{c_i\}$ are the basis coefficients. The basis functions for the signal attenuation and the EAP, left and right side of Equation (2.11) respectively, are given as products of three orthogonal one-dimensional basis functions, which are known as Simple Harmonic Oscillator based Reconstruction and Estimation (SHORE) functions Özarslan et al. (2013). For the signal attenuation they are given as

$$\begin{aligned} \Phi_{n_1 n_2 n_3}(\mathbf{A}, \mathbf{q}) &= \phi_{n_1}(u_x, q_x)\phi_{n_2}(u_y, q_y)\phi_{n_3}(u_z, q_z) \\ \text{with } \phi_n(u, q) &= \frac{i^{-n}}{\sqrt{2^n n!}} e^{-2\pi^2 q^2 u^2} H_n(2\pi u q). \end{aligned} \tag{2.12}$$

and for the EAP as

$$\begin{aligned} \Psi_{n_1 n_2 n_3}(\mathbf{A}, \Delta\mathbf{r}) &= \psi_{n_1}(u_x, R_x)\psi_{n_2}(u_y, R_y)\psi_{n_3}(u_z, R_z) \\ \text{with } \psi_n(u, R) &= \frac{1}{\sqrt{2^{n+1}\pi n! u}} e^{-R^2/(2u^2)} H_n(R/u) \end{aligned} \tag{2.13}$$

where H is a Hermite polynomial of order n and $\psi = \text{IFT}(\phi)$. The fitting of the MAP-MRI signal basis is then not performed in the regular "image space" – that does not change from voxel to voxel – but in voxel-dependent "anatomical space" (Özarslan et al., 2013). In this anatomical space the $\mathbf{q}$-space vectors of the data (and therefore the data itself) has been rotated such that the main eigenvectors of an

estimated DTI tensor (Basser et al., 1994) coincide with the axes of the Cartesian coordinate system $\{x, y, z\}$. The eigenvalues of the DTI tensor are then used to set the stiffness of the oscillator in each direction (i.e. $\{u_x, u_y, u_z\}$). In this way the anisotropy of MAP-MRI's basis functions depends on the anisotropy of the data as estimated by a DTI tensor.

The data-dependent anisotropic scaling lies at the heart of MAP-MRI. However, if the scaling is chosen isotropic ($u_x = u_y = u_z$) the mean apparent propagator imaging (MAP-MRI) basis corresponds to the 3D-SHORE basis (Özarslan et al., 2013). The 3D-SHORE basis is thus a particular case of MAP-MRI where the bases in Eqs. (2.12) and (2.13) have been rewritten as a product of a radial oscillator and angular spherical harmonics. In the experiments of this work we will compare the Cartesian (anisotropic) and spherical (isotropic) implementations of MAP-MRI, but in the theory here we will only consider the 'regular' Cartesian implementation. We provide the derivations of scalar measures and Laplacian regularization for the spherical implementation in (Fick et al., 2016a).

2.3.2 Closed-Form Laplacian Regularization

In this section, we provide the formulation of our proposed Laplacian-regularized MAP-MRI. We call this approach MAPL for brevity. In MAPL, we fit MAP-MRI's basis functions to noisy data by first casting the coefficients into an N_{coef}-dimensional vector $\mathbf{c}$ and the signal values in an N_{data}-dimensional vector $\mathbf{y}$. Design matrix $\mathbf{Q} \in \mathbb{R}^{N_{\text{data}} \times N_{\text{coef}}}$ then has elements $\mathbf{Q}_{ij} = \Phi_{N_i}(2\mathbf{D}(\Delta - \delta/3), \mathbf{q}_j)$, with $\mathbf{D}$ the DTI tensor estimation of the signal. The coefficients $\mathbf{c}$ (recall Eq. (2.11)) are found by minimizing the quantity $\mathbf{c} = \text{argmin}_{\mathbf{c}} \|\mathbf{y} - \mathbf{Q}\mathbf{c}\|^2 + \lambda\, U(\mathbf{c})$ where λ weights our Laplacian regularization functional

$$U(\mathbf{c}) = \int_{\mathbb{R}^3} \|\nabla^2 \hat{E}_{\mathbf{c}}(\mathbf{q})\|^2 d\mathbf{q} \tag{2.14}$$

with $\nabla^2 E_{\mathbf{c}}(\mathbf{q}) = \sum_i c_i \nabla^2 \Phi_{N_i}(\mathbf{q})$ the Laplacian of the reconstructed signal. We then express $U(\mathbf{c})$ as a summation of MAP-MRI basis functions

$$U(\mathbf{c}) = \int_{\mathbb{R}^3} \left(\sum_i c_i \nabla^2 \Phi_{N_i}(\mathbf{q}) \right)^2 d\mathbf{q} = \sum_i \sum_k c_i c_k \int_{\mathbb{R}^3} \nabla^2 \Phi_{N_i}(\mathbf{q}) \cdot \nabla^2 \Phi_{N_k}(\mathbf{q})\, d\mathbf{q} \tag{2.15}$$

where the subscripts i and k indicate the basis order of the i-th or k-th basis function $\Phi_{N_i}(\mathbf{q}) = \Phi_{n_1 n_2 n_3(i)}(\mathbf{q})$. We write the summations in quadratic form such that $U(\mathbf{c}) = \mathbf{c}^{\mathsf{T}}\mathbf{U}\mathbf{c}$ where regularization matrix $\mathbf{U}$ has elements

$$\mathbf{U}_{ik} = \int_{\mathbb{R}^3} \nabla^2 \Phi_{N_i}(\mathbf{q}) \cdot \nabla^2 \Phi_{N_k}(\mathbf{q}) d\mathbf{q}. \tag{2.16}$$

We solve the coefficients of the matrix U analytically in Fick et al. (2016a). Using this formulation we obtain the regularized MAP-MRI coefficients using penalized least squares with unique minimum:

$$\mathbf{c} = (\mathbf{Q}^{\mathsf{T}}\mathbf{Q} + \lambda \mathbf{U})^{-1} \mathbf{Q}^{\mathsf{T}} \mathbf{y}. \tag{2.17}$$

2.3.3 Optimal Weighting Parameter Choice

To find optimal regularization weights λ in Eq (2.17) we use the Generalized Cross Validation (GCV) algorithm. GCV is based on an N_{data}-fold cross validation. Fortunately, the estimation of λ can be calculated as the minimum argument of the GCV function

$$GCV(\lambda, \mathbf{y}) = \frac{\|\mathbf{y} - \hat{\mathbf{y}}_\lambda\|}{N_{\text{data}} - Tr(\mathbf{S}_\lambda)} \tag{2.18}$$

where $\mathbf{S}_\lambda = \mathbf{Q}(\mathbf{Q}^\mathsf{T}\mathbf{Q} + \lambda\mathbf{U})^{-1}\mathbf{Q}^\mathsf{T}$ is the smoother matrix and $\hat{\mathbf{y}}_\lambda = \mathbf{S}_\lambda\mathbf{y}$.

2.3.4 Experiments and Discussion

In this section we detail three most important results supporting the applicability of our technique: first, it improves multi-shell signal reconstruction; second, it can be used as an effective preprocessing tool for multi-compartment models; third we show that MAPL-obtained RTOP is modulated by average cell size, in simulations and on the insular macaque cortex. For a more in-detail analysis of MAPL's properties, such as orientation distribution function (ODF) estimation and comparison with the state of the art we refer the reader to our published work by Fick et al. (2016a).

MAPL Improves Signal Reconstruction

A key feature of MAP-MRI is its use of anisotropic basis functions. We analyse the performance of MAPL as a reconstruction method, by comparing it with MAP on the SPARC phantom data (Ning et al., 2015). In doing this we show, in Figure 2.2, that this feature indeed reduces the fitting error for lower radial orders compared to the isotropic version of MAP-MRI (also known as 3D-SHORE). MAPL also has a great speed advantage over positivity constrained MAP-MRI (Özarslan et al., 2013), especially when presetting the regularization weight, see Figure 2.2(d). Isotropic MAPL is still over 4 times faster than the anisotropic implementation due to the omission of basis rotations.

MAPL Reduces The Variance in Multi-Compartment Tissue Model Estimation

To estimate microstructural tissue properties such as axonal dispersion, the signal contributions from different tissue compartments must be considered (e.g. Zhang et al., 2013). In this work, we used MAPL's signal extrapolation as a preprocessing to estimate axonal dispersion and the NODDI model from a multi-shell protocol at fixed diffusion time $\Delta - \delta/3$.

For this we take the $b_{\text{max}} = 10,000\text{s/m}^2$ dataset from the human connectome project (HCP) database (Sotiropoulos et al., 2013) and estimate the NODDI model with and without MAPL preprocessing on three sections of the corpus callosum. We use the dataset up to $b_{\text{max}} = 10,000\text{s/m}^2$ as ground truth and we analyse the results as we reduce b_{max} and the number of dMRI **q**-shells.

Our results on the estimation of axonal dispersion (ODI) using NODDI and MAPL + NODDI are given in Figure 2.3 and Table 2.3. We observe that increasing the maximum b-value increases the average ODI estimation (by about 1–1.5 standard deviations per jump in b-value) while leaving its

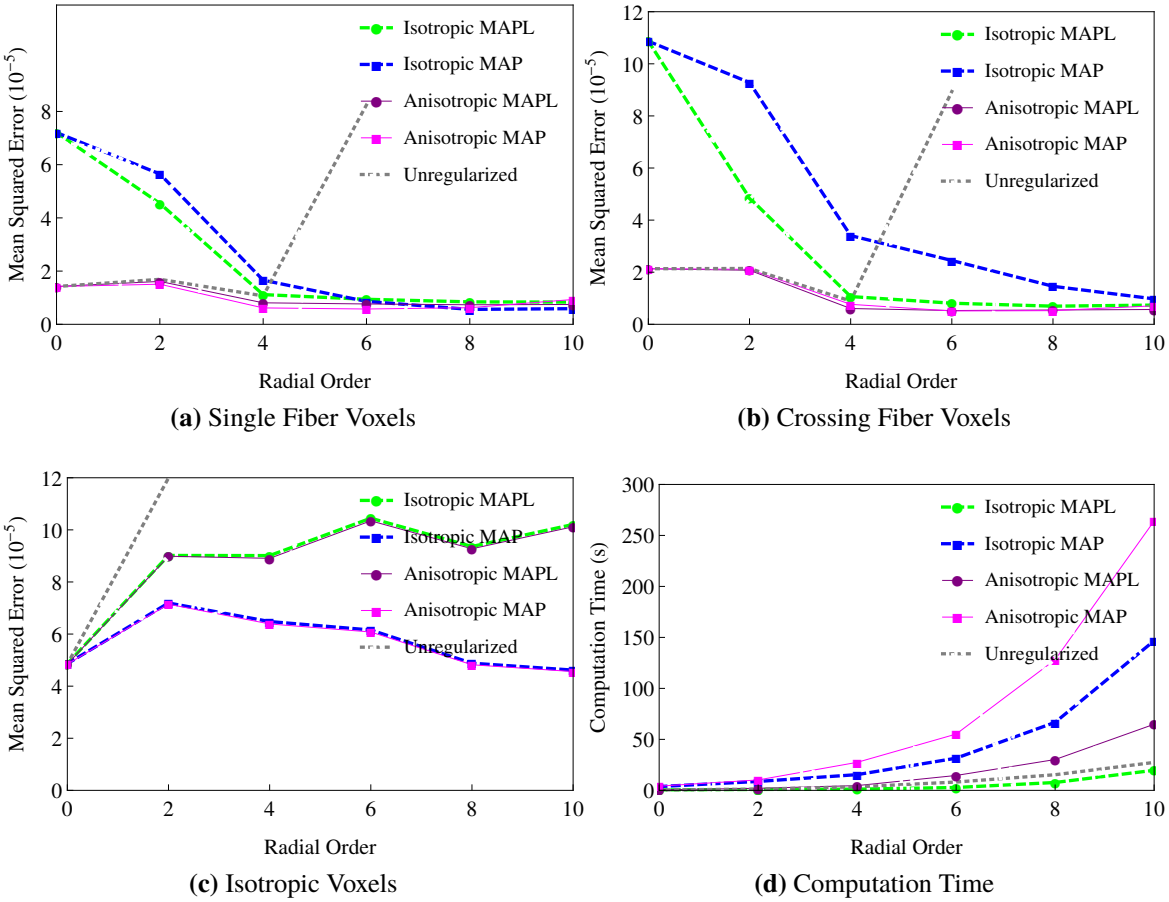

(a) Single Fiber Voxels

(b) Crossing Fiber Voxels

(c) Isotropic Voxels

(d) Computation Time

Figure 2.2: The mean squared error of the reconstructed signal with respect to the ground truth signal. A separation is made for voxels containing one fiber (a), two crossing fibers (b) or isotropic diffusion (c). In (d) the computation time in seconds for every regularization method is given.

standard deviation relatively stable. At the same time in restricted volume fraction also increases (result not shown). When we repeat the same experiment using synthetic data with known ground truth ODI and restricted volume fraction we find the same effect with increasing b-value, but that the results at $b_{\max} = 3,000\,\mathrm{s/mm^2}$ are closest to the ground truth (result not shown). It is possible that the combination of lower SNR at higher b-values or the sampling scheme cause this effect, but from the results here we cannot point to the exact cause.

When we enhance the estimation using MAPL + NODDI the results change in two ways: (1) The ODI estimation stabilizes over b-value around $b_{\max} = 5,000\,\mathrm{s/mm^2}$ result for NODDI and (2) the standard deviation decreases between 25% to 50%. The mean ODI between different sections often comes closer together, but this is in proportion to the decrease in standard deviation. We also find a slightly decreased estimation of the restricted volume fraction compared to NODDI (result not shown).

Overall, these results are meant as an initial exploration into the use of regularised functional basis approaches such as MAPL as a complementary technique to multi-compartment tissue models, rather

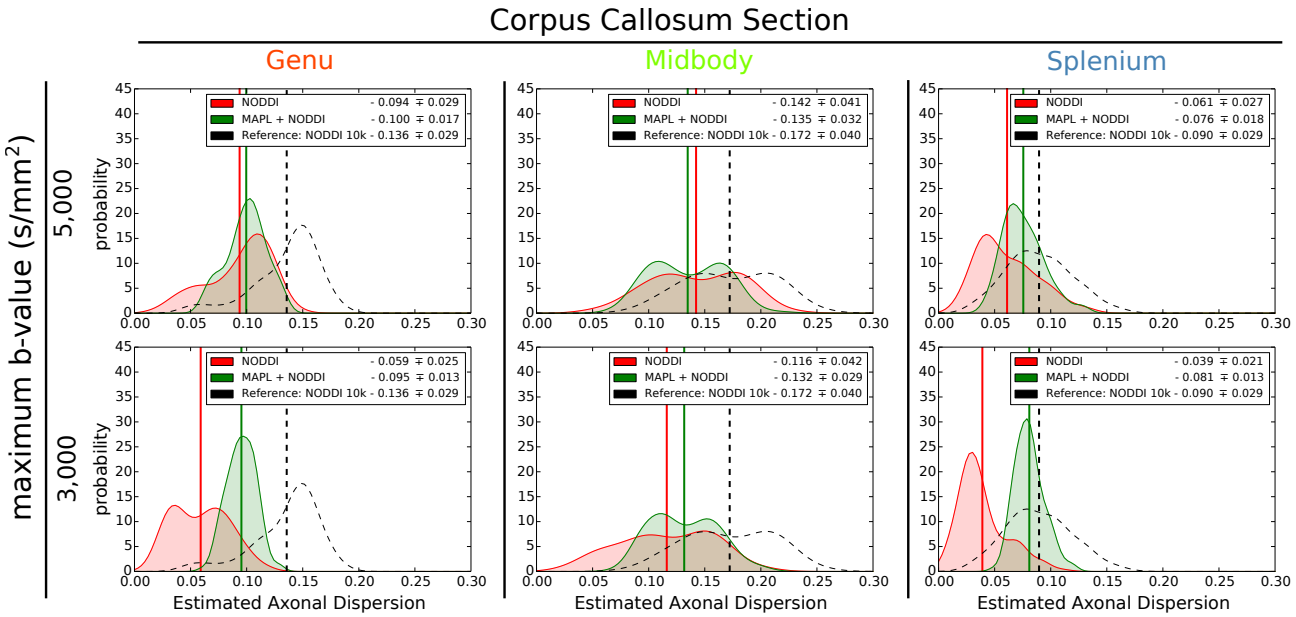

Figure 2.3: The estimated axonal dispersion using either only NODDI (red) or our MAPL + NODDI method (green) on subject 6 of the MGH-HCP data. The estimation of done for different maximum b-values and sections of the Corpus Callosum. The black dotted line is the reference reconstruction using the full data with $b_{\max} = 10,000\,\text{s/mm}^2$. Our combined approach always has a lower standard deviation than the regular NODDI approach.

than a competing technique. Reducing the variability of tissue parameter estimation in this way could increase the statistical power of population tests and the clinical applicability of this approach should be investigated in further studies.

A raising trend in microstructure characterisation has been proposed by Burcaw et al. (2015) among others, who showed that when estimating the axon diameter using multiple diffusion times it is necessary to take into account the time-dependence of the extra-axonal diffusion signal, which biases the estimation even at the long diffusion time limit. Mesoscopic effects, i.e. effects of spatial arrangement, as well as correlations and structural disorder in axon packing should also be considered. To overcome the limitation of MAP-MRI with respect to fitting multiple diffusion times, we proposed an extension of MAP-MRI that is able to simultaneously represent the diffusion signal over both q-space and diffusion time which we present in the next section (Fick et al., 2018a).

Table 2.3: Tables of estimated axonal dispersion values for 6 subjects of the MGH-HCP data set. Estimates are made on the same segmentations of the Corpus Callosum as Figure 11, using either NODDI or our MAPL + NODDI hybrid.

Subject 1			Section	
		Genu	Midbody	Genu
Method	b_{max}(s/mm^2)	ODI	ODI	ODI
NODDI	3,000	0.074±0.030	0.129±0.033	0.101±0.028
	5,000	0.107±0.031	0.156±0.032	0.143±0.024
	10,000	0.152±0.028	0.189±0.034	0.184±0.024
MAPL + NODDI	3,000	0.109±0.017	0.146±0.024	0.124±0.019
	5,000	0.106±0.020	0.148±0.027	0.129±0.021
	10,000	0.110±0.023	0.156±0.032	0.133±0.024

Subject 2			Section	
		Genu	Midbody	Genu
Method	b_{max}(s/mm^2)	ODI	ODI	ODI
NODDI	3,000	0.059±0.025	0.116±0.042	0.039±0.021
	5,000	0.094±0.029	0.142±0.041	0.061±0.027
	10,000	0.136±0.029	0.172±0.040	0.090±0.029
MAPL + NODDI	3,000	0.095±0.013	0.132±0.029	0.081±0.013
	5,000	0.100±0.017	0.135±0.032	0.076±0.018
	10,000	0.095±0.021	0.132±0.038	0.071±0.019

Subject 3			Section	
		Genu	Midbody	Genu
Method	b_{max}(s/mm^2)	ODI	ODI	ODI
NODDI	3,000	0.053±0.021	0.085±0.039	0.086±0.033
	5,000	0.084±0.023	0.103±0.043	0.119±0.033
	10,000	0.120±0.022	0.127±0.046	0.155±0.032
MAPL + NODDI	3,000	0.096±0.013	0.112±0.026	0.114±0.020
	5,000	0.097±0.015	0.109±0.031	0.116±0.024
	10,000	0.095±0.018	0.110±0.038	0.119±0.027

Subject 4			Section	
		Genu	Midbody	Genu
Method	b_{max}(s/mm^2)	ODI	ODI	ODI
NODDI	3,000	0.040±0.019	0.085±0.033	0.096±0.021
	5,000	0.069±0.029	0.114±0.033	0.136±0.015
	10,000	0.122±0.036	0.152±0.033	0.176±0.015
MAPL + NODDI	3,000	0.091±0.015	0.115±0.020	0.117±0.013
	5,000	0.081±0.017	0.112±0.023	0.125±0.014
	10,000	0.074±0.023	0.111±0.027	0.129±0.015

Subject 5			Section	
		Genu	Midbody	Genu
Method	b_{max}(s/mm^2)	ODI	ODI	ODI
NODDI	3,000	0.058±0.026	0.067±0.044	0.057±0.024
	5,000	0.090±0.027	0.081±0.054	0.077±0.031
	10,000	0.147±0.022	0.103±0.061	0.105±0.035
MAPL + NODDI	3,000	0.103±0.015	0.102±0.032	0.093±0.014
	5,000	0.097±0.016	0.094±0.040	0.087±0.019
	10,000	0.104±0.021	0.091±0.047	0.081±0.025

Subject 6			Section	
		Genu	Midbody	Genu
Method	b_{max}(s/mm^2)	ODI	ODI	ODI
NODDI	3,000	0.055±0.023	0.079±0.040	0.043±0.025
	5,000	0.084±0.027	0.106±0.039	0.069±0.034
	10,000	0.130±0.025	0.139±0.039	0.105±0.039
MAPL + NODDI	3,000	0.100±0.015	0.113±0.024	0.088±0.018
	5,000	0.095±0.018	0.109±0.028	0.081±0.021
	10,000	0.097±0.018	0.109±0.034	0.078±0.026

RTOP is sensitive to neuronal size

To assess that dMRI and RTOP, in our experimental conditions, is sensitive to the presence of Von Economo neuron (VEN) and pyramidal neurons, we show analytically, through morphometric modelling simulations, and in an animal model, that the dMRI signal at the acquisition parameters of clinical and pre-clinical MRI scanners, and specifically the HCP acquisition parameters, furthermore that its decay scales with the soma's internal volume.

To assess the feasibility of obtaining a measurement related to neuronal size we performed a theoretical analysis. We analyzed the raw dMRI signal RTOP on VEN and pyramidal neurons. For this, we used the GPA model introduced in Section 2.1 to simulate dMRI acquisitions within a sphere in order to investigate whether the raw dMRI signal and RTOP are sensitive to the presence of large neurons. We assumed two samples of spherical volumes in agreement to the measurements by Evrard et al. (2012) of neuronal somas within the human fronto-insular cortical area: $15,347 \pm 2,954$ μm for VEN, and $5,226 \pm 1,401$ μm for pyramidal neurons. To simulate scenarios close to our human experimental data from HCP, we chose dMRI protocol using a gradient pulse length (δ) of 10.4 ms and separation (Δ) of 43.1 ms. For each soma we simulated two dMRI acquisitions, using 500 gradient strengths each, of $G_{\max}$ = 40 mT/m (b-value = 509 s/mm2), corresponding to clinical scanners, and of $G_{\max}$ = 97 mT/m (b-value = 3000 s/mm2), corresponding to the pre-clinical scanner used in the HCP protocol.

We found that at $G_{\max}$ = 40 mT/m the direction-averaged dMRI signal $E_{\max}$ at maximum gradient strength was $-\ln E_{\max} = 0.46 \pm 0.05$, indicating a signal decay of $36 \pm 3\%$ for large VEN-like neurons and $-\ln E_{\max} = 0.20 \pm 0.04$, i.e. $20 \pm 4\%$ decay for pyramidal-like neurons. This shows that at a clinically realistic SNR of 20, or even at 10, both types of neurons will induce a detectable change in the dMRI signal. Furthermore, when looking the RTOP simulation results showing a RTOP of 1.51 ± 0.05 times that of free water for large VENs and an RTOP of 1.74 ± 0.05 times that of free water for pyramidals, the difference between these two measurements is an order of magnitude larger than the measurement variance, showing that the RTOP measurements are characteristic of each population. We have also complemented these results with numerical simulations on 3-dimensional models of digitized neurons from histology adding to the evidence that RTOP is modulated by neuronal cell size in conditions akin to those of the HCP 1,200 diffusion dataset (Wassermann et al., 2018, Menon et al., submitted).

RTOP captures known microstructural features of the insular cortex in macaques

Because of the paucity of histological data from the human cortex, we then sought to determine whether in vivo measurements using RTOP can reveal known microstructural features of the macaque brain. Recently, Evrard et al. (2012) have provided a detailed account of the macaque insula architecture which can be summarized as follows: agranular areas contain VENs, the largest neurons in brain tissue, but no granule cells, some of the smallest neurons in brain tissue. Granular insula regions have a large number of granule cells but few, if any, VENs. Histological studies in the macaque

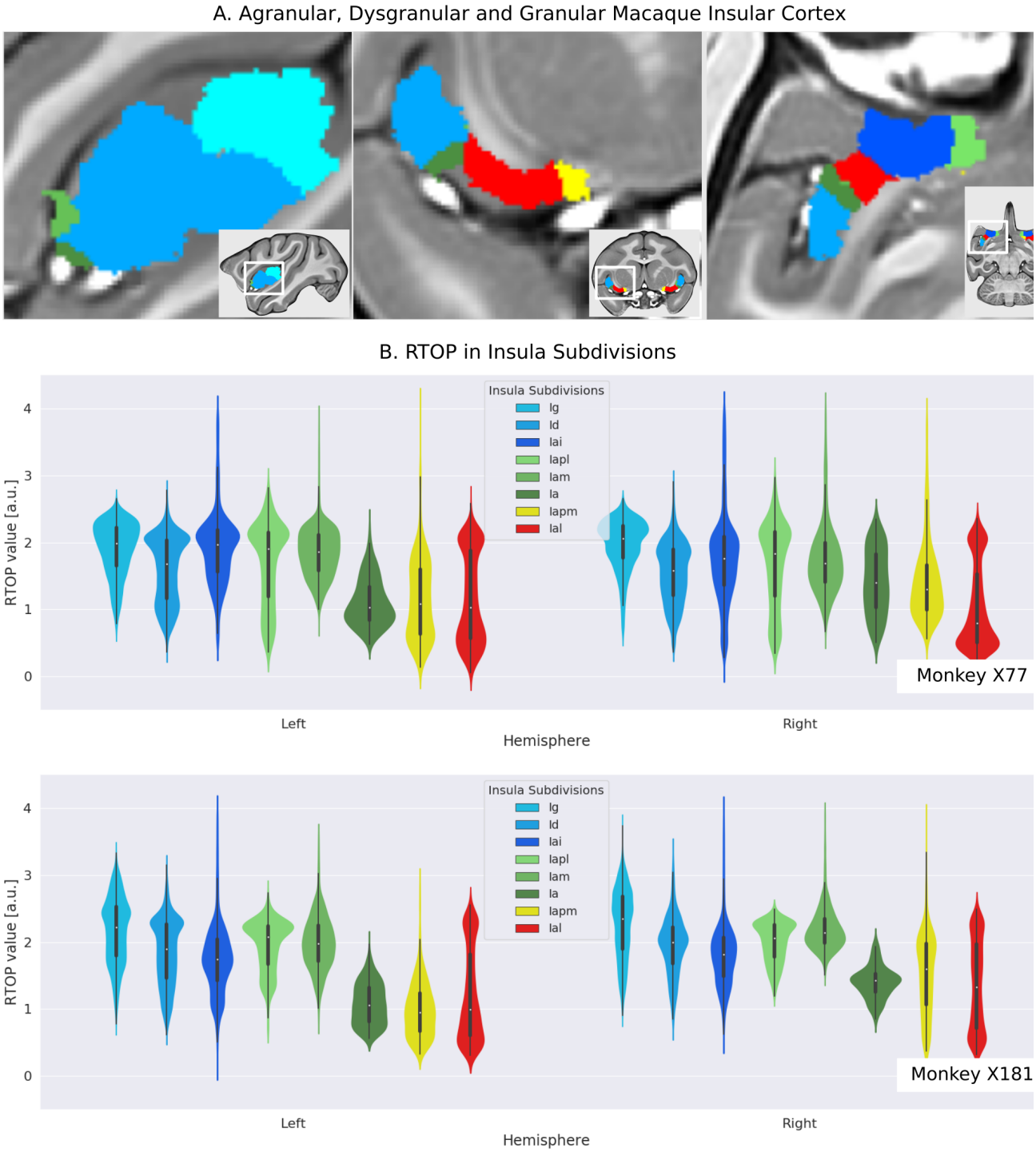

Figure 2.4: RTOP measurements agree with the cytoarchitectonic organization of the macaque insular cortex. RTOP normalised by average ventricular RTOP for cross-monkey comparison. (A) Cytoarchitectonic subdivisions of the insula in the macaque monkey. (B) Distribution of RTOP values inside the cytoarchitectonic insular subdivisions for the two monkeys (X77 and X181). RTOP inversely correlates with expected average neuron size: RTOP is significantly lower in the lateral agranular insula (Ial) region ($p<0.001$) and adjoining posteromedial agranular insula (Iapm) and agranular insula (Ia), compared to other insular subdivisions. Granular insula (Ig) region has significantly higher RTOP values than other insular subdivisions, except for the intermediate agranular insula (Iai) in monkey X77 ($p<0.001$).

brain have shown that VENs are on average 50% and 70% larger than local pyramidal neurons and are concentrated within lateral agranular insula (Ial). Consequently, we predicted that compared to granular insular cortex, RTOP values would be lower in agranular insula, reflecting the presence of large neurons such as the VENs. while granular insula regions have a large number of granule cells but few, if any, VENs. Histological studies in the macaque brain have shown that VENs are on average 50% and 70% larger than local pyramidal neurons and are concentrated within lateral agranular insula (Ial). Consequently, we predicted that compared to granular insular cortex, RTOP values would be lower in agranular insula, reflecting the presence of large neurons such as the VENs.

To test this hypothesis, we scanned two male rhesus macaques (Macaca mulatta, ages = 4 yrs, body weights = 5.6/6.8 kg). For all scan sessions, animals were first sedated with ketamine (10mg/kg IM) and maintained with isoflurane gas (2.5-3.0%) using an MR-compatible anesthesia workstation (Integra SP II, DRE Inc, Louisville KY). Data were collected to resemble the HCP dMRI protocol as close as possible. Specifically, we acquired the whole brain on a Siemens 3T MAGNETOM Prisma (80 mT/m @ 200 T/m/s gradient strength) using a surface coil (11cm Loop Coil; Siemens AG, Erlangen Germany) secured above the head. Nine T1-weighted volumes were collected for averaging to obtain a high-quality structural volume and diffusion images were acquired using a double spin-echo EPI readout pulse sequence. Four datasets of 271 gradient directions were collected using a monopolar gradient diffusion scheme with b values distributed optimally across 3 spherical shells. All macaque MRI data will be/is publicly available on the NKI PRIMatE Data Exchange database. The T1-weighted images were registered to the D99 atlas (Saleem et al., 2007) through the NMT—NIMH Macaque Template allowing the subdivision of the insula into granular, dysgranular, and agranular areas along with smaller subdivisions of each parcel. RTOP was computed using MAPL and normalised on each monkey using average ventricular RTOP following the Mitra et al. (1995) convention for unitless RTOP.

We found that RTOP values are indeed significantly lowest in the Ial in both right and left hemispheres, with more prominent effects in the right hemisphere where the right Ial had the lowest values compared to the rest of the right insular cortex. In the left insular cortex, the lowest values of RTOP were found in the Ial, agranular insula (Ia) and posterior-medial agranular insula (Iapm), the three agranular regions (Ia, Iapm, Ial) which adjoin each other (Figure 2.4). These findings are consistent with histological findings that the agranular cortex contains a greater population of VEN cells and a smaller population of small granule cells (Evrard et al., 2012). The presence of larger VENs increases the average cell size, thus decreasing restriction on the diffusion of water molecules, thereby resulting in lower RTOP values. Taken together, our analysis of the macaque brain provides new evidence that RTOP is sensitive to the presence of VENs and, critically, that it reflects the known cytoarchitectonic organization of the primate insular cortex ().

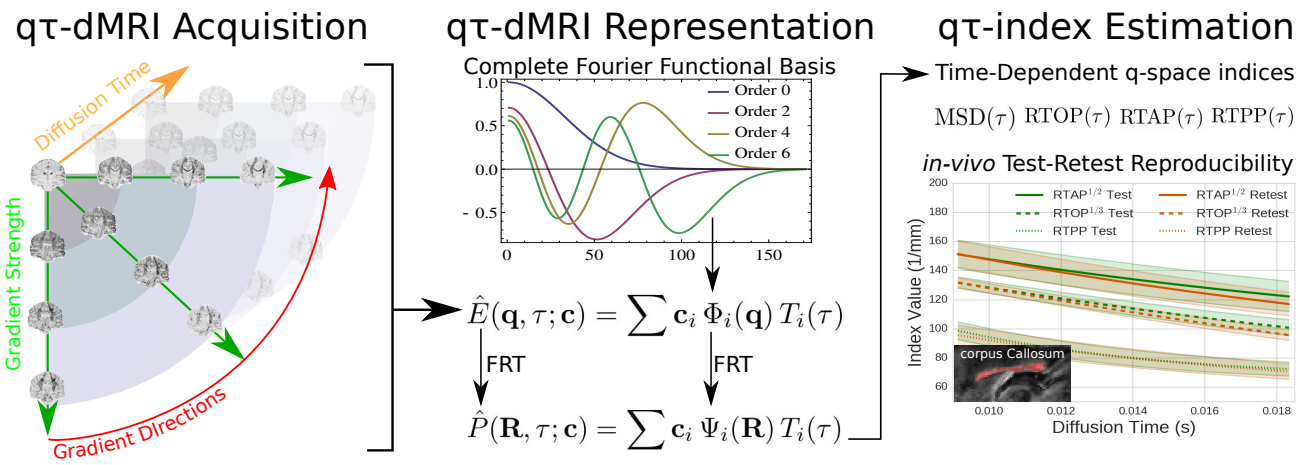

Figure 2.5: Visual Abstract of the second contribution. On the left we show a schematic representation of a four-dimensional qτ-acquisition, varying over gradient strength, directions and diffusion time. Our qτ-dMRI approach represents the qτ-diffusion signal using a functional *Fourier* basis. This allows for the analytic reconstruction of the *time dependent* Ensemble Average Propagator (EAP). From the EAP, we can then estimate *time-dependent* q-space indices, that we call qτ-indices. We do an *in-vivo* test-retest study in the corpus callosum of two mice, showing good reproducibility of estimated qτ-indices.

2.4 Second Contribution: Regularised dMRI signal representation in q-space and diffusion time

Probing brain tissue structure with time-dependent properties of the dMRI signal is gaining momentum in the dMRI community (see e.g. Burcaw et al., 2015; De Santis et al., 2016; Ning et al., 2017). Yet, effectively representing the four-dimensional dMRI signal, varying over three-dimensional q-space and diffusion time, is still challenging. To specifically represent the dMRI signal in this qτ-space, which has been coined by (Novikov et al., 2018a), we propose a qτ-functional basis approach, enriched with machine learning-typical regression models, that we appropriately refer to as "qτ-dMRI" (Fick et al., 2018b). As the main contribution, qτ-dMRI provides the framework to, without making biophysical assumptions, represent the qτ-space signal and estimate *time-dependent* q-space indices (qτ-indices) and reduce the requirements of acquitisiton protocols. Our approach synthetised in Figure 2.5

We generalise our approach presented in Section 2.3 to represent the measured qτ-signal attenuation $E(\mathbf{q},\tau)$ in terms of a continuous functional basis $\hat{E}_{\mathbf{c}}(\mathbf{q},\tau)$ where $\tau = \Delta - \delta/3$ is the diffusion time. Taking the same approach, we represent the attenuation in terms of coefficients $\mathbf{c} \in \mathbb{R}^{N_{\mathbf{c}}}$ with $N_{\mathbf{c}}$ the number of coefficients. As our functional basis has to cover one more dimention and the number of samples is limited, we add a sparsity goal to our previous formulation of effective representation, which needs to:

1. closely approximate the measured qτ-signal attenuation,
2. smoothly interpolate between and outside the measured $\{\mathbf{q},\tau\}$ points,
3. have a sparse representation in $\mathbf{c}$,

4. and be able to reconstruct the EAP from the fitted signal.

Requirements 1–3 are described in Equation (2.19) such that

$$\underset{\mathbf{c}}{\operatorname{argmin}} \iint_{\mathbb{R}^+\mathbb{R}^3} d\mathbf{q}d\tau \Bigg(\overbrace{\left[E(\mathbf{q},\tau) - \hat{E}_{\mathbf{c}}(\mathbf{q},\tau)\right]^2}^{\text{(1) Data Fidelity}} + \overbrace{\lambda \left[\nabla^2_{\mathbf{q}\tau} \hat{E}_{\mathbf{c}}(\mathbf{q},\tau)\right]^2}^{\text{(2) Smoothness}} \Bigg) + \overbrace{\alpha \|\mathbf{c}\|_1}^{\text{(3) Sparsity}} \tag{2.19}$$

$$\text{subject to } \hat{E}_{\mathbf{c}}(0,\tau) = \hat{E}_{\mathbf{c}}(\mathbf{q},0) = 1$$

where λ and α regularization weights. This formulation is inspired by the Elastic-Net regularization strategy (Zou et al., 2005), which has been adapted to neuroimaging (Grosenick et al., 2013), and is closely related to compressive sensing (Filipiak et al., 2018). As stated in Section 2.1, the boundary constraints are important to respect the Fourier relationship between the fitted signal attenuation and the EAP.

The Fourier relationship, shown above as the fourth condition, follows from our choice of a functional basis for $\mathbf{q}$-space that is also a *Fourier* basis. More formally, by choosing a Fourier basis, the following condition is met:

$$\hat{P}_{\mathbf{c}}(\Delta\mathbf{r};\tau) = \mathcal{F}^{-1}_{\mathbf{q}} \left\{ \hat{E}_{\mathbf{c}}(\mathbf{q},\tau) \right\}. \tag{2.20}$$

This means that once the coefficients $\mathbf{c}$ are fitted we immediately also obtain the EAP representation.

Functional Basis Signal Representation

We represent the qτ-signal using an orthogonal basis that allows for the implementation of all our previously stated requirements. As we assume the NPA, see Section 2.1, we represent the combined space $\hat{E}_{\mathbf{c}}(\mathbf{q},\tau)$ using the cross-product between the spatial basis $\Phi(\mathbf{q})$, presented in Section 2.3 and a temporal basis $T(\tau)$ as

$$\hat{E}_{\mathbf{c}}(\mathbf{q},\tau) = \sum_{i}^{N_{\mathbf{q}}} \sum_{k}^{N_\tau} \mathbf{c}_{ik}\, \Phi_i(\mathbf{q})\, T_k(\tau), \quad N_{\mathbf{q}} N_\tau = N_{\mathbf{c}} \tag{2.21}$$

where $N_{\mathbf{q}}$ and N_τ are the maximum expansion orders of each basis, and $\mathbf{c}_{ik}$ weights the contribution of the ik^{th} basis function to $\hat{E}_{\mathbf{c}}(\mathbf{q},\tau)$.

To implement the representation presented in Equation (2.21), we extend the regularised MAPL method introduced in Section 2.3 to encompass the representation of time-dependent decay. We use the MAPL basis as it neatly fulfills all four previously stated requirements; (1) being an orthogonal basis, it can accurately represent any signal over $\mathbf{q}$ using few coefficients; (2) it allows imposing smoothness using analytic Laplacian regularization (Fick et al., 2016b); and (3) MAP is a Fourier basis.

To derive the temporal basis, we study the limiting cases of the diffusion signal described in Section 2.1 for the behaviour of the diffusion signal over varying τ. Specifically: the attenuation is an exponential

decay for pure free, i.e. Gaussian; and diffusion and converges to a constant for diffusion in restricted geometries. An appropriate functional basis to represent the signal over τ should therefore be able to represent signal profiles between these two boundary cases with relatively few coefficients. We chose to use a product of the negative exponential and a Laguerre polynomial L_p, which together form an orthogonal basis over τ, as it can quickly capture the negative exponential nature of the temporal diffusion signal. The temporal basis we choose is then

$$T_p(\tau, u_t) = \exp(-u_t\tau/2)L_p(u_t\tau) \tag{2.22}$$

with basis order p and temporal scaling factor u_t. Specifically, the zeroth order is a pure exponential function and higher orders use the oscillating Laguerre polynomials to represent non-exponential aspects of the signal. Given enough coefficients, this time basis is able to represent any temporal diffusion signal without making assumptions on the underlying tissue structure. We study how many coefficients we actually need to represent the complete qτ-signal in (Fick et al., 2018a).

For the rest of this work we will linearize the ordering of our qτ-basis such that we use one basis index i with notation

$$\hat{E}_{\mathbf{c}}(\mathbf{q}, \tau) = \sum_{i}^{N_{\mathbf{c}}} \mathbf{c}_i \, \Xi_i(\mathbf{q}, \tau, 2\mathbf{D}\tau, u_t) = \sum_{i}^{N_{\mathbf{c}}} \mathbf{c}_i \, \Phi_{M(i)}(\mathbf{q}, 2\mathbf{D}\tau) \, T_{p(i)}(\tau, u_t). \tag{2.23}$$

where $M(i)$ and $p(i)$ are the mapping functions from i to the corresponding indices in Equation (2.21).

The qτ-EAP can be reconstructed using MAP's Fourier properties (Özarslan et al., 2013). The Fourier transform only concerns the $\mathbf{q}$-space, so the EAP is found simply by switching $\Phi(\mathbf{q}, 2\mathbf{D}\tau)$ in Equation (2.23) by its Fourier transform $\Psi(\Delta\mathbf{r}, 2\mathbf{D}\tau)$ in Equation (2.13).

Analytic Laplacian Regularization

We impose smoothness in the qτ-signal reconstruction by using the squared norm of the Laplacian of the reconstructed signal. In dMRI, this type of regularization has successfully been applied to several other techniques (see Fick et al., 2016a, and the references therein). We define the *Smoothness* term in Equation (2.19) as Laplacian functional $U(\mathbf{c})$ as

$$U(\mathbf{c}) = \iint \left[\nabla^2_{\mathbf{q}\tau} \hat{E}_{\mathbf{c}}(\mathbf{q}, \tau)\right]^2 d\mathbf{q} d\tau \tag{2.24}$$

where, due to our choice of basis, the Laplacian of the reconstructed signal can be estimated as $\nabla^2_{\mathbf{q}\tau}\hat{E}_{\mathbf{c}}(\mathbf{q}, \tau) = \sum_i c_i \nabla^2_{\mathbf{q}\tau}\Xi_i(\mathbf{q}, \tau, 2\mathbf{D}\tau, u_t)$. Equation (2.24) can be further rewritten in quadratic form as $U(\mathbf{c}) = \mathbf{c}^{\mathrm{T}}\mathbf{U}c$ with elements

$$\mathbf{U}_{ik} = \iint \nabla^2_{\mathbf{q}\tau}\Xi_i(\mathbf{q}, \tau, 2\mathbf{D}\tau, u_t) \cdot \nabla^2_{\mathbf{q}\tau}\Xi_k(\mathbf{q}, \tau, 2\mathbf{D}\tau, u_t) d\mathbf{q} \, d\tau \tag{2.25}$$

where the subscript ik indicates the ik^{th} position in the regularization matrix. We use the orthogonality of the basis functions (standard inner product on $[0, \infty]$) to compute the values of the regularization matrix to a closed form depending only on the basis orders and scale factors. For brevity here, we don't provide the formulation of $\mathbf{U}$ and refer the interest reader to Fick et al. (2018b).

Coefficient Estimation from qτ-Signal

To represent the qτ-signal $E(\mathbf{q}, \tau)$ in terms of a sparse coefficient vector $\mathbf{c}$ as $\mathbf{y} = \mathbf{Qc} + \epsilon$ where $\mathbf{y} \in \mathbb{R}^{N_\mathbf{y}}$ are the signal values with $N_\mathbf{y}$ the number of samples, $\mathbf{Q} \in \mathrm{R}^{N_\mathbf{y} \times N_\mathbf{c}}$ the observation matrix with elements $\mathbf{Q}_{ij} = \Xi_j(\mathbf{q}_i, \tau_i, 2\mathbf{D}\tau, u_t)$ and $\epsilon \in \mathbb{R}^{N_\mathbf{y}}$ the acquisition noise. We frame the numerical implementation of our approach in the same way as we did continuously in Equation (2.19):

$$\begin{aligned} &\text{argmin}_\mathbf{c} \overbrace{||\mathbf{y} - \mathbf{Qc}||_2^2}^{\text{(1) Data Fidelity}} + \overbrace{\lambda||\mathbf{c}^T\mathbf{Uc}||_2^2}^{\text{(2) Smoothness}} + \overbrace{\alpha||\mathbf{c}||_1}^{\text{(3) Sparsity}} \\ &\text{subject to } \mathbf{Q}^{\{\mathbf{q}=0,\tau>0\}}\mathbf{c} = \mathbf{1} \end{aligned} \tag{2.26}$$

where we described the *Smoothness* term in Section 2.4. The *Sparsity* term and constraints are imposed by framing our problem as a convex optimization using the open-source package CVXPY (Diamond et al., 2016). Note that we only impose the first $\hat{E}_\mathbf{c}(\mathbf{q} = 0, \tau)$ constraint as this is the only one that influences qτ-index estimation. The second $\hat{E}_\mathbf{c}(\mathbf{q}, \tau = 0)$ constraint is irrelevant as no diffusion takes place when $\tau = 0$. We find optimal values for regularization weights α and λ using cross-validation and implemented the surrounding code infrastructure inside the DiPy framework (Garyfallidis et al., 2014). In fact, the entire qτ-dMRI framework for regularized coefficient and qτ-index estimation is available at DiPy. We provide the detailed fitting procedure in Fick et al. (2018b).

2.4.1 Experiments and Discussion

In this section we detail two most important results supporting the applicability of our technique: first, it improves multi-shell signal reconstruction; second, it can be used as an effective preprocessing tool for multi-compartment models. For a more in-detail analysis of our contribution and comparison with the state of the art we refer the reader to our published work by Fick et al. (2015, 2018a) and Filipiak et al. (2018).

To assess the capabilities and reproducibility of our method *in-vivo* we performed test-retest diffusion spin echo acquisitions of two C57Bl6 wild-type mice. We show a sagittal cross-section of the fractional anisotropy (FA) map of the four data sets and the acquisition scheme in Figure 2.6. We drew a region of interest in the corpus callosum of each data set for our experiments.

Combined Laplacian and ℓ_1 regularization provides robustness to noise and subsampling

We compared the fitting error of our combined regularization strategy with that of other regularization approaches. In Figure 2.7, we showed that imposing both signal smoothness through Laplacian regularization and signal sparsity using the ℓ_1-norm produces the lowest fitting error for any number of samples. Using only Laplacian regularization as in Fick et al. (2015) produces higher fitting errors when fewer than 200 samples are fitted, but performs similarly otherwise. Our combined regularization scheme can be seen as a modification to Elastic-Net regularization (Zou et al., 2005) along the same lines as GraphNet (Grosenick et al., 2013). Similar to their approach, we modify ℓ_2-norm penalty term in the Elastic-Net to use the norm of the Laplacian of the measured signal. Our approach differs from

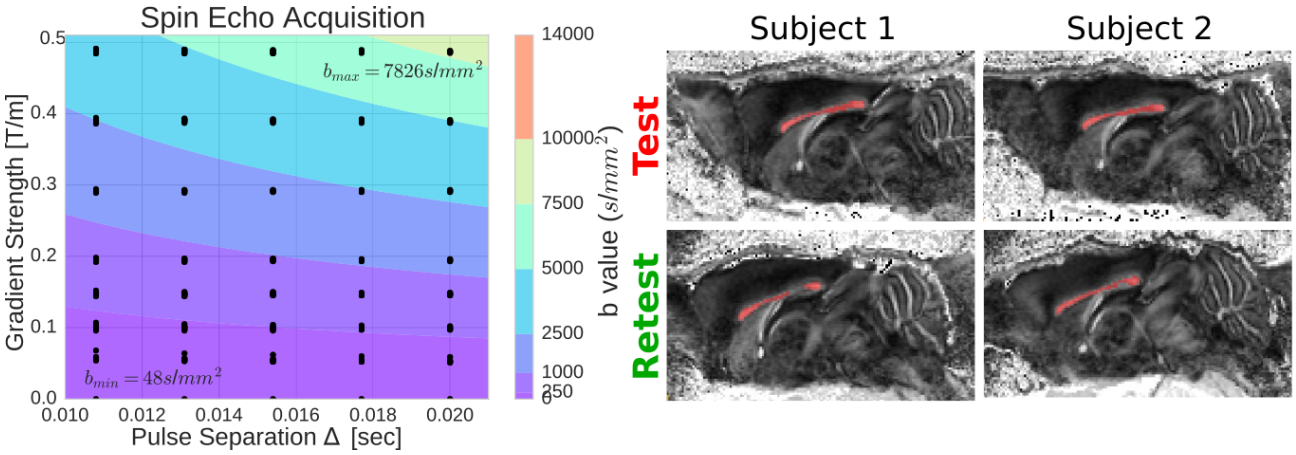

Figure 2.6: left: the 35 shell qτ-diffusion acquisition using a spin echo sequence. Every group of point represents a shell with uniformly spread DWIs on the sphere and one b0 image. The contours represent b-value isolines, given as $b = G^2\delta^2\gamma^2(\Delta - \delta/3)$, whose values are given in the colorbar. The slight spread is due to field inhomogeneities in the *in-vivo* acquisition and are not present in the synthetic simulations. Right: FA illustrations of the test-retest mice with in red the region of interest (ROI) voxels in the corpus callosum.

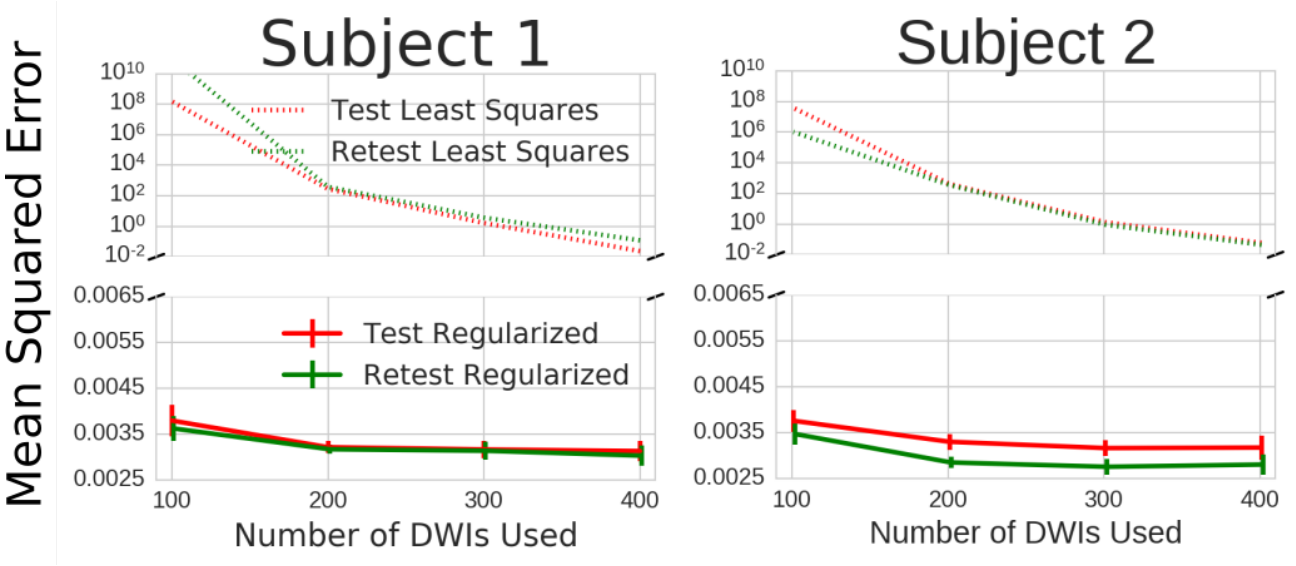

Figure 2.7: Regularized fitting error of our model while randomly subsampling the data from 400 to 100 fitted DWIs. We broke the y-axis into two parts. The top part uses log-scaling to show the much higher fitting error of unregularized qτ-dMRI. The bottom part uses regular scaling and shows our much lower regularized fitting error. For the regularized result, we see that the fitting error is robust to subsampling for all data sets.

theirs in that the coefficients in qτ-dMRI represent the Eigenfunctions of the signal and EAP, while those of GraphNet are discrete measurements of graph connectivity. This allows for the closed-form estimation of the Laplacian in the qτ-space, as we illustrate in Fick et al. (2018b).

Estimation of qτ-indices is reproducible *in-vivo*

We tested the reproducibility of qτ-index estimation on two test-retest diffusion Spin Echo acquisitions of C57B16 wild-type mice. We selected an ROI in the corpus callosum (Figure 2.6) to limit our

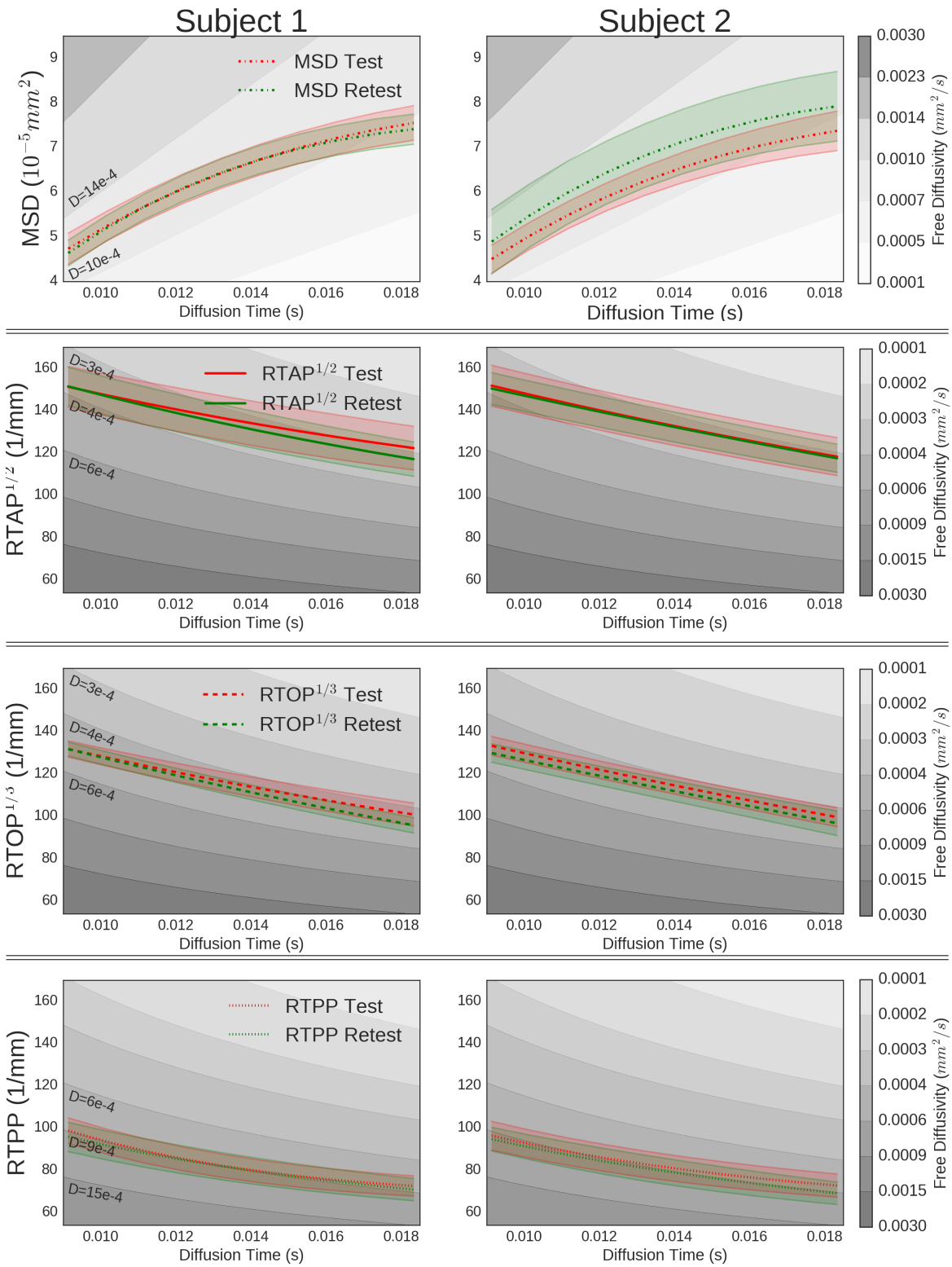

Figure 2.8: Mean and 0.75×Standard deviation of the MSD (top) and RTOP, RTAP and RTPP (bottom) in the corpus callosum for the test and retest data (red and green) of both subjects. We used a 0.75 multiplier to better separate index groups. For comparison, the gray tones show MSD isolines for different free diffusion coefficients. In subject 1 the test-retest indices overlap closely for every metric, indicating excellent reproducibility. Subject 2 shows similar overlap for q-space indices, but for MSD.

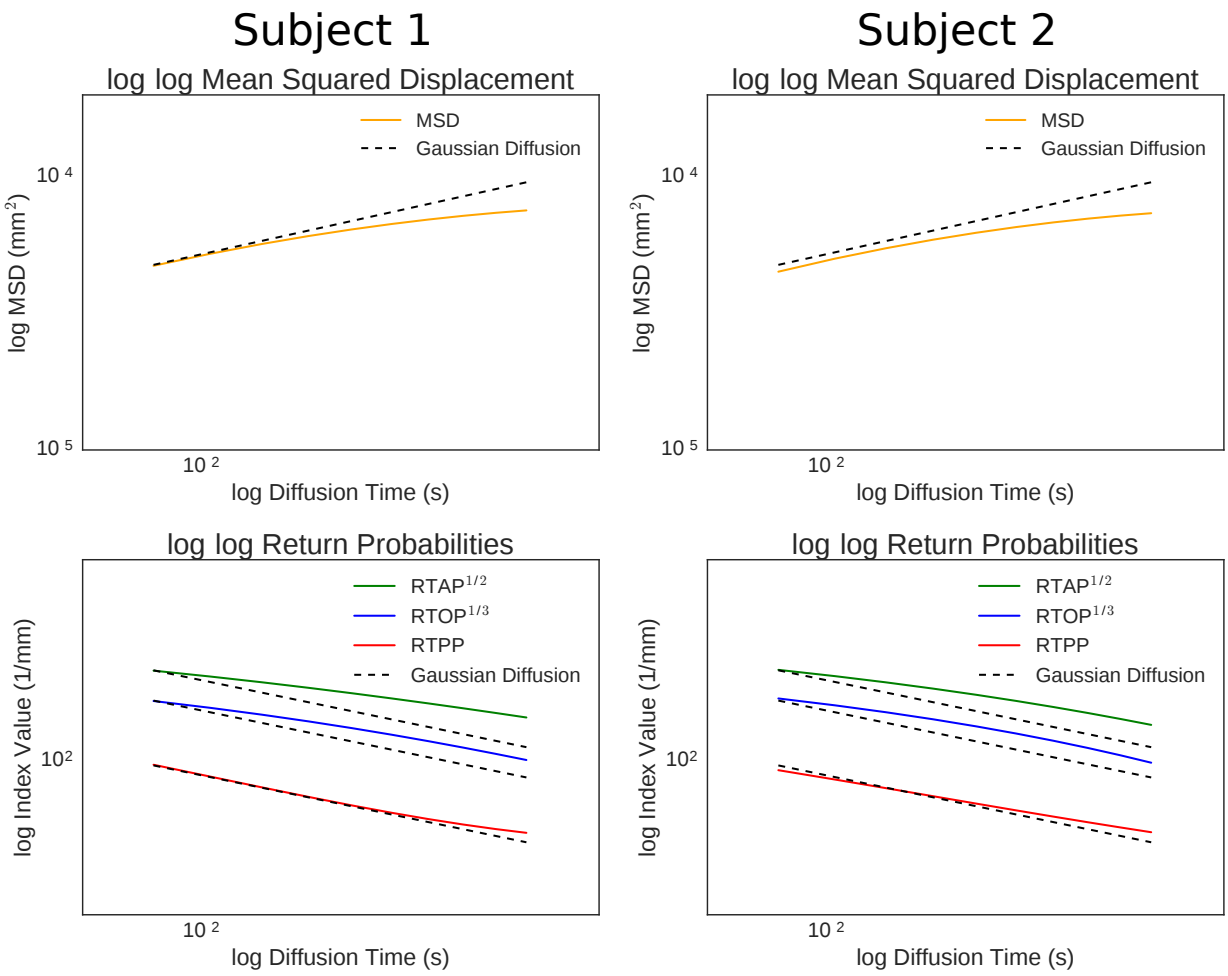

Figure 2.9: Log-log plots of mean MSD (top) and mean return probabilities (bottom) of both Test Subjects. The dashed lines are the index values for free Gaussian diffusion with diffusivities chosen such that the estimated and Gaussian index values of Subject 1 start at the same place. Power-laws of the form $y = ax^k$ show as straight lines in log-log plots. In Subject 1, notice that the estimated MSD starts close to Gaussian and then slowly diverges at longer τ. Similarly, the RTPP, describing parallel diffusion, is almost completely Gaussian over diffusion time. $\text{RTAP}^{1/2}$ has a non-Gaussian slope from the start, and RTOP has non-Gaussianity between $\text{RTAP}^{1/2}$ and RTPP. The trends between subjects are very similar, but differ slightly in MSD and RTPP.

study to anisotropic white matter with minimal axonal dispersion effects (see e.g. Ronen et al., 2014; Palombo et al., 2018). We acquired anisotropic voxels to improve the SNR at high gradient strengths and diffusion times. Fitting qτ-dMRI to the *in-vivo* data produced results that are in agreement with the synthetic experiments; both the fitting error and qτ-index trends are similar (Figures 2.7 and 2.8). Of particular interest is Figure 2.8, where we plot the test-retest values of MSD, RTAP, RTOP and RTPP over diffusion time. The isolines in the background, representing the q-space index value for free diffusion with varying diffusivity, shows that qτ-dMRI q-space trends are actually picking up on diffusion restriction over diffusion time. For different indices we find different levels of restriction over time. This is particularly clear in the log-log plots in Figure 2.9. In log-log plots, power-laws of the form $\text{Index}(\tau) \propto \tau^k$ show as straight lines with slope k. Gaussian diffusion will therefore always have

the same slope regardless of the diffusivity. We can clearly see that the slope of RTPP the steepest and is nearly parallel to that of Gaussian diffusion, while the slope of RTAP is the shallowest, showing the most restriction.

Our qτ-dMRI representation is an effective tool for acquisition sequence design

The main goal of our final study (Filipiak et al., 2018) is to develop a method to find samplings scheme that maximizes the accuracy of signal representation and satisfies given time constraints. Similar studies were performed for other dMRI models and acquisition protocols and we review them in the work by Filipiak et al. (2018). However, none of these models, to the best of our knowledge, addresses full qτ-space optimization.

Our goal is to optimize for the accuracy of $q\tau$-dMRI signal reconstruction. Additionally, we want our approach to be usable on real-world applications, considering that different acquisition protocols are recommended for different WM microstructure models (Sepehrband et al., 2017). For this, we discretize the spatio-temporal search space by performing a dense pre-acquisition of dMRI signal with uniform coverage of the unit sphere (Caruyer et al., 2013). Despite the discretization, the problem is computationally difficult. It requires selecting an optimal subset of DWIs according to a given performance measure, which is an NP-hard problem (Filipiak et al., 2018).

Taking into account that the time complexity of our problem grows exponentially with the domain size, such that global optima cannot be found deterministically within few hours or even few days, we apply a stochastic search engine instead. We use standard genetic algorithm optimization (SGA)(Peña-Reyes et al., 2000; Sabat et al., 2003) for this purpose, which allows us to find approximate solutions in an acceptable time. Specifically, we select a subset of measures from the full set such that

$$\arg \min_{s \subset S,\, \#s \leq n_{\max}} \iint_{\mathbb{R}^+\mathbb{R}^3} d\tau d\mathbf{q} \|\hat{E}_{\mathbf{c}}(\mathbf{q}, \tau; s) - \hat{E}_{\mathbf{c}}(\mathbf{q}, \tau; S)\|_2^2 \tag{2.27}$$

with S the original set of qτ-samples, $n_{\max}$ the number of desired samples for the acquisition scheme, and $\hat{E}_{\mathbf{c}}(\mathbf{q}, \tau; s)$ is our qτ-MRI model, from Equation (2.19), fit over the qτ-sample s.

We study on the same mice dataset two granularity levels of optimization with respect to the domain size. Selecting specific qτ-shells, i.e. sets of constant $\|\mathbf{q}\tau\|_2^2$, allows us to present the effectiveness of the proposed approach by comparing our results with the global optimum found with lengthy exhaustive search. Selecting by individual qτ-sample provides us with crucial information about the structure of the optimized acquisition schemes.

Our experiments show that the reconstruction accuracy grows monotonically with an increase of dMRI acquisition density. However, the contributions of particular DWIs to the measured signal attenuation are not equal. This indicates the need for identifying a variable-density for acquiring the dMRI signal. Our method, described by Filipiak et al. (2018), seeks a fixed-sized set of samples that provide the most accurate signal reconstruction with respect to the reference data obtained with the dense acquisition scheme. In other words, our approach allows reaching high accuracy within a controllable time budget.

region of interest	time budget n_{max}	NRMSE ± STD $[\times 10^{-3}]$ optimization by shells ours	optimization by shells random	optimization by shells even	optimization by samples ours	optimization by samples random	optimization by samples even
CC genu	100	**110.2 ± 0.45**	131.6 ± 14.98	120.1	**106.9 ± 0.33**	118.9 ± 1.95	120.8
	200	**103.7 ± 0.17**	112.7 ± 4.18	112.1	**102.8 ± 0.14**	109.8 ± 1.10	114.1
	300	**101.7 ± 0.14**	108.3 ± 3.11	106.9	**101.5 ± 0.09**	106.4 ± 0.78	106.5
	400	**100.6 ± 0.05**	104.9 ± 1.75	105.4	**100.8 ± 0.13**	104.1 ± 0.52	104.1
CC body	100	**127.6 ± 0.85**	172.2 ± 44.30	144.2	**122.9 ± 0.54**	142.1 ± 3.28	155.3
	200	**116.1 ± 0.45**	136.2 ± 9.83	132.7	**116.6 ± 0.19**	128.4 ± 1.76	149.7
	300	**111.9 ± 0.36**	124.8 ± 6.41	122.0	**113.4 ± 0.20**	121.4 ± 1.73	124.1
	400	**109.9 ± 0.22**	118.9 ± 3.13	119.1	**111.5 ± 0.10**	116.8 ± 1.16	119.9
CC splenium	100	**107.0 ± 1.09**	133.3 ± 19.75	123.1	**104.4 ± 0.37**	117.9 ± 2.80	131.1
	200	**101.4 ± 0.41**	111.2 ± 4.82	109.6	**100.9 ± 0.11**	108.4 ± 1.32	141.0
	300	**99.9 ± 0.42**	105.7 ± 2.23	106.8	**99.6 ± 0.09**	104.2 ± 0.75	104.4
	400	**99.0 ± 0.42**	103.2 ± 1.46	103.7	**98.6 ± 0.12**	101.9 ± 0.53	103.8

Table 2.9: Our approach significantly outperforms the other two subsampling schemes (with p-value $< 10^{-5}$) in both granularity levels (*by shells* and *by samples*), reaching lower means and standard deviations. The tables present the residuals of the dMRI signal reconstruction for the three regions of C57Bl6 wild-type mouse corpus callosum (CC) and the time budgets $n_{max} \in \{100, 200, 300, 400\}$. Our results are expressed as normalized root mean squared errors (NRMSEs) of signal reconstruction with STDs aggregated over 30 runs.

As we can see in Table 2.9 the accuracy of dMRI signal reconstruction obtained with our technique is significantly better than *random* or *even* subsampling of the densely acquired signal. This shows that our signal representation method coupled with the optimization approach presented we presented in the work by Filipiak et al. (2018) enables a time reduction in dMRI acquisitions which sample over the qτ-space.

CHAPTER 3

Brain Macrostructure with Diffusion MRI

Complementary to the theoretical and practical characteristics of the dMRI signal to probe tissue microstructure reviewed in Chapter 2, the integration of the signal over the spatial domain provides a method to probe the brain's macrostructure. Specifically, The consistency of the dMRI signal's principal diffusion direction with that of white matter tract bundles enabled the reconstruction of these tracts and the quantification of the likelihood that two brain sections are connected through a white matter pathway (e.g. Conturo et al., 1999; Mori et al., 1999; Basser et al., 2000; Behrens et al., 2003a).

The macrostructural analyses of dMRI spanned two different, yet related, subfields. The first, namely tractography, deals with the *in vivo* dissection, characterization, and identification of white matter tracts (see e.g. Makris et al., 1999; Catani et al., 2008; Yeatman et al., 2014; Wassermann et al., 2016). Despite the recent intense criticism due to the strong biases present in, increasingly complex, reconstruction algorithms (Maier-Hein et al., 2017), this field has managed to continue in the spirit of Dejerine et al. (1895) atlasing the connections of the human brain's white matter and their relationship with cognition and neuropathology (see e.g. Catani et al., 2007; Thiebaut de Schotten et al., 2011a; Hong et al., 2018).

The second sub-field, connectivity, aims at relating the probability that two regions of the brain are connected by a white matter tract with brain function and cognition. Albeit the precise definition of dMRI-obtained connectivity, namely extrinsic connectivity (EC), remains elusive, especially in terms of its physiological interpretation, several studies have used tractography based techniques to characterise cortical areas (see e.g. Behrens et al., 2003a; Anwander et al., 2007; Gallardo et al., 2017; Ghaziri et al., 2017) and relate such connectivity with brain function (see e.g. Honey et al., 2009;

Saygin et al., 2016). Further investigation is needed to relate EC with the ultimate hypothesis that it allows us to quantify communication efficiency, or at least signal propagation speed, along axonal tissue (Caminiti et al., 2013; Keller et al., 2014).

Two methodological contributions to the dMRI-based study of the brain macrostructure are presented in this chapter. The first one aims at using the currently available large datasets to parcellate the brain in the brain based on EC, the main contribution being the handling of across and within-subject variability. The second one, aiming at breaching the gap between classical and current data-based neuroanatomy: a domain specific language (DSL) to represent white matter neuroanatomy and facilitate automatic white matter tract identification as delineation protocol reproducibility (Wassermann et al., 2016).

3.1 First contribution: group-wise Parcellation of the Cortex: the Need for Random Effects

The human brain is arranged in areas based on criteria such as cytoarchitecture, functional specialization, or axonal connectivity (Brodmann, 1909; Thirion et al., 2014; Thiebaut de Schotten et al., 2016). Parceling the cortex into such areas and characterizing their interaction is key to understanding how the brain works. Nowadays it is accepted that axonal connectivity plays a fundamental role in the interaction between brain regions (see e.g. Schmahmann et al., 2006). Moreover, current theories hold that long-range physical connections trough axonal bundles, namely *extrinsic connectivity* (EC), are strongly related to brain function, for example, this has been shown in macaques (Passingham et al., 2002). Therefore, understanding how the cortex is arranged based on its extrinsic connectivity can provide key information in unraveling the internal organization of the brain.

In this section, we present a parsimonious model for the cortical connectivity alongside an efficient parceling technique based on it. We summarize both contributions in Fig. 3.1. Our model assumes that the cortex is divided in patches of homogeneous extrinsic connectivity. That is, nearby neurons in the cortex share approximately the same long-range physical connections, we call this the *local coherence criterion*. Our assumption is based on histological results in the macaque brain (Schmahmann et al., 2006). Inspired by statistical models for clustered data (Pendergast et al., 1996), our model accounts for the variability in the axonal connections of neurons within a patch and for variability in patch boundaries across subjects. Our parceling technique allows us to create single subject and groupwise parcellations of the whole cortex in agreement with extant parcellations.

The model we introduce assumes that the cortex is divided in clusters of homogeneous EC. That is, nearby neurons in the cortex share approximately the same long-ranged axonal connections, we call this the *local coherence criterion*. Our assumption is based on histological results in the macaque brain (Schmahmann et al., 2006). As in clustered data models in statistics (Pendergast et al., 1996), we

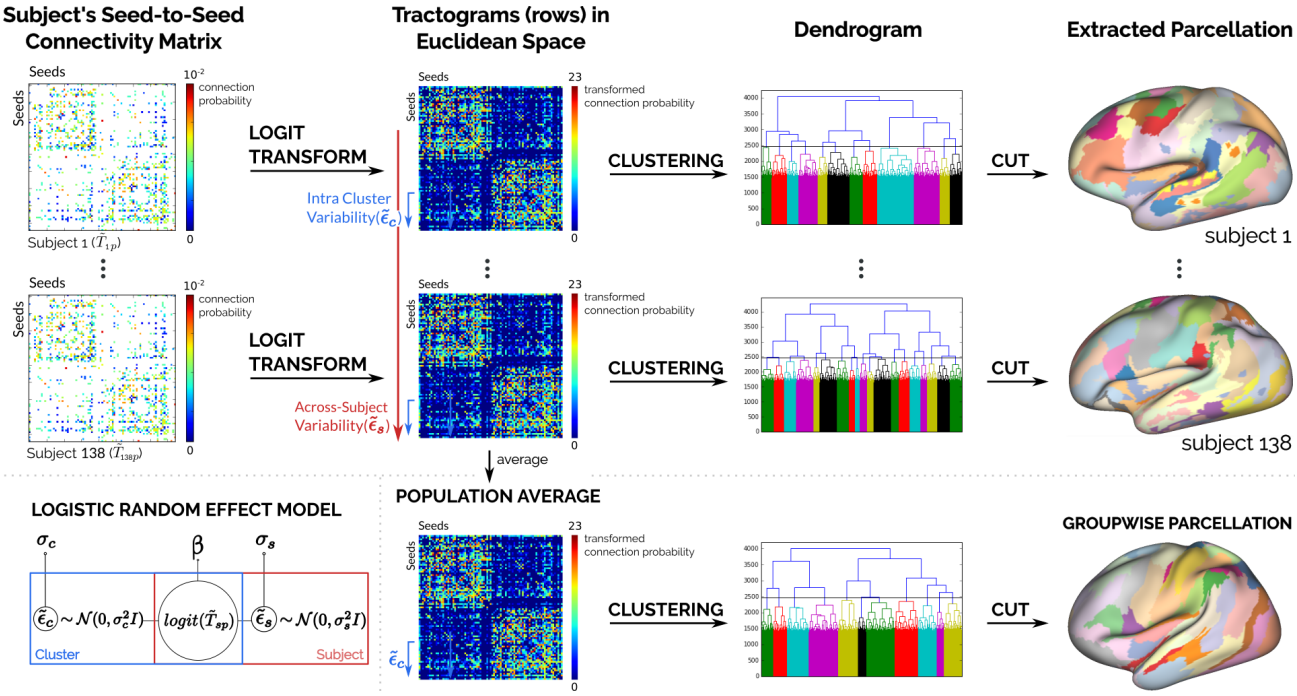

Figure 3.1: Lower left corner: graphical model of the linear relationship between the tractogram of a subject s for a seed p ($\tilde{T}_{sp}$); and the intra-cluster ($\tilde{\epsilon}_c$) and across-subject ($\tilde{\epsilon}_s$) variability of the seed's patch. We transform the tractograms into a Euclidean space while explicitly accounting for the variability. This allows us to use well known clustering techniques and compress different levels of granularities for a same parcellation in a dendrogram.

allow intra-cluster and across-subject variability in the connectivity. We formalize this concept as:

$$K = \bigcup_{i=1}^{k} K_i, \forall_{1 \leq i,j \leq k}, i \neq j \rightarrow K_i \cap K_j = \emptyset \wedge \text{conn}(K_i) \neq \text{conn}(K_j) \tag{3.1}$$

where the set of points, or small regions, on the cortex K is the disjoint union of each cluster K_i and conn$(\cdot)$ is the EC fingerprint of a cluster. We will make the notion of variability explicit in Equation (3.3). In this work, the connectivity fingerprint of a seed-point in the brain is a binary vector denoting to which other seed-points it is connected through axonal bundles. That is, the axonal connections of a point $p \in K_i$ in the brain are represented by its connectivity fingerprint conn(p) = conn(K_i).

Currently, the most common tool for estimating the EC fingerprint of a point in vivo is probabilistic tractography (see e.g. Jbabdi et al., 2013; Jeurissen et al., 2017). Given a seed-point in the brain, probabilistic tractography creates a *tractogram*: an image where each voxel is valued with its probability of being connected to the seed through axonal bundles. One way of calculating these probabilities is with a Monte Carlo procedure, simulating the random walk of water particles through the white matter (Behrens et al., 2003b). Each one of these paths is known as a streamline. If we model these streamlines as Bernoulli trials, where we get a value for the connection from our seed with other points: 1 if they connected by the streamline, 0 if not (Behrens et al., 2003b). Then, we can model the

tractogram of the subject s in the seed-point p as:

$$T_{sp} = [\mathbb{P}(\tilde{C}_{spi} = 1)]_{1\leq i\leq n} = [\theta_{spi}]_{1\leq i\leq n},\ \tilde{C}_{spi} \sim \text{Bernoulli}(\theta_{spi}), \tag{3.2}$$

where $\tilde{C}_{spi}$ is a Bernoulli random variable[1] representing "the point p of the subject s is connected to the voxel i". Each Bernoulli's parameter (θ_{spi}) represents the probability of being connected, and is estimated as the proportion of success in the Bernoulli trials of each seed.

To formulate the tractogram in accordance to our hypothesis of cortical connectivity, we model it as a vector of random variables. In our model, each element in a tractogram comes from a random variable depending on the point's cluster along with its intra-cluster and across-subject variability:

$$p \in K_c \rightarrow \tilde{T}_{sp} = [\mathbb{P}(\tilde{C}_{spi} = 1 | \,\text{conn}(K_c),\ \tilde{\epsilon}_{ci},\ \tilde{\epsilon}_{si})]_{1\leq i\leq n}. \tag{3.3}$$

In this case, the point p belongs to the cluster c; $\tilde{\epsilon}_{ci}$ represents the intra-cluster variability; and $\tilde{\epsilon}_{si}$ represents the across-subject variability for the connectivity to voxel i in the cluster c.

Since each $\tilde{C}_{spi}$ follows a Bernoulli distribution, see Equation (3.2), it is difficult to find an explicit formulation for $\mathbb{P}(\tilde{C}_{spi} = 1 | \,\text{conn}(K_c),\ \tilde{\epsilon}_{ci},\ \tilde{\epsilon}_{si})$ accounting for both variabily sources. For this, we use the generalized linear model (GLM) theory. In this theory, the data is assumed to follow a linear form after being transformed with an appropriate link function (McCullagh et al., 1989). Using the following notation abuse:

$$\text{logit}(\tilde{T}_{sp}) \triangleq [\text{logit}(\mathbb{P}(\tilde{C}_{spi} = 1 | \,\text{conn}(K_c),\ \tilde{\epsilon}_{ci},\ \tilde{\epsilon}_{si})]_{1\leq i\leq n}, \tag{3.4}$$

we derive from GLM theory a logistic random-effects model (Pendergast et al., 1996) for each point p:

$$\text{logit}(\tilde{T}_{sp}) = \beta_c + \tilde{\epsilon}_c + \tilde{\epsilon}_s \in \mathbb{R}^n, \quad \tilde{\epsilon}_c \sim \mathcal{N}(\mathbf{0}, \sigma_c^2 Id),\ \tilde{\epsilon}_s \sim \mathcal{N}(\mathbf{0}, \sigma_s^2 Id), \tag{3.5}$$

where ϵ_c and ϵ_s represent the intra-cluster and across-subject variability respectively. According to GLM theory $\beta_c \in \mathbb{R}^n$ is the EC fingerprint of cluster K_c transformed:

$$\text{logit}^{-1}(\beta_c) = \mathbb{E}(\tilde{T}_{sp}) = \text{conn}(K_c)\ . \tag{3.6}$$

The choice of logit as link function is based on the work of Pohl et al. (2007). In their work they show that logit function's codomain is an Euclidean space, which allows us to transform and manipulate the tractograms in a space with comfortable algebraic properties.

3.1.1 Single Subject and Groupwise parceling Methodologies

In the previous section, we hypothesized that the cortex is divided in clusters with homogeneous EC, alongside intra-cluster and across-subject variability. In using the previous hypothesis, it is important

[1] For the sake of clarity we denote all random variables with a tilde, e.g. $\tilde{C}$.

to underline that we don't have a priori knowledge of the cluster's location or their variability. But, thanks to the proposed logistic random effects model, we formulated the problem of finding these clusters as a well-known clustering problem. This is because, after transforming the tractograms with the logit function as in Equation (3.4) they will be in a Euclidean space (Pohl et al., 2007). Even more, Equation (3.5) states that the transformed tractograms come from a mixture of Gaussian distributions, e.g. it is a Gaussian mixture model.

To solve the Gaussian mixture model and find the clusters, we use a modified agglomerative hierarchical clustering (AHC) algorithm. This was inspired by the method of Moreno-Dominguez et al. (2014). To enforce the local coherence criterion we also modify the algorithm to accept one parameter: the minimum size of the resulting clusters. Clusters smaller than this size are merged with neighbors, i.e. physically close clusters in the cortex. As we are working in a Euclidean space, we use Ward's hierarchical clustering method (Ward Jr., 1963). This method creates clusters with minimum within-cluster variance. The method's result is a dendrogram: a structure that comprises different levels of granularity for the same parcellation. This allows us to explore different parcellation granularities by choosing cutting criteria, without the need of recomputing each time.

The main advantage of the model we proposed in this work is that it allows us to create a groupwise parcellation using linear operations. Assuming direct seed correspondence across subjects, as in the HCP data set, our model lets us remove the subject variability of each seed's tractogram by calculating the expected value across subjects:

$$\mathbb{E}_s(g(\tilde{T}_{sp})) = \mathbb{E}_s(\beta_c + \tilde{\epsilon}_c + \tilde{\epsilon}_s), = \beta_c + \tilde{\epsilon}_c + \mathbb{E}_s(\tilde{\epsilon}_s) = \beta_c + \tilde{\epsilon}_c. \tag{3.7}$$

where the last equality is due to $\mathbb{E}_s(\tilde{\epsilon}_s) = 0$ per Equation (3.5). Since in our model the variabilities are normally distributed, see Equation (3.5), we can estimate the expected value across subjects by averaging a seed's tractograms across subjects. This allows us to create population-representative tractograms for each seed free of across-subject variability, which then can be clustered to create a groupwise parcellation.

3.1.2 Discussion

Taking advantage of our proposed model, in Section 3.1.1 we presented an efficient technique to parcellate the cortex based on its extrinsic connectivity. Our technique uses only dMRI information, without the need of relying on initial parcellations (Clarkson et al., 2010). Also, our technique allows parcellation of the whole cortex (Gallardo et al., 2017, section 3.2 and 3.3), overcoming the problem of working with only part of it (Roca et al., 2009; Thiebaut de Schotten et al., 2014; Lefranc et al., 2016; Thiebaut de Schotten et al., 2016). Additionally, our technique allows creation of both single subject and groupwise parcellations. Our groupwise parcellation technique relies on anatomical seed-correspondence across subjects. In our experiments, this is achieved as each HCP subject possess a co-registered dense mesh representing they cortical surface (Glasser et al., 2013). Given

the anatomical differences across-subjects, this purely anatomical matching of seeds is probably sub-optimal. However, it allows us to compute single and groupwise parcellations independently. By doing this, we avoid the need to impose constraints between our single and group parcellations (Clarkson et al., 2010; Roca et al., 2010; Parisot et al., 2015).

Inspired by Moreno-Dominguez et al. (2014), our technique uses Hierarchical Clustering to comprise multiple granularities of the same parcellation in a dendrogram. Our technique is based on a Logistic Random Effect model (Equation (3.5)) allowing us to transform the tractograms into a Euclidean space (Section 3.1.1) and compare them using the Euclidean distance. In doing this, it is important to remark that we are making a trade off. Since we are comparing high-dimensional vectors with the Euclidean distance, we are probably affected by the dimensionality curse (Beyer et al., 1999). However, working in an Euclidean space possess many advantages. The first advantage is that we can use Ward's Hierarchical method to create clusters with minimum intra-cluster variance. We can use this algorithm since its only hypothesis is that the features to cluster are in a Euclidean space. Also, since we work with the Euclidean distance, we can apply the Lance and Williams (Lance et al., 1966) formula during clustering. This formula gives us the dissimilarity between the new centroid created at each step and the rest of the existing tractograms in constant time. This allows us to lower the time complexity of our algorithm with respect to Moreno-Dominguez et al. (2014). Furthermore, advantage is that we can retrieve a parcellation from the dendrogram using a simple technique: horizontal cut (Murtagh, 1983).

Parcellations obtained by our method have shown to be consistent across groups in a reproducibility study as well as to be in agreement with extant parcellations in the literature (Gallardo et al., 2017). Further more, two main results distinguish our method from those in literature: close relationship of our parcels and brain function.

Our Results Show a Close Relationship Between Structural Connectivity and Brain Function. We assessed the functional specialization of some of our parcels by showing how they overlap with responses to functional and cognitive tasks measured with fMRI on the HCP dataset. In particular, for all the studied tasks, the parcels contained a higher proportion of positive values than negative ones as expressed by the positive mean values reported in tables 2 and 3. For some parcels there were not even negative values. Moreover, several of the histograms on Figures 3.2 and 3.3 show a high frequency of z-score values greater than 5, which indicate a significant co-occurrence with functional activation. Therefore, our results show, for some tasks, the strong relationship between extrinsic connectivity and functional specialization in the human brain cortex.

Our Parcels Are Not Similar to Those Obtained by Glasser et al. (2016) But Possess Better Functional Specialization for Motor Tasks.
Our parcels were not related to those of Glasser et al. (2016). This is shown by the obtained adjusted Rand index score between them (0.28). It's important to remark that our parcels are purely based on

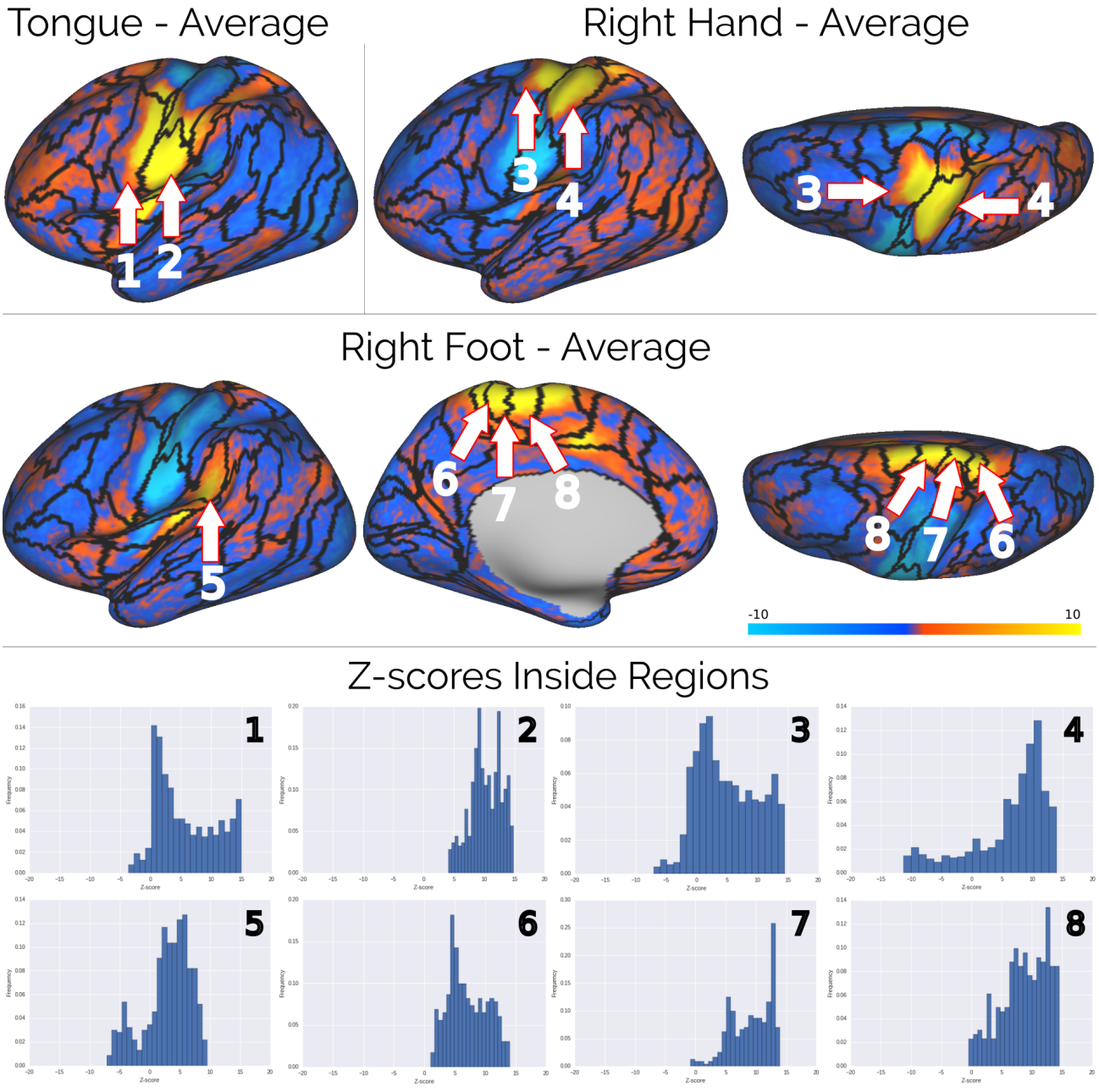

Figure 3.2: Our groupwise parcellation with 55 parcels projected over z-scores representing responses to motor tasks. Each histogram shows the distribution of z-score inside our parcels. The null or small fraction of negative values shows the functional specialization of our parcels

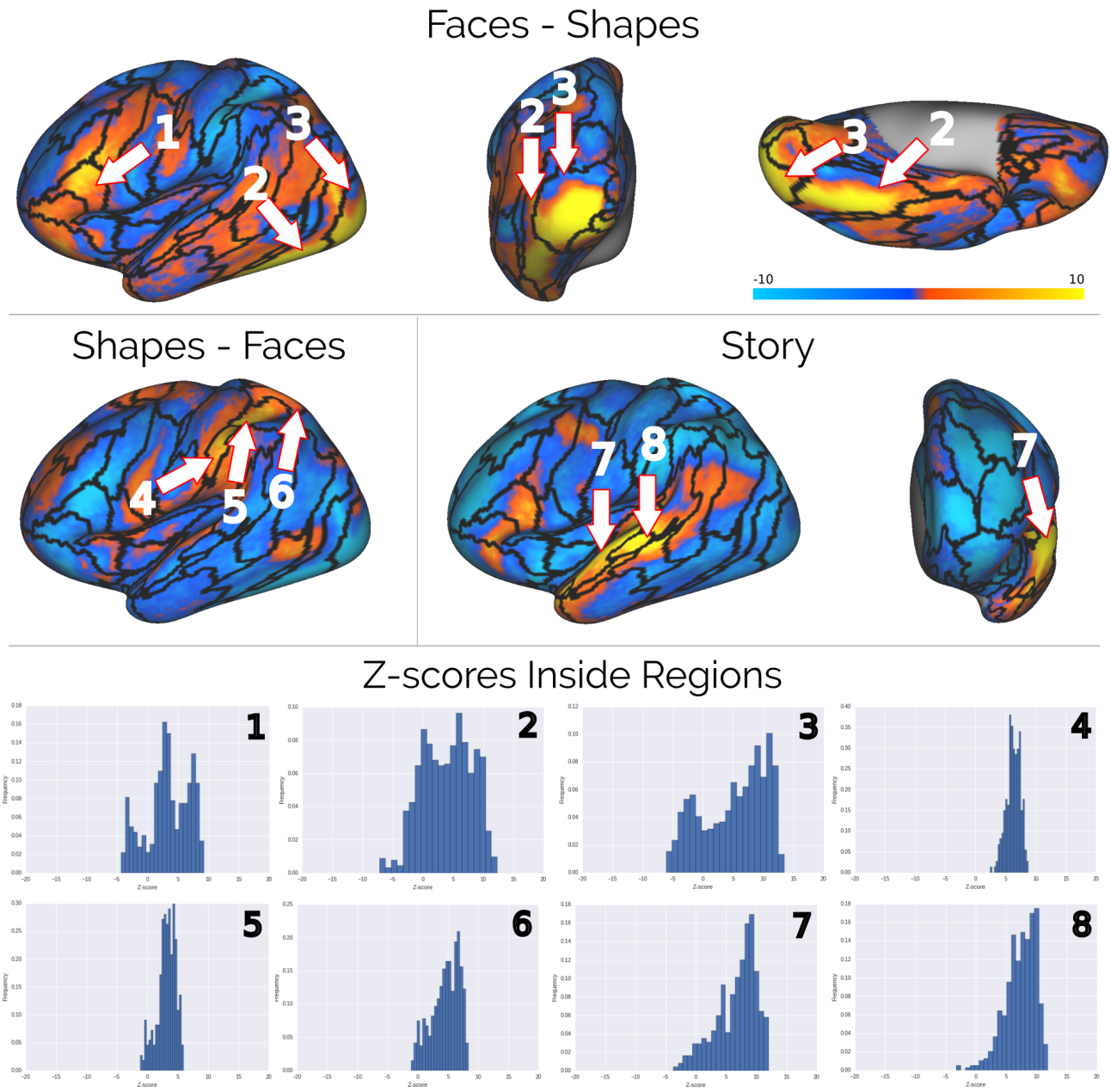

Figure 3.3: Our groupwise parcellation with 55 parcels projected over z-scores representing responses to cognitive tasks. Each histogram shows the distribution of z-score inside our parcels. The null or small fraction of negative values shows the functional specialization of our parcels

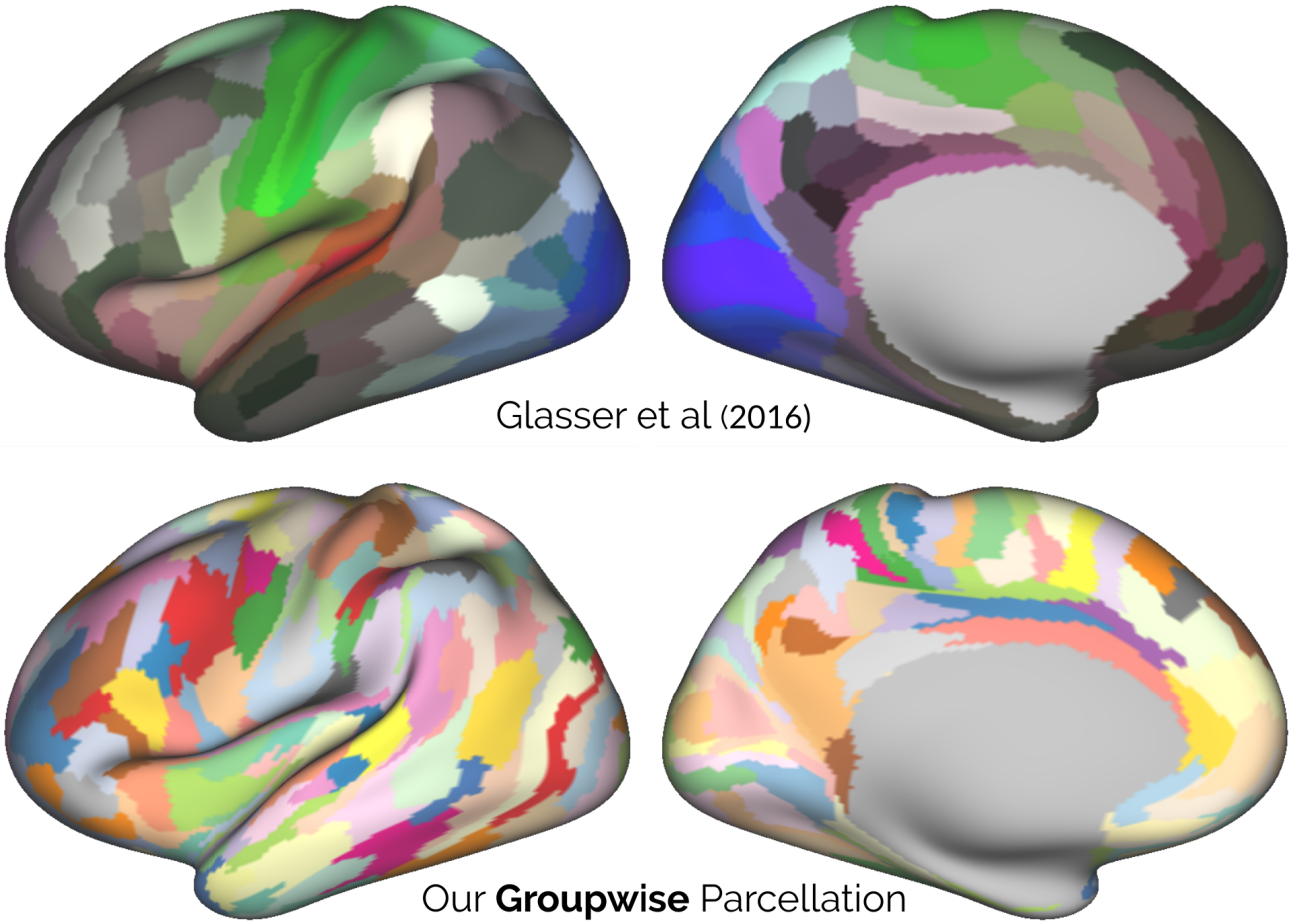

Figure 3.4: Glasser et al. (2016) parcellation (upper) and our groupwise parcellations computed from 138 HCP subjects. Both parcellations contain 180 parcels. There's almost no overlap according to the adjusted Rand index between them (0.28).

extrinsic connectivity, meanwhile those of Glasser et al. (2016) do not use dMRI information. Glasser's parcels are mostly based on myelin and functional information. In particular, their subdivision of the sensori-motor cortex (green parcels in Figure 3.4) is mostly based in Myelin maps as shown in Figure 4.a of Glasser et al. (2016). Because of this, their parcels in the sensori-motor cortex contain a wide range of z-scores when compared with responses to functional stimuli as shown by histograms a; b and c in Figure 3.5. In contrast, our parcels in the sensori-motor cortex, for a coarser parcellation, show a good overlap with function and are in agreement with the motor strip mapping as discussed in the previous section. Also, for the case of story categorization; shape recognition and face recognition, our parcels show a similar distribution of z-scores (Figure 3.2) than those with the highest mean z-scores of Glasser et al. (2016) (parcels d; e and f of Figure 3.5).

3.2 Conclusion

Understanding how the brain is structurally organized and its relationship with functionality is an open question in neuroscience. Recent advances in acquisition and modeling techniques on dMRI have

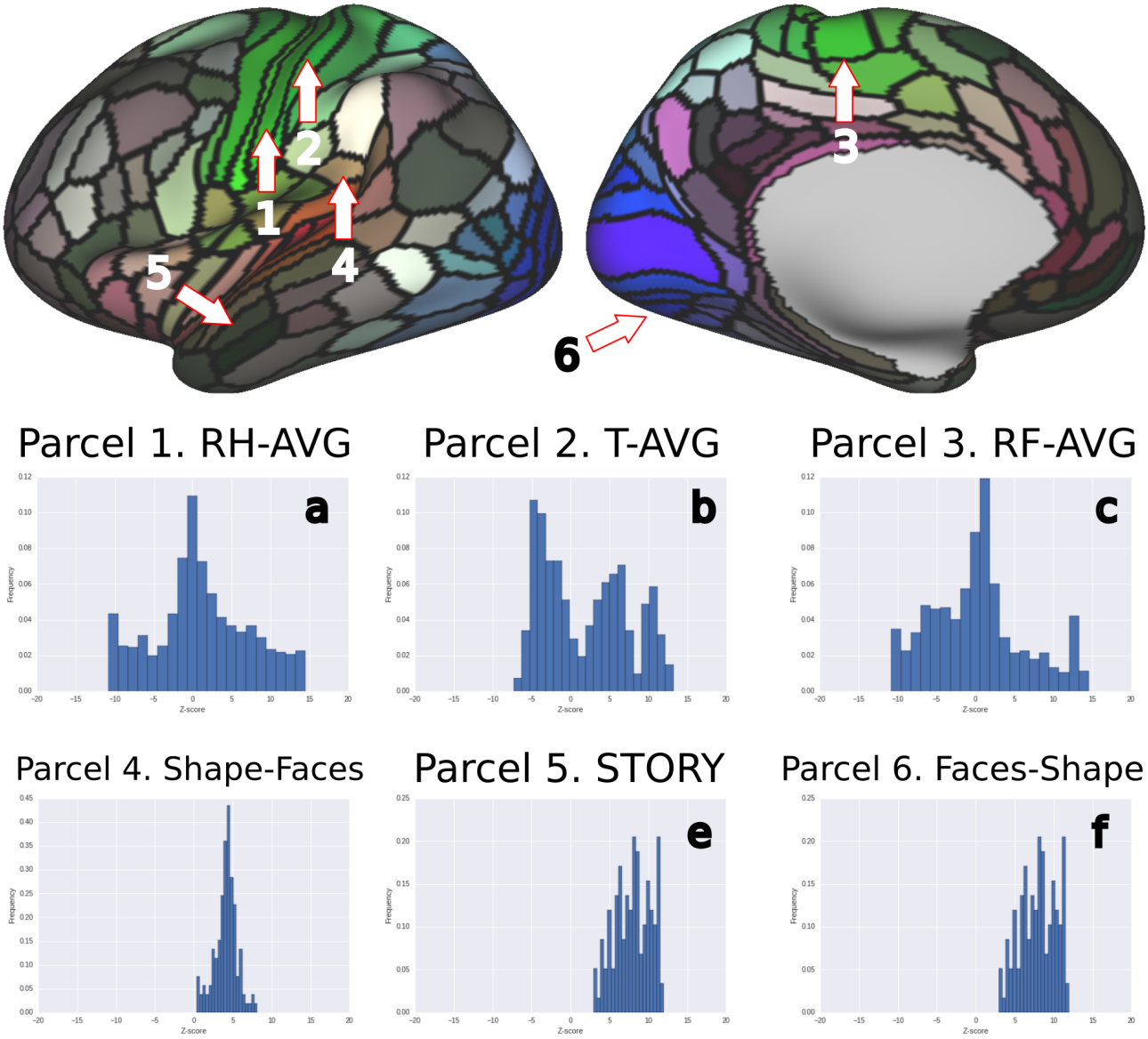

Figure 3.5: Glasser et al. (2016) parcellation (upper) and histograms of z-score contained in different parcels for different functional task. (a) Histogram for parcel 1 for the contrast related to Tongue movement. (b) Histogram for parcel 2 for the contrast related to Tongue movement. (c) Histogram for parcel 3 for the contrast related to Right Foot movement. (d) Histogram for parcel 4 for the contrast Shape recognition vs Face recognition. (e) Histogram for parcel 5 for the contrast related to Story Categorization. (f) Histogram for parcel 5 for the contrast Face recognition vs Shape recognition. The histograms (d); (e) and (f) correspond to the parcels with the greatest mean z-score of their respective tasks.

facilitated to study axonal connectivity in the brain. However, parceling the whole cortex based on a structural criterion remained challenging. In this work we presented a connectivity model; framed tractography within our model and presented a parceling technique that allows parcellation of the whole brain in both single subject and groupwise cases. Our technique, along with the obtained groupwise parcellation, could have major implications both in cognitive neuroscience and in development-aging studies. At the same time, our technique could help to lower the gap between structural connectivity and brain function, since some of our pure structural parcels showed good overlapping with responses to functional tasks.

Both our parceling tool and the obtained groupwise parcellation are or will be soon freely available in GitHub (`https://github.com/AthenaEPI/logpar`) and Neurovault. These tools provide a sound basis for new studies on human cognition, brain development, aging and disease. These tools can create fine parcellations of cortical areas, improving our knowledge about cortical organization. Future comparison with functional connectivity could lead to finally unraveling the link between axonal connectivity and brain function.

3.3 Second contribution: parcelling the White Matter, A History of Human-Centered Taxonomies

The task of subdividing the brain for better understanding and comprehension extends from the cortex to the white matter. Historically, the white matter, whose tissue is fibrous, has been divided into bundles of axons, or fascicles. These fascicles have been assigned numerous, non-concordant, names and taxonomies. Examples of the naming tradition variety are the uncinate fascicle (UF) from Latin *uncus* related to its hook shape; the inferior-longitudinal fascicle (ILF) whose name blends position and pathway descriptions; and Meyer's loop encompassing the name of a neuroanatomist studying it and its shape. Reflecting on the possibility that fascicles are but a useful construct, as they are rarely point-to-point axonal bundles (Schmahmann et al., 2006), we can derive the hypothesis that, differently to cortical parcellations, where we hope to find a set of parcellations based on cytoarchitecture, extrinsic connectivity, or function (von Economo et al., 1925; Amunts et al., 2015; Gallardo et al., 2017, and Section 3.1), the commonly used white matter parcellation and taxonomies are arbitrarily linked to the cumulative historical development of human neuroscience as a discipline (Schmahmann et al., 2007; Wassermann, 2010).

The main hypothesis of this contribution is that the large weight of human arbitrariness in white matter taxonomies constitutes a condemning factor machine learning approaches, generally based on pure geometry, that automatically dissect white matter fascicles from dMRI. There have been numerous contributions to this area using supervised and non-supervised methods(e.g. Wassermann, 2010; Wang et al., 2011a; Siless et al., 2018). Nonetheless, the results of these methods, instead of looking for a specific data-driven parcellation as is the case on the cortex (Amunts et al., 2015; Glasser et al., 2016; Yeo et al., 2016, see e.g.), have targeted the reproduction a specific humanly-derived taxonomy (e.g.

Table 3.5: Different descriptions of the uncinate fascicle in current literature.

Reference	Uncinate Fascicle Characterization
Catani et al. (2008)	[. . .] is a ventral associative bundle that connects the anterior temporal lobe with the medial and lateral orbitofrontal cortex.
Schmahmann et al. (2006)	[. . .] courses between the rostral temporal cortices and the ventral, medial and orbital parts of the frontal lobe.
Makris et al. (2008)	[. . .] extends between the anterior temporal lobe and the frontal lobe, where it spans medial and lateral regions (Dejerine et al., 1895). UF bridges the frontal temporal isthmus, passing in the floor of the insula, where its fibers interdigitate with gray matter islands in an area between anterior claustrum and the amygdala.
Fernandez-Miranda et al. (2008)	[. . .] forms the anterior part of the temporal stem and interconnects, in its most lateral portion, the fronto orbital region with the temporal pole

Catani et al., 2008). Under the hypothesis that there is no *true* dissection of the human brain white matter (see e.g. Axer et al., 2012), this contribution targets the development of a flexible system to define user-specific taxonomies and execute them on a dMRI dataset.

The ability to target specific tracts for quantitative analyses increases the statistical power and sensitivity of a study, compared to whole brain approaches, and simplifies the interpretation of results. However, such an approach requires precise and consistent delineation of the tracts across subjects. Although several fascicles, such as the cingulum bundle, are widely recognized and well defined in the field of neuroanatomy, there are others where the presence of the fascicles or subdivisions within fascicles is still a matter of discussion. For example, currently there are different systems for defining and subdividing the superior longitudinal fascicle (SLF) proposed by Catani et al. (2005) and Makris et al. (2005). There is also a discussion regarding the inferior occiptio-frontal fascicle (IOFF) in humans, and whether it even exists (Mandonnet et al., 2007; Schmahmann et al., 2007). Moreover, throughout the literature, the same fascicle is defined using different landmarks and techniques. This variability hinders the comparison between definitions. We show an example of this in Table 3.5, where we transcribe different definitions of the UF based on the current literature. A more comprehensive example of this problem is given by Axer et al. (2012) in their review of current studies of the dorsal and ventral language fascicles. Three major challenges make it difficult to extend and to reproduce streamline tractography-based dissections and tract-specific analyses: 1) the anatomical dissection of white matter into specific fascicles is currently a debate in the field; 2) comparing fascicle definitions across atlases is complicated by the lack of a system to unify the definitions; and, 3) semi-automated approaches are usually based on a fixed set of fascicles that are difficult to extend due to the high level of technical knowledge required.

The main contribution presented here is a system to define anatomical descriptions of white matter tracts in a near-to-English textual language (Wassermann et al., 2016). Specifically, a DSL to describe white matter neuroanatomy. Particularly, tract descriptions are written by the operator as text sentences which are then interpreted by a tool and can produce tract dissections from dMRI images. We designed this textual language to be easily human-readable; to make the tract descriptions easy to modify; and also to extend the descriptions of tracts without the need of an engineering background. Further, this query language can be used for automated virtual dissections of white matter. Thus, in developing this white matter query language (WMQL), we address the challenge of providing an extensible user-friendly tool for the automated dissection of human white matter from dMRI, as well as comparing definitions across the literature. Differently from current approaches (see e.g. Akers et al., 2004; Wakana et al., 2007; Yendiki et al., 2011) descriptions in WMQL are explicitly written as text. A software tool then interprets this text in order to extract tracts from a dMRI-tractography. The combination of our precise syntax specification for the WMQL queries with the software tool results in WMQL being a query language where the tract specifications are easily modularized and reused across different experiments. The WMQL proposed in this section has several applications. For example, Wakana's and Catani's definition of tracts using regions of interest (ROIs), can readily be represented using WMQL definitions. This yields a human-readable definition that also can be extended by an anatomist for a finer division. In designing the language this section, we produce definitions of the majority of human tracts described in the current literature and formulated using WMQL definitions (Wassermann et al., 2016). Our anatomy dictionary is composed of 10 association and 15 projection tracts per hemisphere, and 7 commissural tracts. An implementation of WMQL as well as the definitions specified in this publication can be downloaded at `http://demianw.github.com/tract_querier`

3.3.1 Methods

We designed WMQL such that the queries formalize current descriptions from anatomy literature. These descriptions are constructed in terms of different relationships between gyri, sulci, subcortical structures or white matter areas. The operations of WMQL can be divided into 3 groups: 1) **anatomical terms** stating if a tract traverses or ends in a certain brain structure, 2) **relative position** terms indicating whether the tracts are, for instance, medial or frontal to a structure like the amygdala, and 3) **logical operations** such as conjunction, disjunction or exclusion of the previous two types of clauses. We illustrate these three types of operations in Figure 3.6. Taking a closer look at the different descriptions of the UF in Table 3.5, it is possible to see that these descriptions can be unified in terms of the operation groups we introduced in Figure 3.6. That is, Schmahmann et al. (2006) and Catani et al. (2008) only state the two main areas connected by the tract, the anterior temporal lobe and medial and orbital sections of the frontal lobe. Makris et al. (2008), however, also point out that it passes through the floor of the insula through the area between the anterior claustrum and the amygdala. Further, Fernandez-Miranda et al. (2008) describe it as forming a part of the anterior subsection of the temporal stem. Unifying these descriptions, we conclude that the UF courses through the insula

and the lateral, medial, or orbital regions of the frontal lobe (Figure 3.6g) and has its endpoints in the anterior temporal lobe (Figure 3.6h). Using WMQL, we formalize this description and dissect the UF from a dMRI-tractography as illustrated in Figure 3.6i. (Figure 3.6 about here.) The overall goal of this paper is to generalize the process used to dissect the UF in Figure 3.6 into a tool: WMQL.

To apply WMQL queries to dissect dMRI-based tractographies, as seen in Figure 3.6, we need to locate gyri, sulci and other structures used for the queries relative to the white matter tracts. For this, we overlay an atlas of the brain structures on the tractography. In this work we used the cortical and white matter parcellation based on the Desikan atlas as described by Salat et al. (2009), and the neuroanatomic structure segmentation by Fischl et al. (2002). It is worth noting that WMQL does not depend on a particular atlas. In order to process queries in WMQL, each anatomical region is related to 8 sets of streamlines, namely the region's WMQL sets. These sets represent whether a tract has an endpoint in the anatomical region (Figure 3.6b); traverses the anatomical region (Figure 3.6c); or whether their position is relative to the anatomical region (Figure 3.6d-f). For example the amygdala's eight WMQL sets are:

endpoints_in(amygdala): all streamlines with at least an endpoint, i.e. the initial or final point of the streamline, in the amygdala.

amygdala: all streamlines traversing the amygdala.

anterior_of(amygdala), posterior_of(amygdala), medial_of(amygdala), lateral_of(amygdala), superior_of(amygdala), inferior_of(amygdala): containing the streamlines traversing brain areas defined by their relative position vis a vis the amygdala.

Having these WMQL sets per region, each one of the logical clauses in WMQL is defined in terms of set operations. For two WMQL sets a and b and the set of all streamlines L, we formalize the WMQL logical operations as follows:

$$\begin{aligned} a \text{ or } b &\triangleq \{\text{tract} : \text{tract} \in a \cup b\} \\ \text{only}(a) &\triangleq \{\text{tract} : \text{tract} \in a \wedge \text{tract} \notin (L - a)\} \\ a \text{ and } b &\triangleq \{\text{tract} : \text{tract} \in a \cap b\} \\ a \text{ not in } b &\triangleq \{\text{tract} : \text{tract} \in a \wedge \text{tract} \notin b\} \\ \text{not } a &\triangleq \{\text{tract} : \text{tract} \notin a \wedge \text{tract} \in L\} \end{aligned} \tag{3.8}$$

We have illustrated these operations in Figure 3.6. Tracts in WMQL are defined by using an assignment operation, for instance, we defined the left UF in Figure 3.6i as assigning a meaning to UF.left:

> UF.left = insula.left and (lateral frontal.left or medial frontal.left or orbitofrontal.left) and endpoints_in(temporal.left and anterior_of(amygdala.left)) not in hemisphere.right

To simplify the definitions of tracts in both hemispheres with a single assignment, we included the suffixes ṡide and ȯpposite to WMQL. Creating a bihemispheric definition becomes:

> UF.side = insula.side and (lateral frontal.side or medial frontal.side or orbito frontal.side) and endpoints_in(temporal.side and anterior_of(amygdala.side)) not in hemisphere.opposite

In this way, WMQL allows a single definition for tracts found in both hemispheres simultaneously. The formalization of WMQL as the basic set operations allows us to define white matter tracts using all the flexibility and expressive power of set theory and propositional logic.

The main challenge in the implementation of WMQL as a software tool is to be efficient enough to evaluate the queries on large tract datasets, such as those containing more than a million streamlines. In particular, we need to efficiently calculate the WMQL sets for each region. To achieve this we build a spatial index of the whole set of streamlines by means of an axis-aligned boundary box tree or AABB-tree. We refer the interest reader to the work by Wassermann et al. (2016) for details regarding the implementation of the spatial indexing. This spatial indexing is an efficient way to calculate which streamlines are candidates of each region's 8 WMQL sets (see Figure 3.6). Using axis-aligned boundary box (AABB) the WMQL sets for each brain region are calculated and the textual WMQL queries efficiently evaluated.

We have conceptually described WMQL. The finer implementation details of the WMQL process to interpret queries and use them to dissect tracts are described in the work by Wassermann et al. (2016) where a historical review of the all tracts included in the chosen proof-of-concept taxonomy can also be found as well as the full description of the tracts in WMQL. To show an example of WMQL, we transcribe below the description for two tracts and show their WMQL definitions in Table 3.6.

Corpus Callosum, rostrum (CC1) The CC is the largest commissure in the human brain. Several systems of subdivision of the callosal commissure have been proposed in the human (e.g. Witelson, 1989), which have been adopted for morphometric MRI studies. Diffusion imaging has currently made it possible to delineate a considerable portion of these fibers in vivo. We present the rostral section of the CC as proposed by Witelson (1989) which connects the orbitofrontal gyri.

Superior Longitudinal Fascicle I (SLF I) SLF I is situated within the dorsal medial white matter of the hemisphere lateral to the cingulate and paracingulate sulci and extends further rostrally into the white matter of the superior frontal gyrus. SLF I connects the superior parietal gyrus the middle and superior frontal gyri (Makris et al., 2005; Thiebaut de Schotten, 2005).

Having presented the core of WMQL as a tool to formalise white matter tract descriptions and extract them from tractography datasets, we proceed to the experiments and discussion of this contribution.

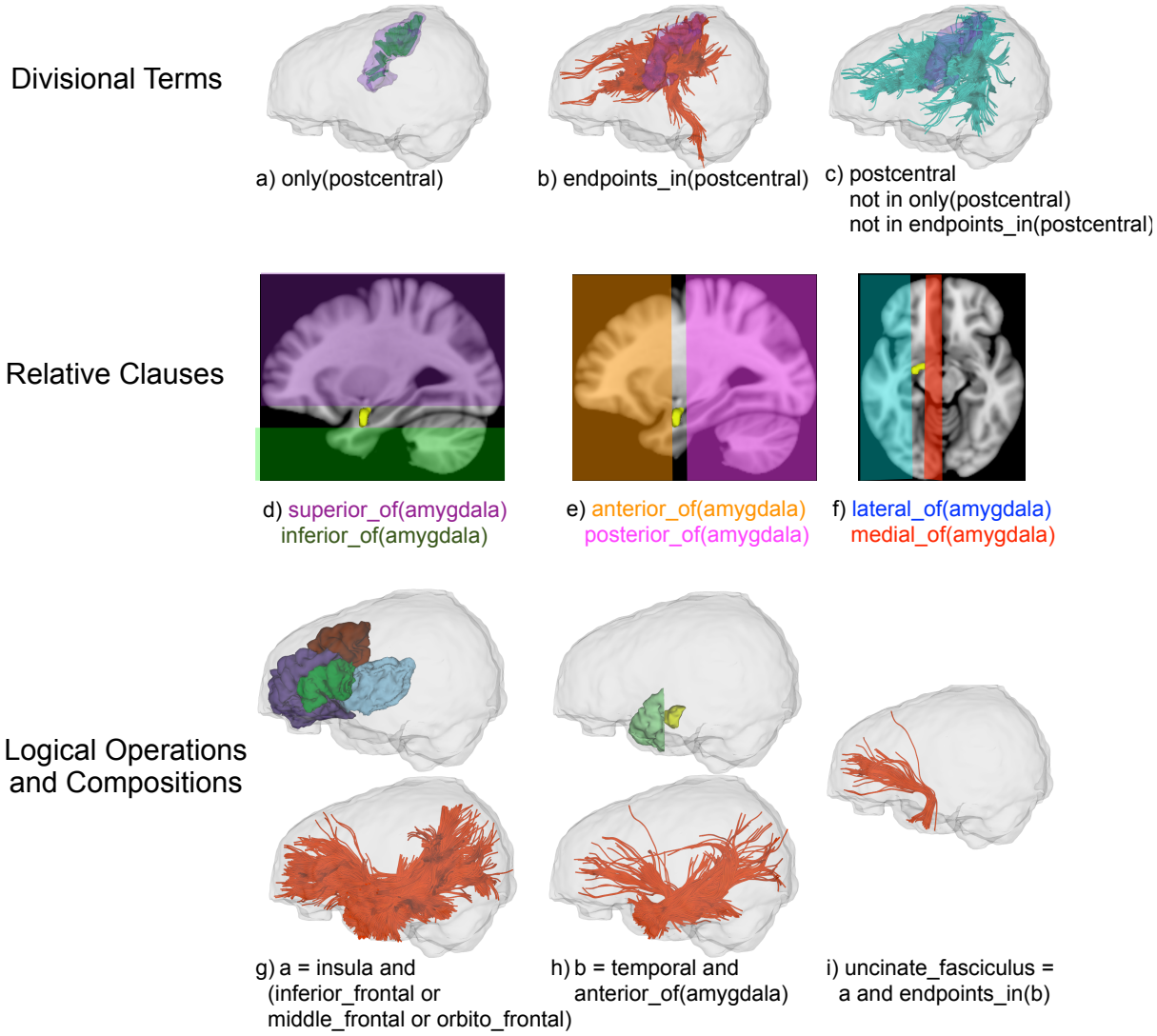

Figure 3.6: WMQL Terms (a-f) along with an example construction of a WMQL query (g-i). Regions in (g-i): insula (cyan); the orbito-frontal (purple), middle-frontal (brown) and inferior-frontal (dark green) convolutions. (h) shows the anterior temporal lobe (light green) defined as the section of the temporal lobe anterior to the amygdala (yellow).

Table 3.6: Example of WMQL queries extracted from 57 tracts defined by Wassermann et al. (2016)

Tract Name	WMQL Query
Rostrum of the Corpus Callosum	CC_1 = endpoints_in(orbitofrontal.left) and endpoints_in(orbitofrontal.right)
Superior Longitudinal Fascicle I	SLF_I.side = endpoints_in(superior_parietal.side) and (middle_frontal_gyrus.side or superiorfrontal.side) and only(frontal.side or parietal.side or centrum_semiovale.side)

3.3.2 Experiments and Discussion

Comparison with manual approach

To assess the accuracy of WMQL as a tract extraction algorithm, we compared our implementation with a set of 5 tracts manually delineated using the procedures specified by Catani et al. (2008): 4 association and one projection tract. We randomly picked 10 subjects from our healthy cohort. On each subject, 2 different experts segmented 5 tracts: IOFF; UF; ILF; cortico-spinal tract (CST); and arcuate fascicle (AF). Tracts were traced in both hemispheres following the manual delineation protocol. In parallel, we used the WMQL definitions in by Wassermann et al. (2016, Section 2.1) to extract the same tracts automatically. Finally, we quantified the overlap between the manually segmented tracts and the ones automatically extracted using WMQL using the kappa measure (Cohen, 1960). The kappa measure (κ) quantifies inter-rater agreement for qualitative items assigning a score between 0.00 and 1.00. Landis et al. (1977) established the following guidelines for its interpretation: a value within the range 0.11–0.20 is considered as "slight", 0.21–0.40 as "fair", 0.41–0.60 as "moderate", 0.61–0.80 as "substantial", and 0.81–1.00 as "almost perfect" agreement.

Overlap across both of our raters, calculated with the kappa measure, was $\kappa \geq 0.76$ for all tracts, considered substantial agreement, the worse being the right AF ($\kappa = 0.76$) and the best the left ILF ($\kappa = 0.90$). Overlap between the manually segmented tracts and the ones extracted using WMQL was $\kappa \geq 0.71$ for all tracts, which is considered substantial agreement. The worse was the left AF ($\kappa = 0.71$) and the best the left CST ($\kappa = 0.89$). When compared with inter-rater κ-scores the WMQL ones were slightly lower (mean κ difference = 0.033 ± 0.020) with the worst case being the left AF (difference of 0.08) and the best being the left CST and IOFF (difference of 0.01).

Our results showed the WMQL overlap to be close, albeit always lower, to the inter-rater one as well as high consistency with each rater (Cohen's $\kappa > 0.7$) for all tracts, the worst being the left AF and the best being the left CST. The origin of this discrepancy can be traced to the fact that the ROI procedure proposed by Catani et al. (2008) was designed for DTI-based tracts. These methods are more conservative than the tractography method used in this study, and they yield a smaller number of true and false positives. Hence, the result of this procedure on our dataset, which uses HARDI-based tractography, results in noisier delineated tracts. Upon visual comparison with dissection-based studies (Wassermann et al., 2016, Table 5) the WMQL results more closely resemble the dissections than those

based on Catani's procedure. All in all, our results proved of comparable accuracy with manually traced fascicles following well-established procedures.

White Matter Atlas Generation with WMQL

The goal of this experiment is twofold: first, it shows the across-subject overlap of our automatic tract extraction pipeline; second, it generates a volumetric atlas that can be used for reference or population studies.

Using our WMQL fascicle definitions (Wassermann et al., 2016, Section 2.1), we constructed a volumetric atlas of white matter tracts based on multi-tensor tractography. The combination of WMQL with multi-tensor tractography and our acquisition protocol enabled us to generalize previous atlases (e.g. Wakana et al., 2004; Catani et al., 2008) and extend them with white matter tracts not included in these. Examples of these tracts are the middle longitudinal fascicle (MdLF) and the three different superior longitudinal fascicles. In total, our atlas includes 10 long association tracts; 15 projection tracts per hemisphere (7 cortico-striatal, 7 cortico-thalamical and the cortico-spinal tract) and the 7 sections of the corpus callosum according to Witelson (1989)

To generate a volumetric tract atlas we acquired a high angular resolution dMRI (HARDI) dataset of 77 healthy subjects (32.9 ± 12.4 years old of age; 64 males; right-handed) and registered them to the MNI template (see Wassermann et al., 2016, for details). Then, we extracted, for each subject, 57 white matter tracts using WMQL definitions (Wassermann et al., 2016, Tables 2, 3 and 4). Simultaneously, we normalized the FA maps of each subject to MNI space, and created a population FA template using ANTS (Avants et al., 2006). Then, we generated group effect maps for each tract (Thiebaut de Schotten et al., 2011b). To obtain the group effect maps, we started by calculating a binary visitation map for each tract of each subject. This map is a mask in MNI space where a voxel has a value of 1 if the tract traverses that voxel and 0 if not. We created the group effect map for each tract through voxel-wise statistics. The group effect map assesses the probability that a tract traverses each voxel. For this, we rejected the null hypothesis that such tract does not traverse that voxel. We first smoothed the visitation maps with a 2mm (FWHM) isotropic Gaussian to account for the uncertainty in spatial location of resulting tractographies. This has the effect of reducing the importance of voxels traversed by stray streamlines while keeping constant that of voxels belonging to a region densely traversed by the tract. Then, we rejected the hypothesis that the voxel does not belong to the tract, i.e. the mean traversal value over all subjects on that voxel is different to 0, by using a voxel wise t-test for a one-sample mean. We calculated the significance corrected for multiple comparisons using permutation testing (10,000 iterations) to avoid a high dependence on Gaussian assumptions across subjects (Nichols et al., 2002).

Across-subject overlap of our automatic tract extraction pipeline shows tract volumes in agreement with current literature in white matter anatomy. The whole set of 57 tracts was extracted from each subject from a whole brain tractography consisting of 2 million tracts in less than 3:40 minutes (±10 seconds) for each subject on a notebook (2.6 GHz intel Core i7, 16 GB memory; we show the speed of WMQL on

one of these subjects in a video (Wassermann et al., 2016, Online Resource 1). The visitation maps of the tracts extracted on each subject separately show a high overlap when superposed in MNI space (p-value < 0.0001 corrected for multiple comparisons using permutation testing). Figure 3.7 (commisural and cortico-thalamic shown in Wassermann et al., 2016, Figure 5) shows, for every tract association tract and the CST, the surfaces where the visitation maps of all 77 subjects overlap at a p-value = 0.0001. Moreover, these surfaces constitute volumetric atlas of white matter tracts for our healthy sample.

Although the tracts reported in this study were present in all 77 healthy subjects, we found variability in their locations and trajectories. A higher variability, depicted as a smaller volume in Figure 3.7, was found in the right hemisphere on the MdLF and extreme capsule fascicle (Ec) and on the left hemisphere on the superior longitudinal fascicle I (SLF I). For all these cases, decreasing the significance threshold from $p < 0.0001$ to $p < 0.01$ showed volumes consistent with dissection-based studies, available in the case of the association tracts (see the references in Wassermann et al., 2016, Table 5).

The inter-individual variability we observed for each tract possibly reflects differences in tract volume and pathway. Biological factors such as axonal density, diameter and myelination are factors known to modulate the diffusion signal and are possible sources of the inter-individual variability at a microstructural level (Beaulieu, 2002). Age, gender and handedness can also be sources of this variation (Thiebaut de Schotten et al., 2011b; Lebel et al., 2012). However, other methodological explanations should be considered. Though the warping technique we used to normalize the brains into MNI space has been shown to be highly reproducible, it may produce small errors in the alignment (Avants et al., 2011). Such errors, even if they are small are likely to introduce variability in the group effect maps of the tracts. Another source of this variability is the intrinsic error in the tractography algorithms. For example, all tractography algorithms suffer from problems due to error accumulation along the traced tracts (Lazar et al., 2003), which might lead to a high variability in longer tracts.

The White Matter Query Language: Advantages and Limitations

Few approaches have formalized the descriptions of fascicles, which comprise the white matter of the human brain using data from dMRI. Wakana et al. (2004) and Catani et al. (2008) have used manually placed ROIs to guide the tractography or tract-selection in the brain, but find a major limitation in reproducibility. This is not surprising given that ROI placement is completely dependent on the operator's judgment thus leading to concerns about the intra-and inter-operator reproducibility (Catani et al., 2008; Zhang et al., 2010). This limitation results in large variability for tract-tracing procedures affecting the results of posterior analyses. Several approaches have been proposed to solve these problems, relying on fixed definitions and simple but robust procedures (e.g. Yendiki et al., 2011; Yeatman et al., 2012), on clustering approaches (e.g. Wang et al., 2011a), or on a combination of the former two techniques (e.g. O'Donnell et al., 2007; Wassermann et al., 2010; Siless et al., 2018). Although these techniques effectively solve the reproducibility problem, they are still limited by two

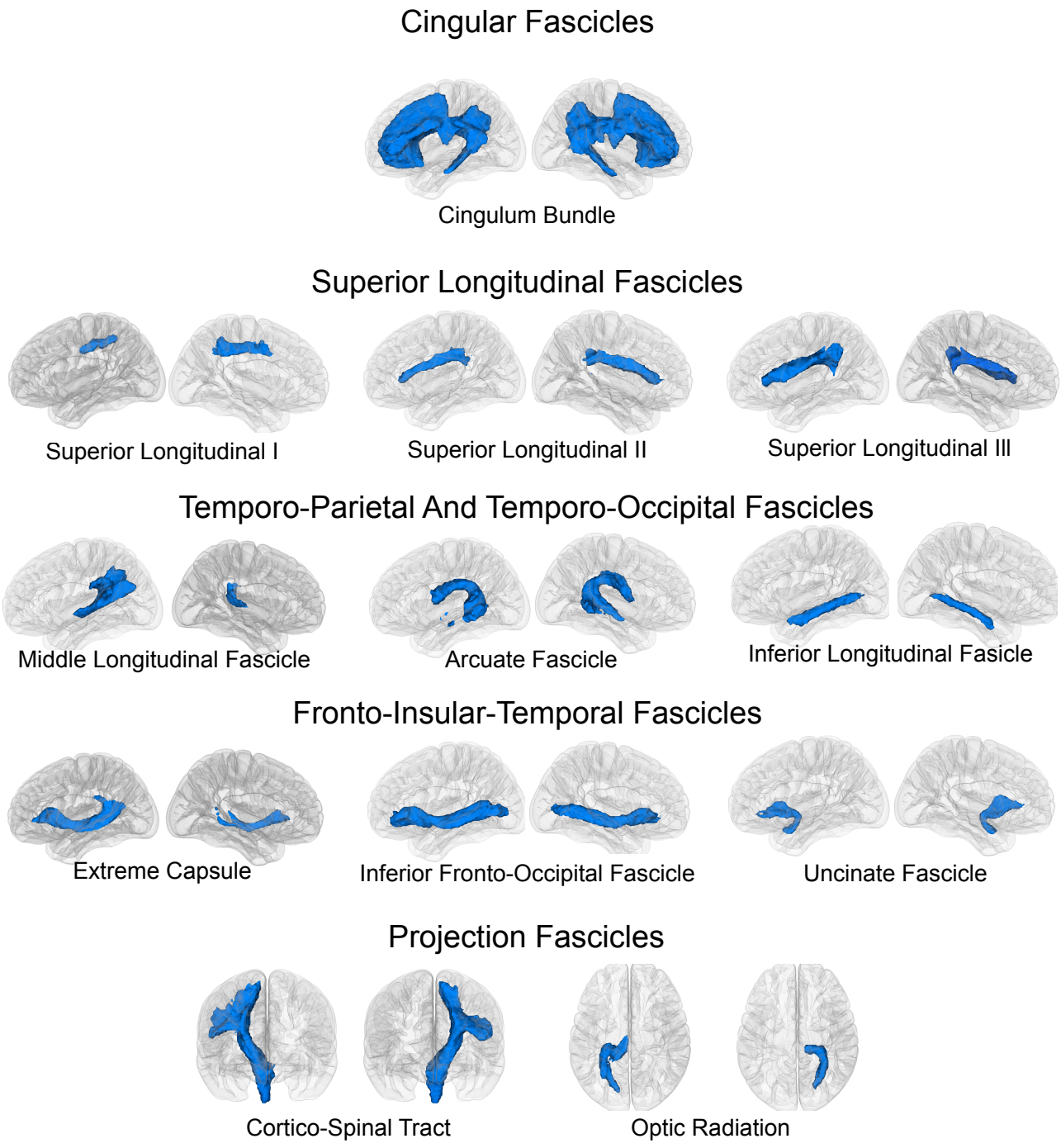

Figure 3.7: As colored volumes, we show the iso-surfaces at p-value = 0.0001 (corrected for multiple comparisons) corresponding to 10 association tracts and 2 projection ones.

main issues:

1. Operator experience: the system is critically dependent on the level of technical proficiency of the operator. This involves the anatomical knowledge to define the white matter tracts or on the technical knowledge to fine-tune the clustering approaches, which may vary considerably.

2. These systems have been designed for a specific set of white matter tracts. However, many of these definitions are still in discussion.

These requirements limit the breadth of the studies that can be performed using these techniques.

Using the WMQL approach, anatomical knowledge is represented as near-to-English queries derived from textbook definitions. This can be seen, for example, in reviewing current definitions for association tracts and their corresponding WMQL queries (Wassermann et al., 2016). The fact that our system is in near-to-English formalizations of anatomical descriptions reduces the need for technical knowledge of the operator, and the comprehensive set of definitions provided by Wassermann et al. (2016) serves as a powerful complement to the operator's anatomical proficiency (issue 1). WMQL is also useful in cases in which the definitions change, or a tract that has not been catalogued in this paper is needed for a study. In these cases, the description of the tract can be translated into a WMQL query in order to automatically extract it from a dMRI image (issue 2). Furthermore, WMQL is independent of the choice of atlas or brain parcellation and can be used with study-specific defined ROIs and a set of newly defined queries. With respect to the set of logical operations included in ROI-based approaches (e.g. Catani et al., 2008; Zhang et al., 2010), the inclusion of the operations only, endpoints_in and the relative positioning terms, see Figure 3.6, improves the expressive capabilities of WMQL allowing for more flexible definitions. The unique trait of WMQL is the possibility to write the queries in a text file or script that then can be used across studies and easily adapted. These definitions can attain a high complexity level, while remaining readable. Once written, reused on a different dataset by, preprocessing it and using a previously written script with the WMQL definitions. This renders WMQL a flexible system to define white matter fascicles in terms of brain areas and extract them from dMRI images. Finally, a recent independent study by Zhang et al. (2019) has shown that, for the same set of tracts and in three large publicly available databases, machine learning-based methods and WMQL enjoy comparable reproducibility. Furthermore, WMQL and a clustering-based method have been recently combined to produce an anatomically-curated white matter atlas over the lifespan (Zhang et al., 2018)

There are two important limitations, however, in the proposed approach. First, the results rely on the quality of the tractography algorithm outputs, which, in turn, depend on the dMRI image preprocessing and the choice of algorithm itself. An algorithm that yields traces that are not anatomically feasible, or false positive streamlines which have shown to be common (Maier-Hein et al., 2017), will result in noisier extracted fascicles; one that yields a very limited amount of curves will yield sparse extracted

fascicles. Second, the results rely on the accuracy of the parcellation of the selected subject's brain; if the parcellation does not contain a segmentation of a brain structure of interest, a trajectory of such an area cannot be specified. However, the possibility of specifying a region as a combination of anatomical and relative position terms often overcomes this problem.

CHAPTER 4

Selected Applications: Unveiling the relationship between Brain Structure, Cognition, and Diagnosis

In this chapter we present two selected applications spanned from methodological contributions previously presented. The first one, wielding the power of RTOP as a measure modulated by cellular size in the human insular cortex using MAPL (Section 2.3), enables us to predict cognitive abilities. The second one, based on WMQL (Section 3.3), enables the fine subdivision of the motor pathways in Huntington's disease (HD) and linking imaging markers with genetic predictors of functional decay.

4.1 Quantitative RTOP analysis reveals microstructural organization of human insula and predicts cognitive control

The human insular cortex plays a critical role in identifying salient sensory, affective, and cognitive cues for guiding attention and behavior (Nimchinsky et al., 1999). Dysfunction of the human insula and its interconnected regions are now thought to be core features of several psychiatric and neurological disorders (Goodkind et al., 2015; Namkung et al., 2017). The insula has a distinct cytoarchitectonic profile, characterized by less differentiated cortical layers (Nimchinsky et al., 1999). Thus far, investigations of the distinct structural features of the human insular cortex have been based solely on postmortem brains and have not been amenable to characterization using non-invasive brain imaging techniques. Consequently, little is known about the normative microstructural organization of the human insular cortex and its relation to behavior.

The insular cortex is a structurally heterogeneous brain region. Its cytoarchitectonic organiza-

tion has been investigated using histological techniques over the last century by several prominent anatomists (von Economo, 1926; Allman et al., 2010). Stereological analyses of the insula have identified a cellular cortical architecture which differs considerably from the 6-layer granular architecture seen in most cortical areas (Mesulam et al., 1985; Vogt et al., 1995). In a seminal study conducted over three decades back, Mesulam et al. (1985) proposed the concept of "granularity", based on the presence of an inner granular layer, composed of small granule neurons, as a key feature for identifying the anatomical subdivisions of the insular cortex. In the ensuing years, several histological studies (Allman et al., 2010; Morel et al., 2013) have focused on demarcating the microstructural properties of insular subdivisions but no consensus has yet emerged about their precise boundaries because of small sample sizes, limited insular divisions examined and high degree of variability across individuals. Non-invasive brain imaging measures are therefore critically needed to address this major gap.

Despite the lack of consistency and precision across previous histological studies, some general patterns have emerged regarding the general cytoarchitectonic organization of the insula. The ventral-anterior insula (vAI) has an agranular structure characterized by undifferentiated layers II/III and without a fully expressed layer IV compared to the fully developed granular cortex with a canonical 6-layer architecture. The dysgranular cortex has an intermediate profile that has been mainly observed in the dorsal anterior aspects of the insula (Kurth et al., 2010). In contrast, large sections of the posterior insula show a canonical granular structure (Kurth et al., 2010). A unique aspect of the neuronal organization of the human insula is the presence of Von Economo neurons (VENs) that are present in the anterior aspects of the insula (Namkung et al., 2017). VENs are projection neurons that differ from the typical pyramidal neurons by virtue of their large spindle shape and thick basal and apical dendrites (Seeley et al., 2012), which allow for speeded communication. The presence of VENs in the human insula is thought to contribute to its unique and important role in goal-directed behaviors and emotional regulation, through rapid processing of attentional, cognitive, interoceptive, emotional, and autonomic signals (Craig, 2009). The lack of tools for assessing morphological alterations in the insula in vivo and its relation to behavior has limited our understanding of the microstructural organization of the insula in health and disease.

Here we exploit recent advances in multi-shell dMRI acquisition protocols and MAPL (Fick et al., 2016a, Section 2.3) to determine the microstructural features of insular cortex using the normalized RTOP density index (Mitra et al., 1995). The first aspect of our study involved leveraging a large (N = 440) cohort of adult participants from the HCP, we evaluated RTOP across three major functional subdivisions of the human insula and demonstrate that they are microstructurally distinct with profiles consistent with its known agranular, dysgranular and granular organization. Finally, we examine whether variation in microstructural features of the insula are related to behavior and individual differences in cognitive control ability. Stability and cross-validation analysis are used to demonstrate the robustness of our findings.

4.1.1 Results and Discussion

To assess whether RTOP is a subsidiary measure for cytoarchitecture, we analysed RTOP over the insula from 440 participants -36 years old, 261 female/179 male) was obtained from the HCP Q1–Q6 Data Release. In line with the monkey experiment in Section 2.3, we computed RTOP using MAPL to account for dMRI image noise. The regularization parameter was selected through generalized cross validation and the Return-To-Origin probability was computed analytically from the fitted MAPL parameters. Finally, to render the RTOP probability comparable across subjects, we normalized it by the average ventricular RTOP of each subject's cortico-spinal fluid in the ventricles. In this way the normalized RTOP quantifies the enhancement ratio over free diffusion (Mitra et al., 1995) specific to each subject.

Normalized RTOP reveals insula microstructural gradients along the anterior-posterior and dorsal-ventral axes

To delineate the microstructural organization of the human insula, we conducted a detailed profile analysis and used directional statistics to characterize gradients in RTOP along its anterior-posterior and ventral-dorsal axes (Figure 4.1).

For this, we projected the volumetric normalized RTOP of each subject over the vertices of a mesh representing the insular cortex by following HCP's methods. To assess if the normalized RTOP values follow the anterior-to-posterior and inferior-to-superior cytoarchitectonic organization of the insular cortex, we computed the normalized RTOP gradient field along the insular surface of each subject. For each gradient, we estimated its main direction alongside a confidence interval (significance $\alpha = 0.05$) based on the von Mises-Fisher distribution (Kanti V Mardia, 2000). If the normalized RTOP has a directional organization within each subject, then the confidence interval of each subject's main direction should be small. To assess that the main gradient directions obtained for each subject were following a common direction, their mean and its confidence interval was computed. Furthermore, we used a Rayleigh test to reject the hypothesis that the subjects' main gradient directions were uniformity distributed. To investigate normalized RTOP organization at a finer level, we repeated the estimations made along the whole insular cortex in each of the three functional subdivisions. For each subject, we first estimated the main gradient direction and its confidence interval within each subdivision. Then, to study the consistency between the obtained directions, we computed their mean direction alongside a confidence interval, and we used the Rayleigh test to reject the hypothesis that they were uniformity distributed.

Figure 4.1A shows isolevels of normalized RTOP values in the insula at a group level. We found a low dispersion of normalized RTOP gradients in both the left ($0.18\pi \pm 0.09\pi, SEM = 0.005$) and right ($0.23\pi \pm 0.10\pi, SEM = 0.005$) hemispheres. We then assessed the significance of this finding using the Rayleigh test, against the null hypothesis of a uniform directional distribution. We found strong evidence for both anterior-to-posterior and ventral-to-dorsal gradient in the left insula (ci = 0.02π,

Rayleigh statistic = 982, p < 1.0e-10, N=440, df=3) and a ventral-to-dorsal gradient in the right insula (ci = 0.03π, Rayleigh statistic = 628, p < 1.0e-10, N=440, df=3).

We found strong evidence that normalized RTOP is sensitive to the cytoarchitectonic organization on the insular cortex. Specifically, normalized RTOP gradients are consistent with the granular, agranular, dysgranular insular subdivisions driven by a cortical layer populated with VENs. When analyzing the functional subdivisions, the confidence intervals of their subject's main direction showed a low dispersion in the gradient field directions. This is the direction on the normalized RTOP gradients of the functional subdivisions shown to be consistent within participants. At the group level, we found strong evidence of an anterior-to-posterior and ventral-to-dorsal gradient in each subdivision of both the left insula and the right insula (Figure 4.1B-C). Again, the confidence interval showed a low dispersion, indicating a consistent pattern of gradients across participants. The lowest values of normalized RTOP were localized to the vAI (Deen et al., 2011).

Analysis of microstructure isolines further revealed gradient 'fingers' from the vAI extending along a ventral-dorsal axis. This pattern is strikingly consistent with findings from known cytoarchitectonic features in the insula derived from studies of post-mortem brains (Allman et al., 2010). The vAI regions where we observed the largest cell size (lower normalized RTOP) is also consistent with histological studies that have found the highest density of VENs in this region (Figure 4.1D).

In sum, the anterior-posterior-ventral-dorsal gradients and the convergent findings from the three distinct functional subdivisions provides new quantitative insights into the microstructural organization of the human insular cortex. The precise anatomical boundaries of the agranular, dysgranular, and granular architectonic areas within the human insula are not known, and differences in stereological methods and criteria have led to different segmentation schemes of the insular cortex in primates (Roberts et al., 1970; Paxinos et al., 2000). However, there is general consensus that the anterior and most of the mid insula areas are agranular or dysgranular while the posterior most aspects are granular (Namkung et al., 2017). The spatial gradient of normalized RTOP in the insular cortex along the dorsocaudal-rostroventral axis provides new metrics for noninvasive in vivo analysis of the general cytoarchitectonic organization in the insular cortex in the human brain and is an advance over previous studies that have thus far been based on invasive histological and electrophysiological data of human and non-human primates (Allman et al., 2010; Evrard et al., 2012; Evrard et al., 2014).

Insula microstructure predicts cognitive control ability

The human insula has been implicated in a broad range of cognitive functions (Nimchinsky et al., 1999; Menon et al., 2010; Uddin, 2015), but links between its microstructural features and individual differences in cognitive control abilities have not been previously examined. We used CCA with cross-validation and prediction analysis to investigate the relationship between microstructural properties of the insula and cognitive control ability.

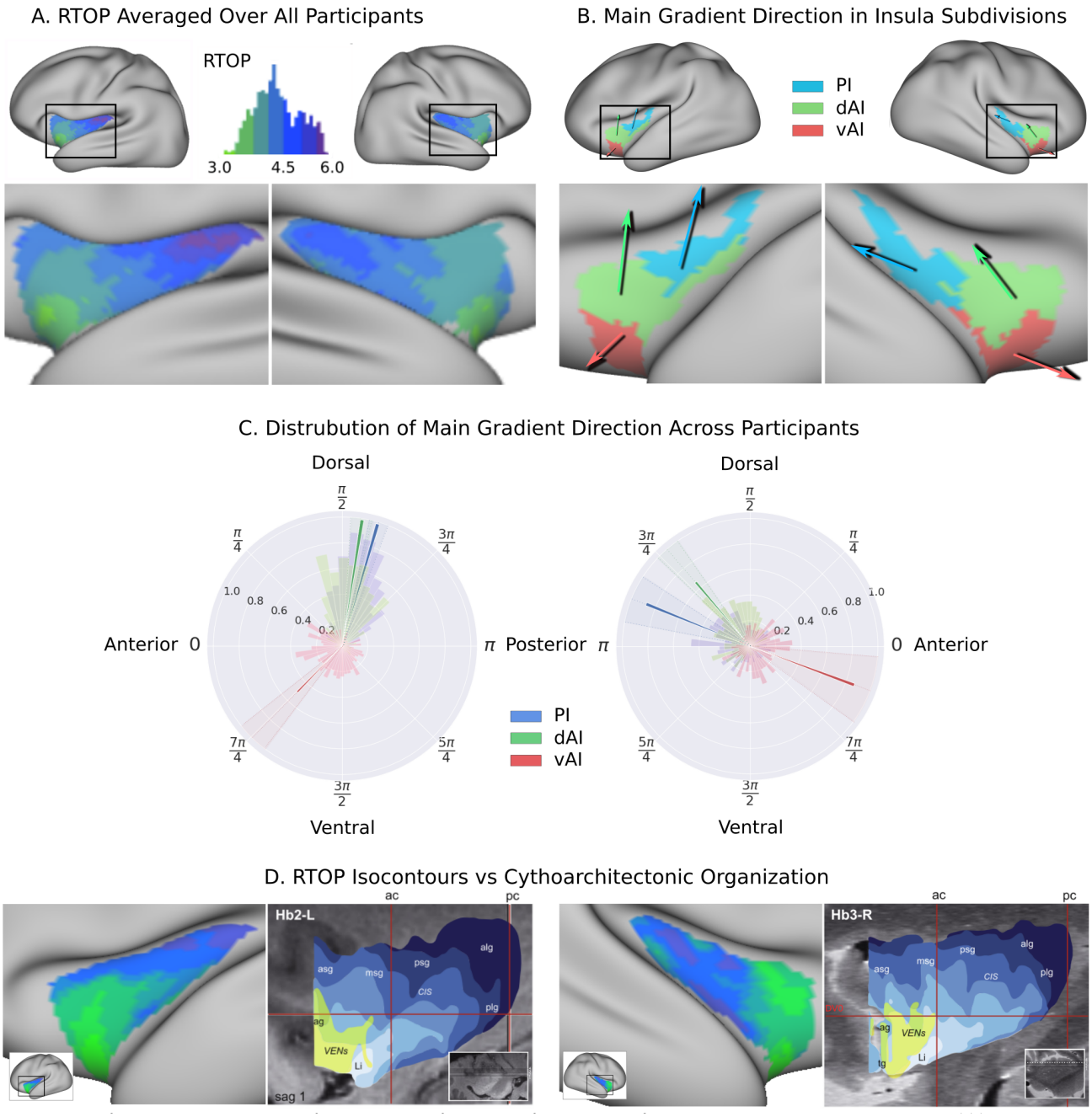

Figure 4.1: Insula microstructure gradients along its anterior-posterior and dorsal-ventral axes. (A) RTOP averaged over all participants (N=440) illustrates inhomogeneity in insula microstructure with a vAI peak, and gradients along the anterior-posterior and dorsal-ventral gradients axes. Larger RTOP indicates smaller average compartments. There is a prominent gradient from the insular pole towards the posterior insular section. Note right hemisphere dominance. (B) Main gradient direction, computed using Rayleigh directional statistics in each functionally defined subdivision: vAI, dAI, PI (Deen et al., 2011). The main directions show an anterior-to-posterior and inferior-to- superior RTOP organization in the left insular cortex and an anterior-to-posterior organization in the right insular cortex. The polar plots show the distribution of main gradient directions in each functional subdivision. (C) Gradient direction histograms. The mean direction is represented with solid lines on top of the distribution histogram; the shaded region represents the 95% confidence interval. (D) Isocontours of the population-average RTOP (left) are closely aligned to cytoarchitectonic organization of the insula and VEN expression from studies of post-mortem brains (right, from Morel et al., 2013).

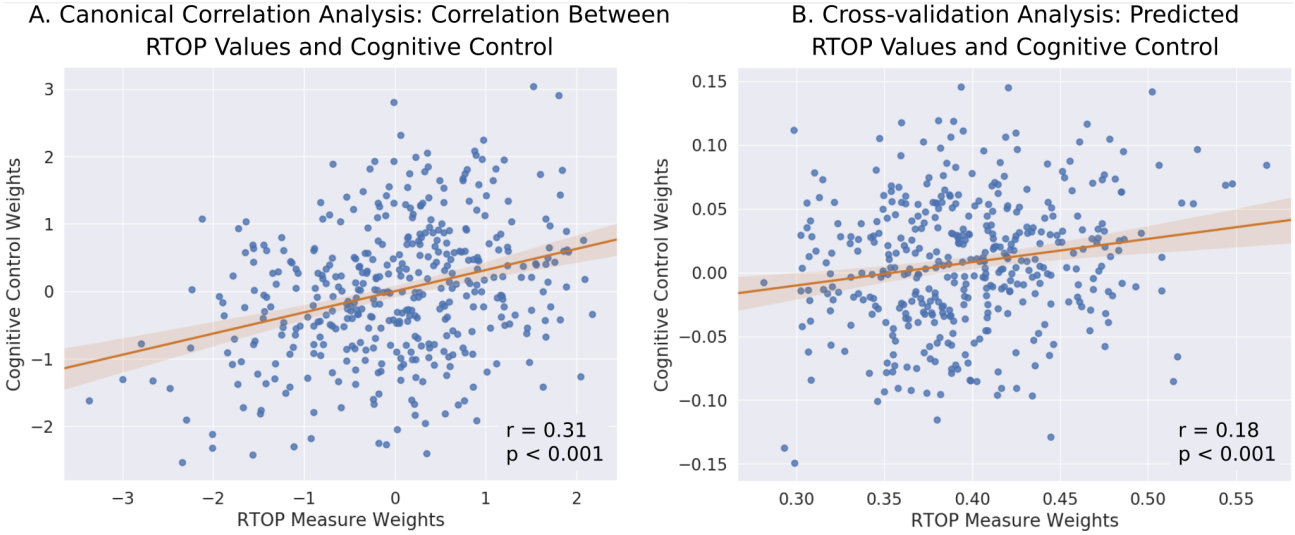

Figure 4.2: Insula microstructural features predict cognitive control abilities. (A) canonical correlation analysis (CCA) revealed a relationship between RTOP and cognitive control measures. CCA weights of RTOP measures in Axis 1 has significant correlation with CCA weights of cognitive measures in CCA Axis 1. (B) Cross-validation analysis revealed that predicted CCA weights of RTOP and cognitive measures on unseen data are significantly correlated.

Behavioral measures consisted of a set of carefully chosen in- and out-scanner variables that are highly relevant to cognitive control capacity. In-scanner behavioral task measures included n-back working memory task accuracy and reaction time (RT), relational task accuracy and RT, and gambling task percentage accuracy and RT for larger choice. Out-of-scanner behavioral measures consisted of performance on List sorting, Flanker, Card sorting, Picture sequence tasks from the NIH toolbox as well as the processing speed. Together, there were 11 behavioral measures. CCA is a statistical method for examining the relationship between two multivariate sets of variables). Specifically, CCA finds the optimal linear combination of two sets of variables that maximize the relation between them. Prediction analysis was performed using leave-one-out cross-validation. In each iteration, brain and behavioral data from one participant was selected as a test set and the remaining data were used as a training set. CCA analysis was used to find the optimal combination weights of the brain and behavioral measures. The weights were then applied to the test data to obtain predicted values for brain and behavioral measures in CCA space. This procedure was repeated with each participant used once as a test set. Pearson's correlation was used to compute correlation between the predict brain and behavioral measures.

Mean normalized RTOP values from the six insular subdivisions proposed by Deen et al. (2011, shown in Figure 4.1B), 3 in each hemisphere, were used to predict cognitive-behavioral measures associated with processing speed, working memory, response inhibition and cognitive flexibility. We found a significant relation between insular normalized RTOP values and individuals cognitive control abilities (Pillai's trace=0.21, p<0.01). The canonical weights of the 1st latent variable in microstructural

measures were significantly correlated with the canonical weights of the 1st latent variable in behavioral measures (r=0.31, p<0.001, Figure 4.2a). A leave-one-out cross-validation procedure further revealed that, based on microstructural properties of the insula, our CCA model could predict cognitive control ability on unseen data (r=0.18, p<0.001, Figure 4.2b).

These results provide novel strong support for an association between the microstructural properties of the insula and individual differences in cognitive control ability. Remarkably, machine learning algorithms and cross-validation on the large HCP samples revealed that cognitive control abilities could be predicted in a left-out sample with the strongest predictive weights in the right anterior insula. Our findings provide novel in vivo evidence that the microstructural integrity of the insula is crucial for implementing cognitive control. Gray matter lesions and insults to white matter pathways associated with the insular cortex and pathways linking it to the salience network have also been shown to impair cognitive control ability (Clark et al., 2008; Gläscher et al., 2012; Jilka et al., 2014). In particular, the anterior insula, the key node in the salience network, is the most consistently and highly activated brain region during tasks involving cognitive control (Swick et al., 2011; Cai et al., 2014). The strength of effective connectivity between anterior insula and other regions in the core cognitive control networks is modulated by cognitive demands (e.g. Cai et al., 2016). Aberrant connectivity of the anterior insula has been associated with cognitive deficits in psychiatric disorders (Palaniyappan et al., 2013; Cai et al., 2018; Taghia et al., 2018). Integrating these and other related findings, a prominent neurocognitive model has proposed that the salience network, especially the anterior insula, plays an important role in dynamically switching between other core brain networks to facilitate access to cognitive resources (Menon et al., 2010). A unique feature of the human insular cortex that is thought support its role in fast switching is the presence of VENs, whose large axons could be fundamental neuronal basis for rapid signal relay between the anterior insula and anterior cingulate cortex as well as other brain networks. Our findings provide convergent support for this hypothesis and demonstrate a link between the unique microstructural features of the anterior insula and cognitive control function in humans, and they provide new quantitative metrics for investigating multiple psychiatric and neurological disorders known to impact the insula transdiagnostically (Goodkind et al., 2015).

4.2 Genetic load determines atrophy in hand cortico-striatal pathways in presymptomatic Huntington's disease

Huntington's disease is a genetic brain disorder that causes physical and mental decline, including uncontrollable movements, emotional problems, and loss of thinking abilities. Huntington's disease is caused by expansion of cytosine-adenine-guanine (CAG) repeats in the Huntington (HTT) gene, with a threshold of 36 or more repeats (Vonsattel et al., 1998). During the presymptomatic (i.e. prodromal-HD) phase, individuals do not manifest the characteristic motor symptoms necessary for a diagnosis, but they have been shown to exhibit mild subclinical cognitive, psychiatric and motor deficits. Symptoms of HD vary between individuals and its progression may evolve over years before formal

diagnosis. Studies show that brain atrophy occurs gradually and typically starts years before symptom onset. Although this inherited disease currently has no cure, identification of reliable markers might be useful for future Huntington's disease clinical trials to monitor disease progression and evaluate therapeutic efficacy (Ross et al., 2014).

HD causes progressive breakdown of striatal neurons. Standard white matter integrity measures like fractional anisotropy and mean diffusivity derived from DTI were analyzed in prodromal-HD subjects. However, they studied either a whole brain or specific subcortical white matter structures with connections to cortical motor areas. In this work (Hong et al., 2018), we propose a novel analysis of a longitudinal cohort of 243 prodromal-HD individuals and 88 healthy controls who underwent two or more diffusion MRI scans as part of the PREDICT-HD study. Using WMQL we separately traced specific white matter fiber tracts connecting the striatum (caudate and putamen) with four cortical regions corresponding to the hand, face, trunk, and leg motor areas. A multi-tensor tractography algorithm with an isotropic volume fraction compartment (Malcolm et al., 2010) allows estimating diffusion of fast-moving extra-cellular water in regions containing crossing fibers and provides quantification of a microstructural property related to tissue atrophy. We analyzed tissue atrophy rate separately in eight cortico-striatal pathways as a function of CAG-repeats (genetic load) by statistically regressing out age effect from our cohort. The results demonstrate a statistically significant increase in isotropic volume fraction (atrophy) bilaterally in hand fiber connections to the putamen with increasing CAG-repeats. This connects the genetic abnormality, i.e. CAG-repeats, to an imaging-based microstructural marker of tissue integrity in specific white matter pathways in HD. We also found that isotropic volume fraction measures in eight cortico-striatal pathways are also correlated significantly with total motor scores and diagnostic confidence levels, providing evidence of their relevance to HD clinical presentation.

4.2.1 Results and Discussion

In this work, we analyzed the longitudinal diffusion MRI data set of prodromal-HD subjects acquired as part of the PREDICT-HD project (Paulsen et al., 2014). We manually created a modification of the Desikan-Killiany cortical atlas (Desikan et al., 2006) to produce a new atlas that includes delineations of the hand, face, trunk, and leg sub-regions of the motor cortex. These new expert-defined atlas regions were spatially mapped to the T1-weighted image of each individual subject. Whole brain multi-tensor tractography was performed on the dMRI data and white matter tracts connecting the striatum (caudate and putamen) with each of the four cortical motor regions were extracted by adapting the CST query of WMQL (see Section 3.3), as shown in Figure 4.3. The isotropic volume fraction was estimated in each of the fiber bundles (a total of sixteen fiber bundles; four cortico-caudal and four cortico-putamen in each hemisphere) and mixed-effects models (Lindstrom et al., 1988) were used to analyze the data as described in Hong et al. (2018, Section 2.1).

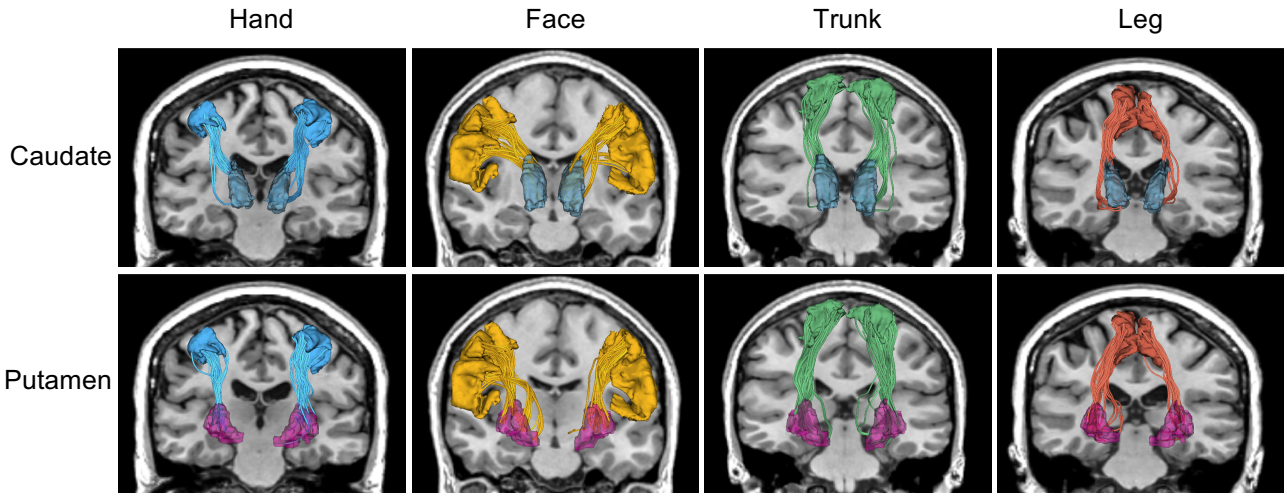

Figure 4.3: White matter tracts connecting the striatum extracted by means of WMQL (top: caudate and bottom: putamen) with four cortical motor regions (left to right: hand, face, trunk, and leg).

Differential rate of increase in the isotropic volume fraction with age

In Hong et al. (2018) we first show that isotropic volume fraction changes over age for different sensorimotor areas. Then, we investigate which region shows a faster rate of increase in the isotropic volume fraction (or atrophy). We estimated group trends of the tract-averaged isotropic water fraction in different regions for both normal control and prodromal-HD subjects. In particular, we compared the isotropic volume fraction difference between these two groups at age 50 (years), as the fit from linear regression has the lowest uncertainty at this age. Specifically, we estimated the isotropic volume fraction at age 50 for both groups and then computed their difference. To ensure robustness of the results, we color coded the rates such that the blue bars indicate connections for which the slope was statistically significant (after FDR correction). As shown in Figure 4.4 (top row), at the age of 50 years, the average isotropic volume fraction in the prodromal-HD group is larger than that for the normal control group in almost all cortico-striatal pathways. The top two significant fiber connections on the list are hand to the bilateral putamen, as shown on the top right of Figure 4.4. In addition, the rate of increase in the isotropic volume fraction in prodromal-HD subjects is also faster than controls in almost all pathways. By discarding estimates with adjusted p-value larger than 0.05 (the gray bars in Figure 4.4), the fiber bundles connecting hand and leg to right putamen show the fastest increase in the isotropic volume fraction (i.e., fastest rate of atrophy). The fiber bundle connecting hand to left putamen also shows similar rate of atrophy. Thus, after accounting for the normal degeneration rate (from healthy controls), the cortico-striatal hand motor fibers seem to degenerate faster than other fiber tracts in HD.

4.2.2 Isotropic volume fraction correlation with genetic load

The number of CAG repeats determines whether a subject will develop HD during his or her lifetime. We aim to find the correlation between this genetic load and isotropic volume fraction in the prodromal-

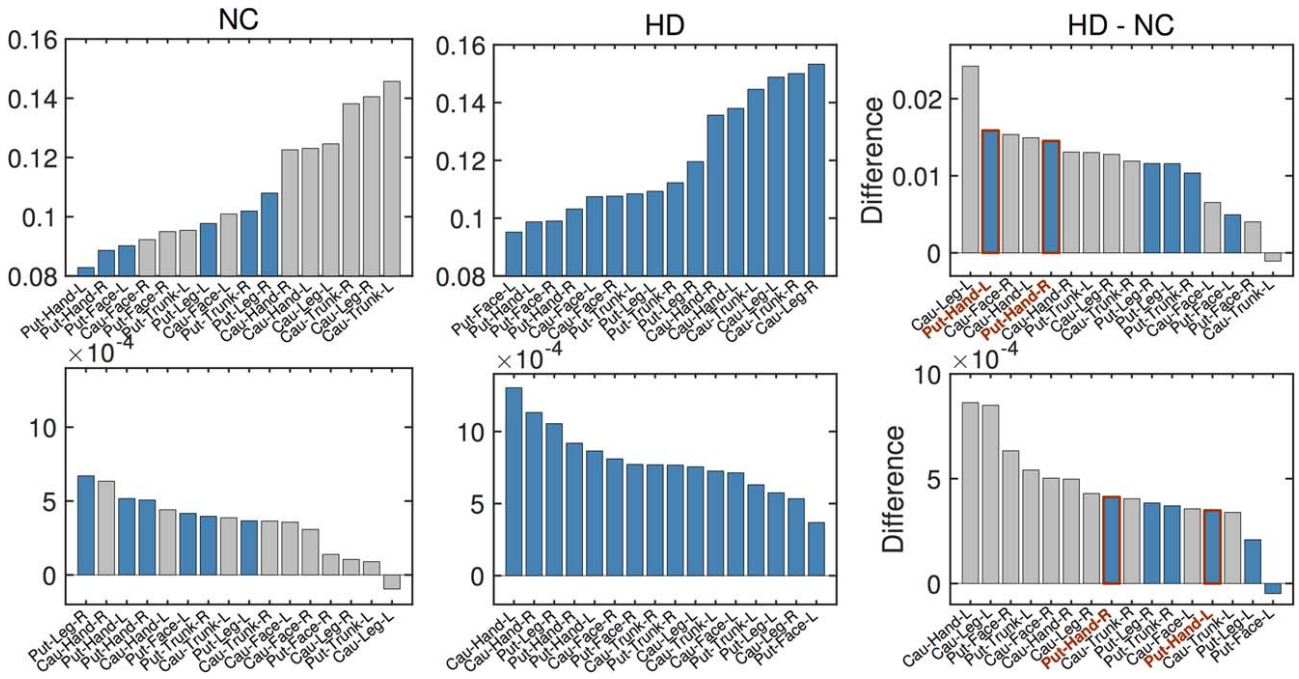

Figure 4.4: Comparison of the isotropic volume fraction between Normal Control (NC) and prodromal-HD groups. Top: the averaged isotropic volume fraction values estimated at the age of 50 years old for different regions. Bottom: the degeneration rates (slopes of estimated group trends) for different regions. From left to right: NC group, HD group, and their differences. Gray bars were used in those regions where estimate for the slope is not significant at the level of 0.05 (i.e., no significant correlation between isotropic volume fraction and age), while blue bars indicate that the results are significant at the level of 0.05. (Cau: Caudate, Put: Putamen).

HD group. To achieve this goal, we first regress out the effects of normal aging on changes in the isotropic volume fraction, and then estimate the relationship between the isotropic volume residuals and CAG repeats in prodromal-HD subjects. Although no significant correlations are found in caudal connections, motor regions connected to the putamen show significant correlations, for example, hand to the left and right putamen and leg to the right putamen, as shown in Figure 4.5 (Hong et al., 2018, see Supplementary material, Table 3 for the statistics). In addition, face to the left putamen and trunk to the right putamen (in Figure 4.5) also show a significant change in the slope, indicating strong correlation between the isotropic volume fraction and CAG repeats in these regions. These results indicate that the isotropic volume fraction correlates with the genetic load in prodromal-HD subjects, and it further confirms that the putamen (and its motor connections) could play a critical role in early assessment of degeneration in HD.

4.2.3 Isotropic volume fraction correlates with clinical scores

To further explore the relationship of the isotropic volume fraction with clinical scores, we used total motor scores and diagnostic confidence levels of prodromal-HD subjects using linear mixed-effects models. These scores are used to define motor diagnosis in at-risk individuals, and we study them only in prodromal-HD subjects. In addition, for each motor area we average the isotropic volume

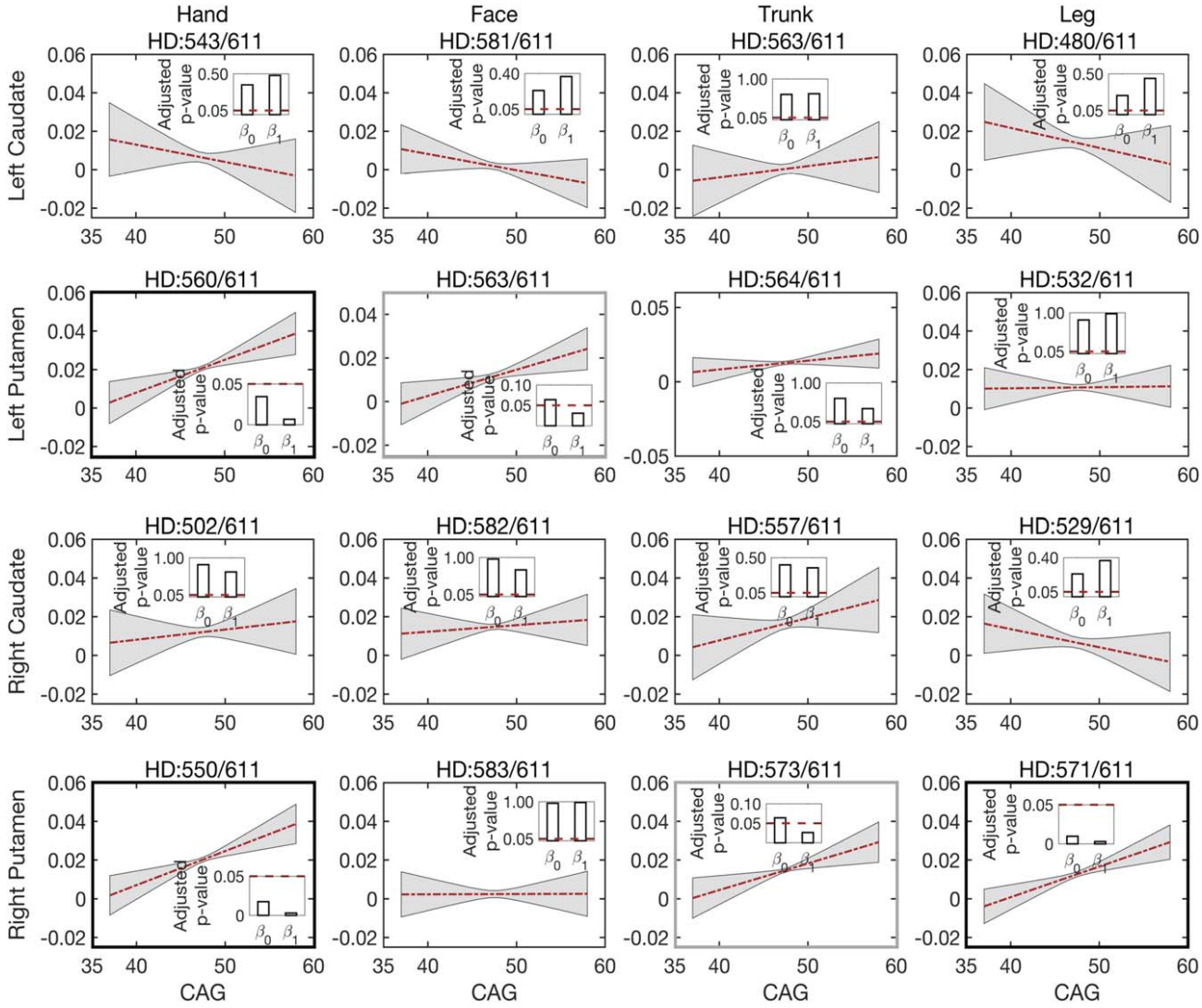

Figure 4.5: Correlations between the isotropic volume fraction residuals (after regressing out the effect of age) and CAG repeats in prodromal-HD group for white matter connections to left caudate, left putamen, right caudate, and right putamen (from top to bottom). Lines depict estimates of group trends, gray areas indicate their 95% confidence intervals, and bars indicate the corresponding p-values of the estimated intercepts (β_0) and slopes (β_1). The title of each sub-figure details tractography connections and the number of scans for which robust connections were obtained out of total scans in prodromal-HD group.

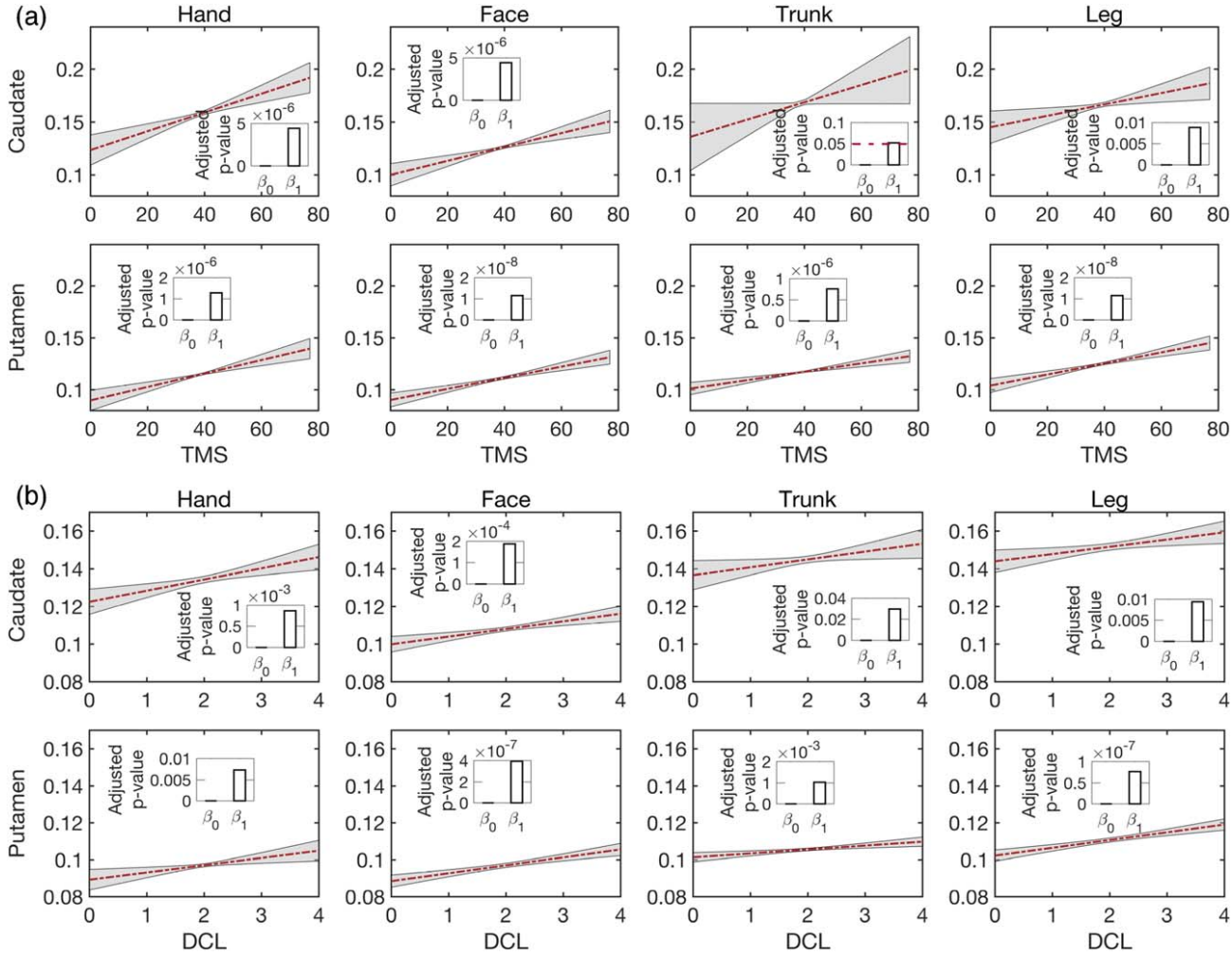

Figure 4.6: Correlations between the isotropic volume fraction and (a) total motor scores (TMS), (b) diagnostic confidence level (DCL) in prodromal-HD group for caudate (top) and putamen (bottom). Lines show estimates of group trends, gray areas indicate their 95% confidence intervals, and bars present the corresponding FDR-corrected p-values of the estimated intercepts (β_0) and slopes (β_1).

fraction from the bilateral tracts of the caudate or the putamen. The experimental results are shown in Figure 4.6. In all regions except for trunk to the caudate for testing total motor scores correlation, the isotropic volume fraction was significantly correlated with both total motor scores and diagnostic confidence level with $p < 0.05$ (Hong et al., 2018, see FDR corrected p-values in Supplementary material, Table 4).

CHAPTER 5

CONCLUSIONS

In this dissertation I presented different contributions towards improving our understanding of the relationship between the human brain's tissue and architecture, and cognition and neurological disease. Two methodological contributions towards enhancing the quality of microstructural analysis and reducing the data acquisition requirements were presented in Chapter 2. Two methodological contributions towards dividing the brain into large discrete sections to ease the conceptualisation and analysis of brain function and neurology were presented in Chapter 3. Finally, two applications were presented in Chapter 4: one linking cytoarchitecture to cognition; one linking macrostructure to diagnosis and motor function decay.

There is, however, something that this research has brought into light. The lack of a common framework to express and perform, document, and reproduce neuroanatomy, and probably neuroscience, experiments. Neuroscience is at an inflection point. The 150 year-old cortical specialization paradigm, in which cortical brain areas have a distinct set of functions, is experiencing an unprecedented momentum with over 1000 articles being published each year. However, this paradigm is reaching its limit. Recent studies show that current approaches to atlas brain areas, like relative location, cellular population type, or connectivity, are not enough on their own to characterize a cortical area and its function unequivocally (Zilles et al., 2013; Ding et al., 2016; Glasser et al., 2016). Moreover, cortical functions are prone to changing size and location on the cortex due to plasticity processes (Duffau, 2015). Consequently, it is difficult to translate the cortical specialization map from one individual to another, hindering the reproducibility and advancement of neuroscience. The field is in *dire need of a universal standard to specify cortical regions and their connectivity*: a novel formal language allowing neuroscientists to simultaneously specify tissue characteristics, relative location, known function, and connectional topology for the unequivocal identification of a given cortical region. Neuroscience needs

a domain specific language.

From this work, I draw the conclusion that a *unified formal language for neuroanatomy*, much as WMQL presented in Section 3.3, will boost our understanding of the brain. By defining brain regions, networks, and cognitive tasks through a set of formal criteria, i.e. equations, expressed in a syntax resembling standard neuroanatomical and cognitive vocabulary, researchers will be able *to query, synthesize and integrate data within and across diverse studies*. In doing so, a neuroanatomical DSL will accelerate the development of neuroscience by providing a way to evaluate anatomical specificity, test current theories and develop new hypotheses.

The *large nomenclature inconsistency* in cognitive sciences and neuroanatomy has long hampered the development of the neurosciences (Poldrack et al., 2016; Tremblay et al., 2016; Wassermann et al., 2016). Recent ontology-based approaches proposed to address this issue can be seen as the embryo of a formal language for neuroanatomy. Ontologies provide 3 major advantages (Poldrack et al., 2016): a controlled vocabulary; a framework for annotating data such as cortical areas involved in a cognitive task; and a tool to infer relations between concepts which are absent in the initial dataset. Despite being able to identify brain areas based on cognitive involvement (Yarkoni et al., 2011), ontology-based approaches can't perform inference based on continuous characteristics of brain tissue such as cell density or functional response (Glasser et al., 2016). This limits their ability to solve a fundamental problem in current neurosciences: *relating specific neurobiological traits to cognitive tasks*.

Alternative approaches study the relationship between cognition and neurobiology through brain parcellations on the grey and white matter. These are based on multiple neurobiological traits such as architecture, function, connectivity or topography (Zilles et al., 2013; Glasser et al., 2016). These techniques are able to synthesize continuous information on brain tissue and relate it to cognitive tasks (Glasser et al., 2016). However, *these approaches are hampered by important sources of brain variability*: individual brains are known to have atypical topological arrangements challenging the cross-subject spatial matching hypotheses underlying these approaches; moreover, even if an optimal spatial mapping across brain tissue and topology exists, functional localization is prone to be situated in different areas across individuals (Ding et al., 2016; Tremblay et al., 2016) and can change size and location through plasticity (Duffau, 2015). In short, individual variability is not noise (Zilles et al., 2013).

To summarize, both brain tissue parcellation methods and ontology-based approaches have important limitations when it comes to handle the complexity of the human brain. Evidence across the board points to the need for a novel methodology to define neuroanatomical and cognitive taxonomies. A methodology allowing these taxonomies to be *defined unequivocally across studies*, and *able to capture individual and population variability beyond the limitations of spatial matching*.

The unprecedented availability of large population multimodal imaging (Glasser et al., 2016), ultra-high resolution histology (Amunts et al., 2013; Ding et al., 2016), and controlled representations of

cognitive tasks (Poldrack et al., 2016) provides a unique opportunity to gain insight into the organisation of the brain. There is a need to capitalize on these resources, provided by project such as HCP and Human Brain Project, to address the lack of a unified formal language for neuroscience by building a computational model of multimodal brain analysis, a *Domain Specific Language for neuroanatomy*.

Bibliography

Aggarwal, M., M. V. Jones, P. A. Calabresi, S. Mori, and J. Zhang (2012). "Probing Mouse Brain Microstructure Using Oscillating Gradient Diffusion MRI". In: *Magnetic Resonance in Medicine* 67.1, pp. 98–109. ISSN: 07403194. DOI: 10.1002/mrm.22981.

Akers, D., A. Sherbondy, R. Mackenzie, R. F. Dougherty, and B. Wandell (2004). "Exploration of the Brain's White Matter Pathways with Dynamic Queries". In: *IEEE Viz*. IEEE Visualization 2004. IEEE Comput. Soc, pp. 377–384. ISBN: 0-7803-8788-0. DOI: 10.1109/VISUAL.2004.30.

Alexander, D. C. (2008). "A General Framework for Experiment Design in Diffusion MRI and Its Application in Measuring Direct Tissue-Microstructure Features". In: 60.2, pp. 439–448. DOI: 10.1002/mrm.21646.

Alexander, D. C., P. L. Hubbard, M. G. Hall, E. A. Moore, M. Ptito, G. J. M. Parker, and T. B. Dyrby (2010). "Orientationally Invariant Indices of Axon Diameter and Density from Diffusion MRI". In: 52, pp. 1374–1389. DOI: DOI:10.1016/j.neuroimage.2010.05.043.

Allman, J. M., N. A. Tetreault, A. Y. Hakeem, K. F. Manaye, K. Semendeferi, J. M. Erwin, S. Park, V. Goubert, and P. R. Hof (2010). "The von Economo Neurons in Frontoinsular and Anterior Cingulate Cortex in Great Apes and Humans." In: *Brain Struct Funct* 214, pp. 495–517. DOI: 10.1007/s00429-010-0254-0.

Amunts, K., C. Lepage, L. Borgeat, h. Mohlberg, T. Dickscheid, M.-É. Rousseau, S. Bludau, P.-L. L. Bazin, L. B. Lewis, A.-M. Oros-Peusquens, N. J. Shah, T. Lippert, K. Zilles, and A. C. Evans (2013). "BigBrain: An Ultrahigh-Resolution 3D Human Brain Model." In: *Science* 340.6139, pp. 1472–1475. DOI: 10.1126/science.1235381.

Amunts, K. and K. Zilles (2015). "Architectonic Mapping of the Human Brain beyond Brodmann". In: *Neuron* 88.6, pp. 1086–1107. DOI: 10.1016/j.neuron.2015.12.001.

Anderson, P. W. (1972). "More Is Different". In: *Science* 177.4047, pp. 393–396. ISSN: 0036-8075, 1095-9203. DOI: 10.1126/science.177.4047.393.

Anwander, A., M. Tittgemeyer, D. von Cramon, A. Friederici, and T. R. Knösche (2007). "Connectivity-Based Parcellation of Broca's Area". In: *Cerebral Cortex* 17, pp. 16–825. DOI: 10.1093/cercor/bhk034.

Assaf, Y., D. Ben-Bashat, J. Chapman, S. Peled, I. E. Biton, M. Kafri, Y. Segev, T. Hendler, A. D. Korczyn, M. Graif, and Y. Cohen (2002). "High B-Value q-Space Analyzed Diffusion-Weighted MRI: Application to Multiple Sclerosis". In: *Magnetic Resonance in Medicine* 47.1, pp. 115–126. ISSN: 1522-2594. DOI: 10.1002/mrm.10040.

Assaf, Y., T. Blumenfeld Katzir, Y. Yovel, and P. J. Basser (2008). "Axcaliber: A Method for Measuring Axon Diameter Distribution from Diffusion MRI". In: *Magnetic Resonance in Medicine* 59.6, pp. 1347–1354. DOI: 10.1002/mrm.21577.

Avants, B., P. T. Schoenemann, and J. C. Gee (2006). "Lagrangian Frame Diffeomorphic Image Registration: Morphometric Comparison of Human and Chimpanzee Cortex". In: *MIA* 10, pp. 397–412. DOI: 10.1016/j.media.2005.03.005.

Avants, B., N. J. Tustison, G. Song, P. A. Cook, A. Klein, and J. C. Gee (2011). "A Reproducible Evaluation of ANTs Similarity Metric Performance in Brain Image Registration". In: 54.3, pp. 2033–2044. DOI: 10.1016/j.neuroimage.2010.09.025.

Avram, A. V., J. E. Sarlls, A. S. Barnett, E. Özarslan, C. Thomas, M. O. Irfanoglu, E. Hutchinson, C. Pierpaoli, and P. J. Basser (2016). "Clinical Feasibility of Using Mean Apparent Propagator (MAP) MRI to Characterize Brain Tissue Microstructure". In: *NeuroImage* 127, pp. 422–434. ISSN: 10538119. DOI: 10.1016/j.neuroimage.2015.11.027.

Avram, L., E. Özarslan, Y. Assaf, A. Bar-Shir, Y. Cohen, and P. J. Basser (2008). "Three-Dimensional Water Diffusion in Impermeable Cylindrical Tubes: Theory versus Experiments." In: *NMR in Biomedicine* 21.8, pp. 888–898. DOI: 10.1002/nbm.1277.

Axer, H., C. M. Klingner, and A. Prescher (2012). "Fiber Anatomy of Dorsal and Ventral Language Streams". In: DOI: 10.1016/j.bandl.2012.04.015.

Balinov, B., B. Jonsson, P. Linse, and O. Soderman (1993). "The NMR Self-Diffusion Method Applied to Restricted Diffusion. Simulation of Echo Attenuation from Molecules in Spheres and between Planes". In: 104.1, pp. 17–25. DOI: 10.1006/jmra.1993.1184.

Basser, P. J., J. Mattiello, and D. Le Bihan (1994). "MR Diffusion Tensor Spectroscopy and Imaging". In: *Biophysical Journal* 66.1, pp. 259–267.

Basser, P. J., S. Pajevic, C. Pierpaoli, J. Duda, and A. Aldroubi (2000). "In Vivo Fiber Tractography Using DT-MRI Data". In: 44.4, pp. 625–632.

Basser, P. J. and C. Pierpaoli (1996). "Microstructural and Physiological Features of Tissues Elucidated by Quantitative-Diffusion-Tensor MRI". In: 111.3, pp. 209–219.

Beaulieu, C. (2002). "The Basis of Anisotropic Water Diffusion in the Nervous System - a Technical Review". In: 15, pp. 435–455. DOI: 10.1002/nbm.782.

Behrens, T. E. J., H. Johansen-Berg, M. W. Woolrich, S. M. Smith, C. A. M. Wheeler-Kingshott, P. A. Boulby, G. J. Barker, E. L. Sillery, K. Sheehan, O. Ciccarelli, A. J. Thompson, J. M. Brady, and P. M. Matthews (2003a). "Non-Invasive Mapping of Connections between Human Thalamus and Cortex Using Diffusion Imaging". In: *Nature Neuroscience* 6.7, pp. 750–757. ISSN: 1097-6256, 1546-1726. DOI: 10.1038/nn1075.

Behrens, T. E. J., M. W. Woolrich, M. Jenkinson, H. Johansen-Berg, R. G. Nunes, S. Clare, P. M. Matthews, J. M. Brady, and S. M. Smith (2003b). "Characterization and Propagation of Uncertainty in Diffusion-Weighted MR Imaging". In: *Magnetic Resonance in Medicine* 50.5, pp. 1077–1088. ISSN: 1522-2594. DOI: 10.1002/mrm.10609.

Behrens, T. E. J. and O. Sporns (2012). "Human Connectomics". In: *Current Opinion in Neurobiology* 22.1, pp. 144–153. DOI: 10.1016/j.conb.2011.08.005.

Bertalanffy, L. v. (.-1. (1928). *Kritische Theorie Der Formbildung*. Gebrüder Borntraeger. Berlin.

Beyer, K., J. Goldstein, R. Ramakrishnan, and U. Shaft (1999). "When is "nearest neighbor" meaningful?" In: *Database Theory—ICDT'99*, pp. 217–235. ISSN: 3540654526. DOI: 10.1007/3-540-49257-7_15.

Boltzmann, L. (1867). *Über Die Anzahl Der Atome in Den Gasmolecülen Und Die Innere Arbeit in Gasen*. Kk Hof-und Staatsdruckerei.

Breasted, J. H. (1930). *The Edwin Smith Surgical Papyrus*. University of Chicago Press.

Broca, P. (1861). "Remarques Sur Le Siege de La Faculté Du Langage Articulé, Suivies d'une Observation d'aphemie (Perte de La Parole)". In: *Bulletin de la Société Anatomique* 6, pp. 330–357.

Brodmann, K. (1909). *Vergleichende Lokalisationslehre Der Grosshirnrinde in Ihren Prinzipien Dargestellt Auf Grund Des Zellenbaues*. Springer. 335 pp.

Bullmore, E. T. and O. Sporns (2009). "Complex Brain Networks: Graph Theoretical Analysis of Structural and Functional Systems". In: *Nature Reviews Neuroscience* 10.3, pp. 186–198. DOI: 10.1038/nrn2575.

Burcaw, L. M., E. Fieremans, and D. S. Novikov (2015). "Mesoscopic Structure of Neuronal Tracts from Time-Dependent Diffusion". In: 114, pp. 18–37. DOI: 10.1016/j.neuroimage.2015.03.061.

Cai, W., T. Chen, S. Ryali, J. Kochalka, C.-S. R. Li, and V. Menon (2016). "Causal Interactions Within a Frontal-Cingulate-Parietal Network During Cognitive Control: Convergent Evidence from a Multisite-Multitask Investigation". In: *Cereb. Cortex* 26.5, pp. 2140–2153. ISSN: 1460-2199. DOI: 10.1093/cercor/bhv046. pmid: 25778346.

Cai, W., T. Chen, L. Szegletes, K. Supekar, and V. Menon (2018). "Aberrant Time-Varying Cross-Network Interactions in Children With Attention-Deficit/Hyperactivity Disorder and the Relation to Attention Deficits". In: *Biol Psychiatry Cogn Neurosci Neuroimaging* 3.3, pp. 263–273. ISSN: 2451-9030. DOI: 10.1016/j.bpsc.2017.10.005. pmid: 29486868.

Cai, W., S. Ryali, T. Chen, C.-S. R. Li, and V. Menon (2014). "Dissociable Roles of Right Inferior Frontal Cortex and Anterior Insula in Inhibitory Control: Evidence from Intrinsic and Task-Related Functional Parcellation, Connectivity, and Response Profile Analyses across Multiple Datasets". In: *J. Neurosci.* 34.44, pp. 14652–14667. ISSN: 1529-2401. DOI: 10.1523/JNEUROSCI.3048-14.2014. pmid: 25355218.

Callaghan, P. T. (1995). "Pulsed-Gradient Spin-Echo NMR for Planar, Cylindrical, and Spherical Pores under Conditions of Wall Relaxation". In: *JMR* 113.1, pp. 53–59. DOI: 10.1006/jmra.1995.1055.

Callaghan, P. T., D. MacGowan, K. J. Packer, and F. O. Zelaya (1990). "High-Resolution q-Space Imaging in Porous Structures". In: *J Magn Reson* 90, pp. 177–182. DOI: 10.1016/0022-2364(90)90376-K.

Callaghan, P. T., C. Eccles, and Y. Xia (1988). "NMR Microscopy of Dynamic Displacements: K-Space and q-Space Imaging". In: *Journal of Physics E: Scientific Instruments* 21, pp. 820–822.

Caminiti, R., F. Carducci, C. Piervincenzi, A. Battaglia-Mayer, G. Confalone, F. Visco-Comandini, P. Pantano, and G. M. Innocenti (2013). "Diameter, Length, Speed, and Conduction Delay of Callosal Axons in Macaque Monkeys and Humans: Comparing Data from Histology and Magnetic Resonance Imaging Diffusion Tractography." In: *Journal of Neuroscience* 33.36, pp. 14501–14511. DOI: 10.1523/JNEUROSCI.0761-13.2013.

Carr, H. Y. and E. Purcell (1954). "Effects of Diffusion on Free Precession in Nuclear Magnetic Resonance Experiments". In: *Physical Review* 94.3, pp. 630–638.

Caruyer, E., C. Lenglet, G. Sapiro, and R. Deriche (2013). "Design of Multishell Sampling Schemes with Uniform Coverage in Diffusion MRI". In: 69.6, pp. 1534-1540-1540. DOI: 10.1002/mrm.24736.

Catani, M., M. Allin, M. Husain, L. Pugliese, M. Mesulam, R. Murray, and D. K. Jones (2007). "Symmetries in Human Brain Language Pathways Correlate with Verbal Recall". In: 104.43, p. 17163.

Catani, M., D. K. Jones, and D. H. Ffytche (2005). "Perisylvian Language Networks of the Human Brain." In: 57.1, pp. 8–17.

Catani, M. and M. Thiebaut de Schotten (2008). "A Diffusion Tensor Imaging Tractography Atlas for Virtual in Vivo Dissections." In: *Cortex* 44.8, pp. 1105–1132. DOI: 10.1016/j.cortex.2008.05.004.

Catani, M., M. Thiebaut de Schotten, D. Slater, and F. Dell'acqua (2013). "Connectomic Approaches before the Connectome". In: *NImg* 80, pp. 2–13. DOI: 10.1016/j.neuroimage.2013.05.109.

Clark, L., A. Bechara, H. Damasio, M. R. F. Aitken, B. J. Sahakian, and T. W. Robbins (2008). "Differential Effects of Insular and Ventromedial Prefrontal Cortex Lesions on Risky Decision-Making". In: *Brain* 131.5, pp. 1311–1322. ISSN: 0006-8950. DOI: 10.1093/brain/awn066.

Clarkson, M. J., I. B. Malone, M. Modat, K. K. Leung, N. Ryan, D. C. Alexander, N. C. Fox, and S. Ourselin (2010). *A Framework For Using Diffusion Weighted Imaging To Improve Cortical Parcellation*. Ed. by T. Jiang, N. Navab, J. P. W. Pluim, and M. A. Viergever. Vol. 6362. Lecture Notes in Computer Science PART 2. Berlin, Heidelberg: Springer Berlin Heidelberg, pp. 169–176. ISBN: 978-3-642-15744-8. DOI: 10.1007/978-3-642-15745-5.

Cohen, J. (1960). "A Coefficient of Agreement for Nominal Scales". In: *Educational and Psychological Measurement* 20.1, pp. 37–46. DOI: 10.1177/001316446002000104.

Cohen, Y. and Y. Assaf (2002). "High B-Value q-Space Analyzed Diffusion-Weighted MRS and MRI in Neuronal Tissues - a Technical Review." In: *NMR in Biomedicine* 15.7-8, pp. 516–542. DOI: 10.1002/nbm.778.

Commowick, O., A. Maarouf, J.-C. Ferré, J.-P. Ranjeva, G. Edan, and C. Barillot (2015). "Diffusion MRI Abnormalities Detection with Orientation Distribution Functions: A Multiple Sclerosis Longitudinal Study". In: *Medical Image Analysis* 22.1, pp. 114–123. ISSN: 1361-8415. DOI: 10.1016/j.media.2015.02.005.

Conturo, T., N. Lori, T. Cull, E. Akbudak, A. Snyder, J. Shimony, R. McKinstry, H. Burton, and M. Raichle (1999). "Tracking Neuronal Fiber Pathways in the Living Human Brain". In: 96.18, pp. 10422–10427.

Cory, D. G. (1990). “Measurement of Translational Displacement Probabilities by NMR: An Indicator of Compartmentation”. In: 14.3, pp. 435–444. DOI: 10.1002/mrm.1910140303.

Craig, A. D. B. (2009). “How Do You Feel–Now? The Anterior Insula and Human Awareness”. In: *Nat. Rev. Neurosci.* 10.1, pp. 59–70. ISSN: 1471-0048. DOI: 10.1038/nrn2555. pmid: 19096369.

De Backer, P., D. De Waele, and L. Van Speybroeck (2010). “Ins and Outs of Systems Biology Vis-à-Vis Molecular Biology: Continuation or Clear Cut?” In: *Acta Biotheor* 58.1, pp. 15–49. ISSN: 1572-8358. DOI: 10.1007/s10441-009-9089-6.

De Santis, S., D. K. Jones, and A. Roebroeck (2016). “Including Diffusion Time Dependence in the Extra-Axonal Space Improves in Vivo Estimates of Axonal Diameter and Density in Human White Matter”. In: 130, pp. 91–103. DOI: 10.1016/j.neuroimage.2016.01.047.

Deen, B., N. B. Pitskel, and K. A. Pelphrey (2011). “Three Systems of Insular Functional Connectivity Identified with Cluster Analysis”. In: *Cereb. Cortex* 21.7, pp. 1498–1506. ISSN: 1460-2199. DOI: 10.1093/cercor/bhq186. pmid: 21097516.

Dejerine, J. and A. Dejerine-Klumpke (1895). *Anatomie Des Centres Nerveux*. Rueff Paris.

Descoteaux, M., E. Angelino, S. Fitzgibbons, and R. Deriche (2007). “Regularized, Fast and Robust Analytical Q-Ball Imaging”. In: 58.3, pp. 497–510.

Desikan, R. S., F. Ségonne, B. Fischl, B. T. Quinn, B. C. Dickerson, D. Blacker, R. L. Buckner, A. M. Dale, R. P. Maguire, B. T. Hyman, M. Albert, and R. J. Killiany (2006). “An Automated Labeling System for Subdividing the Human Cerebral Cortex on MRI Scans into Gyral Based Regions of Interest.” In: *NImg* 31.3, pp. 968–980. DOI: 10.1016/j.neuroimage.2006.01.021.

Diamond, S. and S. Boyd (2016). “CVXPY: A Python-Embedded Modeling Language for Convex Optimization”. In: *Journal of Machine Learning Research*. To appear.

Ding, S. L., J. J. Royall, S. M. Sunkin, L. Ng, B. A. C. Facer, P. Lesnar, A. Guillozet Bongaarts, B. McMurray, A. Szafer, T. A. Dolbeare, A. Stevens, L. Tirrell, T. Benner, S. Caldejon, R. A. Dalley, N. Dee, C. Lau, J. Nyhus, M. Reding, Z. L. Riley, D. Sandman, E. Shen, A. Kouwe, A. Varjabedian, M. Write, L. Zollei, C. Dang, J. A. Knowles, C. Koch, J. W. Phillips, N. Sestan, P. Wohnoutka, H. R. Zielke, J. G. Hohmann, A. R. Jones, A. Bernard, M. J. Hawrylycz, P. R. Hof, B. Fischl, and E. S. Lein (2016). “Comprehensive Cellular-resolution Atlas of the Adult Human Brain”. In: *J. Comp. Neurol.* 524.16, pp. 3127–3481. DOI: 10.1002/cne.24080.

Duffau, H. (2015). “Stimulation Mapping of White Matter Tracts to Study Brain Functional Connectivity”. In: *Nat Rev Neurol* 11.5, pp. 255–265. DOI: 10.1038/nrneurol.2015.51.

Evrard, H. C., N. K. Logothetis, and A. Bud Craig (2014). “Modular Architectonic Organization of the Insula in the Macaque Monkey: Architectonic Organization of Macaque Insula”. In: *Journal of Comparative Neurology* 522.1, pp. 64–97. ISSN: 00219967. DOI: 10.1002/cne.23436.

Evrard, H. C., T. Forro, and N. K. Logothetis (2012). “Von Economo Neurons in the Anterior Insula of the Macaque Monkey”. In: *Neuron* 74.3, pp. 482–489.

Felleman, D. J. and D. C. Van Essen (1991). “Distributed Hierarchical Processing in the Primate Cerebral Cortex”. In: *Cereb. Cortex* 1.1, pp. 1–47. ISSN: 1047-3211. pmid: 1822724.

Fernandez-Miranda, J. C., A. L. Rhoton, Y. Kakizawa, C. Choi, and J. Alvarez-Linera (2008). "The Claustrum and Its Projection System in the Human Brain: A Microsurgical and Tractographic Anatomical Study." In: *Journal of Neurosurgery* 108.4, pp. 764–774. DOI: 10.3171/JNS/2008/108/4/0764.

Fick, R. H. J., A. Petiet, M. Santin, A.-C. Philippe, S. Lehericy, R. Deriche, and D. Wassermann (2018a). "Non-Parametric Graphnet-Regularized Representation of dMRI in Space and Time". In: *Medical Image Analysis* 43, pp. 37–53. DOI: 10.1016/j.media.2017.09.002.

Fick, R. H. J., D. Wassermann, E. Caruyer, and R. Deriche (2016a). "MAPL: Tissue Microstructure Estimation Using Laplacian-Regularized MAP-MRI and Its Application to HCP Data". In: *NImg* 134, pp. 365–385. DOI: 10.1016/j.neuroimage.2016.03.046.

Fick, R. H. J., D. Wassermann, M. Pizzolato, and R. Deriche (2015). "A Unifying Framework for Spatial and Temporal Diffusion in Diffusion MRI". In: Information Processing in Medical Imaging.

Fick, R. H. J., M. Pizzolato, D. Wassermann, and R. Deriche (2017). "Diffusion MRI Anisotropy: Modeling, Analysis and Interpretation". In: *Modeling, Analysis, and Visualization of Anisotropy*. Ed. by T. Schultz, E. Özarslan, and I. Hotz. Mathematics and Visualization. Springer International Publishing, pp. 203–228. ISBN: 978-3-319-61358-1.

Fick, R. H., D. Wassermann, E. Caruyer, and R. Deriche (2016b). "MAPL: Tissue microstructure estimation using Laplacian-regularized MAP-MRI and its application to HCP data". In: *NeuroImage* 134, pp. 365–385.

Fick, R., A. Petiet, M. Santin, A.-C. Philippe, S. Lehericy, R. Deriche, and D. Wassermann (2018b). "Non-Parametric Graphnet-Regularized Representation of dMRI in Space and Time". In: *Medical Image Analysis* 43, pp. 37–53. ISSN: 1361-8415. DOI: 10.1016/j.media.2017.09.002.

Filipiak, P., R. Fick, A. Petiet, M. Santin, A.-C. Philippe, S. Lehericy, P. Ciuciu, R. Deriche, and D. Wassermann (2018). "Reducing the Number of Samples in Spatiotemporal dMRI Acquisition Design". In: *Magnetic Resonance in Medicine*. ISSN: 07403194. DOI: 10.1002/mrm.27601.

Fischl, B., D. H. Salat, E. Busa, M. Albert, M. Dieterich, C. Haselgrove, A. van der Kouwe, R. Killiany, D. Kennedy, S. Klaveness, A. Montillo, N. Makris, B. Rosen, and A. M. Dale (2002). "Whole Brain Segmentation: Automated Labeling of Neuroanatomical Structures in the Human Brain". In: 33.3, pp. 341–355. DOI: 10.1016/S0896-6273(02)00569-X.

Frahm, J., K. D. Merboldt, W. Hänicke, and A. Haase (1985). "Stimulated Echo Imaging". In: *Journal of Magnetic Resonance (1969)* 64.1, pp. 81–93.

Gall, F. J. and Spurzheim (1810). *On the Functions of the Brain and of Each of Its Parts*. Marsh, Capen \& Lyon.

Gallardo, G., W. Wells III, R. Deriche, and D. Wassermann (2017). "Groupwise Structural Parcellation of the Whole Cortex: A Logistic Random Effects Model Based Approach". In: *NImg*. DOI: 10.1016/j.neuroimage.2017.01.070.

Garyfallidis, E., M. Brett, B. Amirbekian, A. Rokem, S. Van Der Walt, M. Descoteaux, and I. Nimmo-Smith (2014). "Dipy, a Library for the Analysis of Diffusion MRI Data". In: *Front. Neuroinform.* 8. ISSN: 1662-5196. DOI: 10.3389/fninf.2014.00008.

Ghaziri, J., A. Tucholka, G. Girard, J.-C. Houde, O. Boucher, G. Gilbert, M. Descoteaux, S. Lippé, P. Rainville, and D. K. Nguyen (2017). "The Corticocortical Structural Connectivity of the Human Insula". In: *Cerebral Cortex* 27.2, pp. 1216–1228. DOI: 10.1093/cercor/bhv308.

Gläscher, J., R. Adolphs, H. Damasio, A. Bechara, D. Rudrauf, M. Calamia, L. K. Paul, and D. Tranel (2012). "Lesion Mapping of Cognitive Control and Value-Based Decision Making in the Prefrontal Cortex". In: *PNAS*, p. 201206608. ISSN: 0027-8424, 1091-6490. DOI: 10.1073/pnas.1206608109. pmid: 22908286.

Glasser, M. F., S. N. Sotiropoulos, J. A. Wilson, T. S. Coalson, B. Fischl, J. L. Andersson, J. Xu, S. Jbabdi, M. Webster, J. R. Polimeni, D. C. Van Essen, and M. Jenkinson (2013). "The minimal preprocessing pipelines for the Human Connectome Project". In: *Neuroimage* 80, pp. 105–124. ISSN: 10538119. DOI: 10.1016/j.neuroimage.2013.04.127. arXiv: NIHMS150003.

Glasser, M. F., T. S. Coalson, E. C. Robinson, C. D. Hacker, J. Harwell, E. Yacoub, K. Ugurbil, J. Andersson, C. F. Beckmann, M. Jenkinson, S. M. Smith, and D. C. Van Essen (2016). "A Multi-Modal Parcellation of Human Cerebral Cortex". In: *Nature* 536.7615, pp. 171–178. DOI: 10.1038/nature18933.

Goodkind, M., S. B. Eickhoff, D. J. Oathes, Y. Jiang, A. Chang, L. B. Jones-Hagata, B. N. Ortega, Y. V. Zaiko, E. L. Roach, M. S. Korgaonkar, S. M. Grieve, I. Galatzer-Levy, P. T. Fox, and A. Etkin (2015). "Identification of a Common Neurobiological Substrate for Mental Illness". In: *JAMA Psychiatry* 72.4, p. 305. ISSN: 2168-622X. DOI: 10.1001/jamapsychiatry.2014.2206.

Grebenkov, D. S. (2008). "Laplacian Eigenfunctions in NMR. I. A Numerical Tool". In: *CONCEPTS IN MAGNETIC RESONANCE PART A* 32A.4, pp. 277–301. DOI: 10.1002/cmr.a.20117.

Grebenkov, D. S. (2009). "Laplacian Eigenfunctions in NMR. II. Theoretical Advances". In: *CONCEPTS IN MAGNETIC RESONANCE PART A* 34A, pp. 264–296. DOI: 10.1002/cmr.a.20145.

Greicius, M. D., B. Krasnow, A. L. Reiss, and V. Menon (2003). "Functional Connectivity in the Resting Brain: A Network Analysis of the Default Mode Hypothesis." In: *PNAS* 100.1, pp. 253–258. DOI: 10.1073/pnas.0135058100.

Grosenick, L., B. Klingenberg, K. Katovich, B. Knutson, and J. E. Taylor (2013). "Interpretable Whole-Brain Prediction Analysis with GraphNet". In: *NImg* 72, pp. 304–321. DOI: 10.1016/j.neuroimage.2012.12.062.

Gross, C. (1998). *Brain, Vision, Memory. Tales in the History of Neuroscience*. MIT Press.

Hahn, E. L. (1950). "Spin Echoes". In: *Phys. Rev.* 80, pp. 580–594. DOI: 10.1103/PhysRev.80.580.

Honey, C. J., O. Sporns, L. Cammoun, X. Gigandet, J. Thiran, R. Meuli, and P. Hagmann (2009). "Predicting Human Resting-State Functional Connectivity from Structural Connectivity". In: 106.6, p. 2035.

Hong, Y., L. J. O'Donnell, P. Savadjiev, F. Zhang, D. Wassermann, O. Pasternak, H. Johnson, J. Paulsen, J.-P. Vonsattel, N. Makris, C. F. Westin, and Y. Rathi (2018). "Genetic Load Determines Atrophy in Hand Cortico-Striatal Pathways in Presymptomatic Huntington's Disease". In: *Human Brain Mapping*. ISSN: 10659471. DOI: 10.1002/hbm.24217.

Hubel, D. H. and T. N. Wiesel (1962). “Receptive Fields, Binocular Interaction and Functional Architecture in the Cat’s Visual Cortex”. In: *The Journal of Physiology* 160.1, pp. 106–154. ISSN: 0022-3751. DOI: 10.1113/jphysiol.1962.sp006837.

Jbabdi, S. and T. E. J. Behrens (2013). “Long-Range Connectomics.” In: *Annals of the New York Academy of Sciences* 1305.1, pp. 83–93. DOI: 10.1111/nyas.12271.

Jelescu, I. O., J. Veraart, E. Fieremans, and D. S. Novikov (2015). “Degeneracy in Model Parameter Estimation for Multi-Compartmental Diffusion in Neuronal Tissue”. In: 29.1, pp. 33–47. DOI: 10.1002/nbm.3450.

Jeurissen, B., M. Descoteaux, S. Mori, and A. Leemans (2017). “Diffusion MRI Fiber Tractography of the Brain”. In: *NMR in Biomedicine* 0.0, e3785. ISSN: 1099-1492. DOI: 10.1002/nbm.3785.

Jilka, S. R., G. Scott, T. Ham, A. Pickering, V. Bonnelle, R. M. Braga, R. Leech, and D. J. Sharp (2014). “Damage to the Salience Network and Interactions with the Default Mode Network”. In: *J. Neurosci.* 34.33, pp. 10798–10807. ISSN: 0270-6474, 1529-2401. DOI: 10.1523/JNEUROSCI.0518-14.2014. pmid: 25122883.

Kanti V Mardia, P. E. J. (2000). *Directional Statistics*. Wiley Series in Probability and Statistics. J. Wiley. ISBN: 0-471-95333-4 978-0-471-95333-3.

Kärger, J. and W. Heink (1983). “The Propagator Representation of Molecular Transport in Microporous Crystallites”. In: *J Magn Reson* 51.1, pp. 1–7. DOI: 10.1016/0022-2364(83)90094-X.

Keller, C. J., C. J. Honey, P. Mégevand, L. Entz, I. Ulbert, and A. D. Mehta (2014). “Mapping Human Brain Networks with Cortico-Cortical Evoked Potentials”. In: *Philosophical Transactions of the Royal Society of London B: Biological Sciences* 369, pp. 20130528–20130528. DOI: 10.1098/rstb.2013.0528.

King, M. D., J. Houseman, S. A. Roussel, N. Van Bruggen, S. R. Williams, and D. G. Gadian (1994). “Q-Space Imaging of the Brain”. In: *Magnetic Resonance in Medicine* 32.6, pp. 707–713. ISSN: 07403194, 15222594. DOI: 10.1002/mrm.1910320605.

Kurth, F., S. B. Eickhoff, A. Schleicher, L. Hoemke, K. Zilles, and K. Amunts (2010). “Cytoarchitecture and Probabilistic Maps of the Human Posterior Insular Cortex”. In: *Cereb. Cortex* 20.6, pp. 1448–1461. ISSN: 1460-2199. DOI: 10.1093/cercor/bhp208. pmid: 19822572.

Lance, G. N. and W. T. Williams (1966). “Computer Programs for Hierarchical Polythetic Classification (" Similarity Analyses")”. In: *The Computer Journal* 9.1, p. 60.

Landis, J. R. and G. G. Koch (1977). “The Measurement of Observer Agreement for Categorical Data”. In: *Biometrics* 33.1, pp. 159–174. JSTOR: 2529310.

Latour, L. L., K. Svoboda, P. P. Mitra, and C. H. Sotak (1994). “Time-Dependent Diffusion of Water in a Biological Model System.” In: *PNAS* 91.4, pp. 1229–1233.

Lazar, M. and A. L. Alexander (2003). “An Error Analysis of White Matter Tractography Methods: Synthetic Diffusion Tensor Field Simulations”. In: 20.2, pp. 1140–1153. DOI: 10.1016/S1053-8119(03)00277-5.

Lebel, C., M. Gee, R. Camicioli, M. Wieler, W. Martin, and C. Beaulieu (2012). “Diffusion Tensor Imaging of White Matter Tract Evolution over the Lifespan”. In: *NeuroImage* 60, pp. 340–352. DOI: 10.1016/j.neuroimage.2011.11.094.

Lebel, C., L. Walker, A. Leemans, L. Phillips, and C. Beaulieu (2008). "Microstructural Maturation of the Human Brain from Childhood to Adulthood". In: 40.3, pp. 1044–1055. DOI: 10.1016/j.neuroimage.2007.12.053.

Lee, H.-H., E. Fieremans, and D. S. Novikov (2017). "What Dominates the Time Dependence of Diffusion Transverse to Axons: Intra- or Extra-Axonal Water?" In: *NImg*. DOI: 10.1016/j.neuroimage.2017.12.038.

Lefranc, S., P. Roca, M. Perrot, C. Poupon, D. Le Bihan, J.-F. Mangin, and D. Rivière (2016). "Groupwise connectivity-based parcellation of the whole human cortical surface using watershed-driven dimension reduction". In: *Med. Image Anal.* 30, pp. 11–29. ISSN: 13618415. DOI: 10.1016/j.media.2016.01.003.

Lindstrom, M. J. and D. M. Bates (1988). "Newton-Raphson and EM Algorithms for Linear Mixed-Effects Models for Repeated-Measures Data". In: *J Am Stat Asso* 83.404, p. 1014. DOI: 10.2307/2290128. JSTOR: 2290128?origin=crossref.

Maier-Hein, K. H., P. F. Neher, J.-C. Houde, M.-A. Côté, E. Garyfallidis, J. Zhong, M. Chamberland, F.-C. Yeh, Y.-C. Lin, Q. Ji, W. E. Reddick, J. O. Glass, D. Q. Chen, Y. Feng, C. Gao, Y. Wu, J. Ma, H. Renjie, Q. Li, C.-F. Westin, S. Deslauriers-Gauthier, J. O. O. González, M. Paquette, S. St-Jean, G. Girard, F. Rheault, J. Sidhu, C. M. W. Tax, F. Guo, H. Y. Mesri, S. Dávid, M. Froeling, A. M. Heemskerk, A. Leemans, A. Boré, B. Pinsard, C. Bedetti, M. Desrosiers, S. Brambati, J. Doyon, A. Sarica, R. Vasta, A. Cerasa, A. Quattrone, J. Yeatman, A. R. Khan, W. Hodges, S. Alexander, D. Romascano, M. Barakovic, A. Auría, O. Esteban, A. Lemkaddem, J.-P. Thiran, H. E. Cetingul, B. L. Odry, B. Mailhe, M. S. Nadar, F. Pizzagalli, G. Prasad, J. E. Villalon-Reina, J. Galvis, P. M. Thompson, F. D. S. Requejo, P. L. Laguna, L. M. Lacerda, R. Barrett, F. Dell'Acqua, M. Catani, L. Petit, E. Caruyer, A. Daducci, T. B. Dyrby, T. Holland-Letz, C. C. Hilgetag, B. Stieltjes, and M. Descoteaux (2017). "The Challenge of Mapping the Human Connectome Based on Diffusion Tractography". In: *Nature Communications* 8.1, p. 1349. ISSN: 2041-1723. DOI: 10.1038/s41467-017-01285-x.

Makris, N., D. N. Kennedy, S. McInerney, A. G. Sorensen, R. Wang, V. S. Caviness, and D. N. Pandya (2005). "Segmentation of Subcomponents within the Superior Longitudinal Fascicle in Humans: A Quantitative, In Vivo, DT-MRI Study". In: *Cereb Cortex* 15.6, pp. 854–869. ISSN: 1047-3211. DOI: 10.1093/cercor/bhh186.

Makris, N., J. W. Meyer, J. F. Bates, E. H. Yeterian, D. N. Kennedy, and V. S. Caviness (1999). "MRI-Based Topographic Parcellation of Human Cerebral White Matter and Nuclei: II. Rationale and Applications with Systematics of Cerebral Connectivity". In: 9.1, pp. 18–45. DOI: 10.1006/nimg.1998.0384.

Makris, N. and D. Pandya (2008). "The Extreme Capsule in Humans and Rethinking of the Language Circuitry". In: *Brain Struct Funct* 213.3, pp. 343–358. DOI: 10.1007/s00429-008-0199-8.

Malcolm, J. G., O. Michailovich, S. Bouix, C.-F. Westin, M. E. Shenton, and Y. Rathi (2010). "A Filtered Approach to Neural Tractography Using the Watson Directional Function". In: *IEEE Trans. Med. Imaging* 14, pp. 58–69.

Mandonnet, E., A. Nouet, P. Gatignol, L. Capelle, and H. Duffau (2007). "Does the Left Inferior Longitudinal Fasciculus Play a Role in Language? A Brain Stimulation Study". In: *Brain* 130.3, pp. 623–629. DOI: 10.1093/brain/awl361.

Marr, D. (1969). “A Theory of Cerebellar Cortex”. In: *The J Physiology* 202, pp. 437–470.

McCullagh, P. and J. A. Nelder (1989). *Generalized Linear Models*. 2nd ed. Chapman and Hall/CRC. ISBN: 978-0412317606.

Menon, V. and L. Q. Uddin (2010). “Saliency, Switching, Attention and Control: A Network Model of Insula Function”. In: *Brain Structure and Function* 214.5-6, pp. 655–667. ISSN: 1863-2653, 1863-2661. DOI: 10.1007/s00429-010-0262-0.

Mesulam, M.-M. and E. J. Mufson (1985). “The Insula of Reil in Man and Monkey”. In: *Association and Auditory Cortices*. Ed. by A. Peters and E. G. Jones. Red. by E. G. Jones and A. Peters. Vol. 4. Boston, MA: Springer US, pp. 179–226. ISBN: 978-1-4757-9621-6 978-1-4757-9619-3. DOI: 10.1007/978-1-4757-9619-3_5.

Meynert, T. (1867). “Das Gesammtgewicht Und Die Theilgewichte Des Gehirns in Ihren Beziehungen Zum Geschlechte, Dem Lebensalter Und Dem Irrsinn, Untersucht Nach Einer Neuen Wägungsmethode an Den Gehirnen Der in Der Wiener Irrenanstalt Im Jahre 1866 Verstorbenen”. In: *Vierteljahresschrift für Psychiatrie, Psychologie und gerichtliche Medicin* 1, pp. 125–170.

Mitra, P. P., L. L. Latour, R. L. Kleinberg, and C. H. Sotak (1995). “Pulsed-Field-Gradient NMR Measurements of Restricted Diffusion and the Return-to-the-Origin Probability”. In: *Journal of Magnetic Resonance, Series A* 114.1, pp. 47–58.

Mitra, P. P. and P. N. Sen (1992a). “Effects of Microgeometry and Surface Relaxation on NMR Pulsed-Field-Gradient Experiments: Simple Pore Geometries”. In: 45.1, pp. 143–156. DOI: 10.1103/PhysRevB.45.143.

Mitra, P. P., P. N. Sen, and L. M. Schwartz (1993). “Short-Time Behavior of the Diffusion Coefficient as a Geometrical Probe of Porous Media”. In: *Phys. Rev. B* 47.14, pp. 8565–8574. DOI: 10.1103/PhysRevB.47.8565.

Mitra, P. P., P. Sen, L. Schwartz, and Le Doussal P (1992b). “Diffusion Propagator as a Probe of the Structure of Porous Media.” In: *Phys. Rev. Lett.* 68.24, pp. 3555–3558. DOI: 10.1103/PhysRevLett.68.3555.

Morel, A., M. N. Gallay, A. Baechler, M. Wyss, and D. S. Gallay (2013). “The Human Insula: Architectonic Organization and Postmortem MRI Registration”. In: *Neuroscience* 236.C, pp. 117–135. DOI: 10.1016/j.neuroscience.2012.12.076.

Moreno-Dominguez, D., A. Anwander, and T. R. Knösche (2014). “A Hierarchical Method for Whole-Brain Connectivity-Based Parcellation.” In: *Human Brain Mapping* 35.10, pp. 5000–5025. DOI: 10.1002/hbm.22528.

Mori, S., B. J. Crain, V. P. Chacko, and P. C. van Zijl (1999). “Three-Dimensional Tracking of Axonal Projections in the Brain by Magnetic Resonance Imaging”. In: *Ann Neur* 45.2, pp. 265–269. DOI: 10.1002/1531-8249(199902)45:2<265::AID-ANA21>3.0.CO;2-3.

Murday, J. S. and R. M. Cotts (1968). “Self-Diffusion Coefficient of Liquid Lithium”. In: 48.11, p. 4938. DOI: 10.1063/1.1668160.

Murtagh, F. (1983). “A Survey of Recent Advances in Hierarchical Clustering Algorithms”. In: 26.4, p. 354.

Namkung, H., S.-H. Kim, and A. Sawa (2017). "The Insula: An Underestimated Brain Area in Clinical Neuroscience, Psychiatry, and Neurology." In: *Trends Neurosci.* 40.4, pp. 200–207. DOI: 10.1016/j.tins.2017.02.002.

Neuman, C. H. (1973). "Spin Echo of Spins Diffusing in a Bounded Medium". In: *The Journal of Chemical Physics* 60.11, pp. 4508–4511. DOI: 10.1063/1.1680931.

Nichols, T. E. and A. P. Holmes (2002). "Nonparametric Permutation Tests for Functional Neuroimaging: A Primer with Examples." In: *Human Brain Mapping* 15.1, pp. 1–25.

Nilsson, M., J. Lätt, F. Ståhlberg, D. van Westen, and H. Hagslätt (2012). "The Importance of Axonal Undulation in Diffusion MR Measurements: A Monte Carlo Simulation Study". In: *NMR in Biomedicine* 25.5, pp. 795–805. DOI: 10.1002/nbm.1795.

Nimchinsky, E. A., E. Gilissen, J. M. Allman, D. P. Perl, J. M. Erwin, and P. R. Hof (1999). "A Neuronal Morphologic Type Unique to Humans and Great Apes". In: *Proceedings of the National Academy of Sciences* 96.9, pp. 5268–5273. ISSN: 0027-8424, 1091-6490. DOI: 10.1073/pnas.96.9.5268.

Ning, L., F. Laun, Y. Gur, E. V. R. DiBella, S. Deslauriers-Gauthier, T. Megherbi, A. Ghosh, M. Zucchelli, G. Menegaz, R. Fick, S. St-Jean, M. Paquette, R. Aranda, M. Descoteaux, R. Deriche, L. O'Donnell, and Y. Rathi (2015). "Sparse Reconstruction Challenge for Diffusion MRI: Validation on a Physical Phantom to Determine Which Acquisition Scheme and Analysis Method to Use?" In: *Medical Image Analysis* 26.1, pp. 316–331. ISSN: 1361-8415. DOI: 10.1016/j.media.2015.10.012.

Ning, L., K. Setsompop, C.-F. Westin, and Y. Rathi (2017). "New Insights about Time-Varying Diffusivity and Its Estimation from Diffusion MRI". In: *Magnetic Resonance in Medicine* 78.2, pp. 763–774. ISSN: 1522-2594. DOI: 10.1002/mrm.26403.

Novikov, D. S., E. Fieremans, S. N. Jespersen, and V. G. Kiselev (2018a). "Quantifying Brain Microstructure with Diffusion MRI: Theory and Parameter Estimation: Brain Microstructure with dMRI: Theory and Parameter Estimation". In: *NMR in Biomedicine*, e3998. ISSN: 09523480. DOI: 10.1002/nbm.3998.

Novikov, D. S., J. Veraart, I. O. Jelescu, and E. Fieremans (2018b). "Rotationally-Invariant Mapping of Scalar and Orientational Metrics of Neuronal Microstructure with Diffusion MRI". In: *NeuroImage* 174, pp. 518–538. ISSN: 10538119. DOI: 10.1016/j.neuroimage.2018.03.006.

Novikov, D. S., J. H. Jensen, J. A. Helpern, and E. Fieremans (2014). "Revealing Mesoscopic Structural Universality with Diffusion." In: *Proc. Natl. Acad. Sci. U.S.A.* 111.14, pp. 5088–5093. DOI: 10.1073/pnas.1316944111.

O'Donnell, L. J. and C.-F. Westin (2007). "Automatic Tractography Segmentation Using a High-Dimensional White Matter Atlas". In: *IEEE Trans. Med. Imaging* 26.11, pp. 1562–1575.

Özarslan, E., C. G. Koay, T. M. Shepherd, M. E. Komlosh, M. O. İrfanoğlu, C. Pierpaoli, and P. J. Basser (2013). "Mean Apparent Propagator (MAP) MRI: A Novel Diffusion Imaging Method for Mapping Tissue Microstructure." In: *NImg* 78, pp. 16–32. DOI: 10.1016/j.neuroimage.2013.04.016.

Palaniyappan, L., M. Simmonite, T. P. White, E. B. Liddle, and P. F. Liddle (2013). "Neural Primacy of the Salience Processing System in Schizophrenia". In: *Neuron* 79.4, pp. 814–828. ISSN: 1097-4199. DOI: 10.1016/j.neuron.2013.06.027. pmid: 23972602.

Palombo, M., N. Shemesh, I. Ronen, and J. Valette (2018). "Insights into Brain Microstructure from in Vivo DW-MRS". In: *NeuroImage* 182, pp. 97–116. ISSN: 10538119. DOI: 10.1016/j.neuroimage.2017.11.028.

Parisot, S., S. Arslan, J. Passerat-Palmbach, W. M. Wells, and D. Rueckert (2015). "Tractography-Driven Groupwise Multi-scale Parcellation of the Cortex." In: *Inf. Process. Med. Imaging*. Lecture Notes in Computer Science 24. Ed. by S. Ourselin, D. C. Alexander, C.-F. Westin, and M. J. Cardoso, pp. 600–12. ISSN: 1011-2499. DOI: 10.1007/978-3-319-19992-4.

Parker, G. J. M. and D. C. Alexander (2005). "Probabilistic Anatomical Connectivity Derived from the Microscopic Persistent Angular Structure of Cerebral Tissue". In: *Philosophical Transactions of the Royal Society B: Biological Sciences* 360, pp. 893–902.

Passingham, R. E., K. E. Stephan, and R. Kötter (2002). "The anatomical basis of functional localization in the cortex". In: *Nat. Rev. Neurosci.* 3.8, pp. 606–616. ISSN: 1471-003X. DOI: 10.1038/nrn893.

Paulsen, J. S., J. D. Long, C. A. Ross, D. L. Harrington, C. J. Erwin, J. K. Williams, H. J. Westervelt, H. J. Johnson, E. H. Aylward, Y. Zhang, H. J. Bockholt, and R. A. Barker (2014). "Prediction of Manifest Huntington's Disease with Clinical and Imaging Measures: A Prospective Observational Study". In: *The Lancet Neurology* 13.12, pp. 1193–1201. ISSN: 1474-4422. DOI: 10.1016/S1474-4422(14)70238-8.

Paxinos, G., X. F. Huang, and A. W. Toga (2000). *The Rhesus Monkey Brain in Stereotaxic Coordinates*. San Diego, CA: Academic Press. 163 pp. ISBN: 978-0-12-358255-3.

Peña-Reyes, C. A. and M. Sipper (2000). "Evolutionary Computation in Medicine: An Overview". In: *Artificial Intelligence in Medicine*. Evolutionary Computation in Medicine 19.1, pp. 1–23. ISSN: 0933-3657. DOI: 10.1016/S0933-3657(99)00047-0.

Pendergast, J. F., S. J. Gange, M. A. Newton, M. J. Lindstrom, M. Palta, and M. R. Fisher (1996). "A Survey of Methods for Analyzing Clustered Binary Response Data". In: 64.1, p. 89. DOI: 10.2307/1403425. JSTOR: 1403425?origin=crossref.

Pohl, K. M., J. Fisher, S. Bouix, M. Shenton, R. W. McCarley, W. E. L. Grimson, R. Kikinis, and W. M. Wells III (2007). "Using the Logarithm of Odds to Define a Vector Space on Probabilistic Atlases." In: *Medical Image Analysis* 11.5, pp. 465–477. DOI: 10.1016/j.media.2007.06.003.

Poldrack, R. A. and T. Yarkoni (2016). "From Brain Maps to Cognitive Ontologies: Informatics and the Search for Mental Structure." In: *Annu Rev Psychol* 67.1, pp. 587–612. DOI: 10.1146/annurev-psych-122414-033729.

Raichle, M. E., A. M. MacLeod, A. Z. Snyder, W. J. Powers, D. A. Gusnard, and G. L. Shulman (2001). "A Default Mode of Brain Function". In: *PNAS* 98.2, pp. 676–682. ISSN: 0027-8424, 1091-6490. DOI: 10.1073/pnas.98.2.676. pmid: 11209064.

Roberts, M. and J. Hanaway (1970). *Atlas of the Human Brain in Section*. Philadelphia: Lea & Febiger. 95 pp. ISBN: 978-0-8121-0261-1.

Roca, P., D. Rivière, P. Guevara, C. Poupon, and J. F. Mangin (2009). "Tractography-based parcellation of the cortex using a spatially-informed dimension reduction of the connectivity matrix". In: *Lect. Notes Comput. Sci. (including Subser. Lect. Notes Artif. Intell. Lect. Notes Bioinformatics)* 5761 LNCS.PART 1, pp. 935–942. ISSN: 03029743. DOI: 10.1007/978-3-642-04268-3_115.

Roca, P., A. Tucholka, D. Rivière, P. Guevara, C. Poupon, and J. F. Mangin (2010). "Inter-subject connectivity-based parcellation of a patch of cerebral cortex". In: *Lect. Notes Comput. Sci. (including Subser. Lect. Notes Artif. Intell. Lect. Notes Bioinformatics)* 6362 LNCS.PART 2, pp. 347–354. ISSN: 03029743. DOI: 10.1007/978-3-642-15745-5_43.

Ronen, I., M. Budde, E. Ercan, J. Annese, A. Techawiboonwong, and A. Webb (2014). "Microstructural Organization of Axons in the Human Corpus Callosum Quantified by Diffusion-Weighted Magnetic Resonance Spectroscopy of N-Acetylaspartate and Post-Mortem Histology". In: 219.5, pp. 1773–1785. DOI: 10.1007/s00429-013-0600-0.

Ross, C. A., E. H. Aylward, E. J. Wild, D. R. Langbehn, J. D. Long, J. H. Warner, R. I. Scahill, B. R. Leavitt, J. C. Stout, J. S. Paulsen, R. Reilmann, P. G. Unschuld, A. Wexler, R. L. Margolis, and S. J. Tabrizi (2014). "Huntington Disease: Natural History, Biomarkers and Prospects for Therapeutics". In: *Nature Reviews Neurology* 10.4, pp. 204–216. ISSN: 1759-4766. DOI: 10.1038/nrneurol.2014.24.

Sabat, S., R. Mir, M. Guarini, A. Guesalaga, and P. Irarrazaval (2003). "Three Dimensional K-Space Trajectory Design Using Genetic Algorithms". In: *Magnetic Resonance Imaging* 21.7, pp. 755–764. ISSN: 0730-725X. DOI: 10.1016/S0730-725X(03)00174-7.

Salat, D. H., D. N. Greve, J. L. Pacheco, B. T. Quinn, K. G. Helmer, R. L. Buckner, and B. Fischl (2009). "Regional White Matter Volume Differences in Nondemented Aging and Alzheimer's Disease". In: 44.4, pp. 1247–1258. DOI: 10.1016/j.neuroimage.2008.10.030.

Saleem, K. S. and N. Logothetis (2007). *A Combined MRI and Histology Atlas of the Rhesus Monkey Brain in Stereotaxic Coordinates*. OCLC: ocm72146944. London ; Burlington, MA: Academic. 326 pp. ISBN: 978-0-12-372559-2.

Saygin, Z. M., D. E. Osher, E. S. Norton, D. A. Youssoufian, S. D. Beach, J. Feather, N. Gaab, J. D. E. Gabrieli, and N. Kanwisher (2016). "Connectivity Precedes Function in the Development of the Visual Word Form Area". In: *Nature Publishing Group* 19.9, nn.4354–1255. DOI: 10.1038/nn.4354.

Schmahmann, J. D. and D. N. Pandya (2006). *Fiber Pathways of the Brain*. OCLC: ocm59279675. Oxford ; New York: Oxford University Press. 654 pp. ISBN: 978-0-19-510423-3.

Schmahmann, J. D. and D. Pandya (2007). "Cerebral White Matter—Historical Evolution of Facts and Notions Concerning the Organization of the Fiber Pathways of the Brain". In: 16.3, pp. 237–267.

Searle, J. R. (2004). *Mind: A Brief Introduction*. oxford university press. ISBN: 0-19-972900-X.

Seeley, W. W., F. T. Merkle, S. E. Gaus, A. D. (Craig, J. M. Allman, and P. R. Hof (2012). "Distinctive Neurons of the Anterior Cingulate and Frontoinsular Cortex: A Historical Perspective". In: *Cerebral Cortex* 22.2, pp. 245–250. DOI: 10.1093/cercor/bhr005.

Sepehrband, F., K. O'Brien, and M. Barth (2017). "A Time-Efficient Acquisition Protocol for Multipurpose Diffusion-Weighted Microstructural Imaging at 7 Tesla". In: *Magnetic Resonance in Medicine* 78.6, pp. 2170–2184. ISSN: 1522-2594. DOI: 10.1002/mrm.26608.

Setsompop, K., R. Kimmlingen, E. Eberlein, T. Witzel, J. Cohen-Adad, J. A. McNab, B. Keil, M. D. Tisdall, P. Hoecht, P. Dietz, S. F. Cauley, V. Tountcheva, V. Matschl, V. H. Lenz, K. Heberlein, A. Potthast, H. Thein, J. Van Horn, A. Toga, F. Schmitt, D. Lehne, B. R. Rosen, V. Wedeen, and L. L. Wald (2013). "Pushing the Limits of in Vivo Diffusion MRI for the Human Connectome Project". In: 80, pp. 220–233. DOI: 10.1016/j.neuroimage.2013.05.078.

Siless, V., K. Chang, B. Fischl, and A. Yendiki (2018). "AnatomiCuts: Hierarchical Clustering of Tractography Streamlines Based on Anatomical Similarity". In: *NeuroImage* 166, pp. 32–45. ISSN: 1053-8119. DOI: 10.1016/j.neuroimage.2017.10.058.

Solstad, T., C. N. Boccara, E. Kropff, M.-B. Moser, and E. I. Moser (2008). "Representation of Geometric Borders in the Entorhinal Cortex". In: *Science* 322.5909, pp. 1865–1868. ISSN: 0036-8075, 1095-9203. DOI: 10.1126/science.1166466. pmid: 19095945.

Song, S. K., J. Yoshino, T. Q. Le, S. J. Lin, S. W. Sun, A. C. Neuroimage, and 2005 (2005). "Demyelination Increases Radial Diffusivity in Corpus Callosum of Mouse Brain". In: *Elsevier*. DOI: 10.1016/j.neuroimage.2005.01.028.

Sotiropoulos, S. N., S. Jbabdi, J. Xu, J. L. Andersson, S. Moeller, E. J. Auerbach, M. F. Glasser, M. Hernandez, G. Sapiro, M. Jenkinson, D. A. Feinberg, E. Yacoub, C. Lenglet, D. C. Van Essen, K. Ugurbil, and T. E. J. Behrens (2013). "Advances in Diffusion MRI Acquisition and Processing in the Human Connectome Project". In: 80, pp. 125–143. DOI: 10.1016/j.neuroimage.2013.05.057.

Stejskal, E. O. and J. E. Tanner (1965). "Spin Diffusion Measurements: Spin Echoes in the Presence of a Time-Dependent Field Gradient". In: *The Journal of Chemical Physics* 42.1, pp. 288–292. ISSN: 0021-9606, 1089-7690. DOI: 10.1063/1.1695690.

Swick, D., V. Ashley, and U. Turken (2011). "Are the Neural Correlates of Stopping and Not Going Identical? Quantitative Meta-Analysis of Two Response Inhibition Tasks". In: *NeuroImage* 56.3, pp. 1655–1665. ISSN: 1053-8119. DOI: 10.1016/j.neuroimage.2011.02.070.

Taghia, J., W. Cai, S. Ryali, J. Kochalka, J. Nicholas, T. Chen, and V. Menon (2018). "Uncovering Hidden Brain State Dynamics That Regulate Performance and Decision-Making during Cognition". In: *Nature Communications* 9.1, p. 2505. ISSN: 2041-1723. DOI: 10.1038/s41467-018-04723-6.

Tanner, J. E. and E. O. Stejskal (1968). "Restricted Self-Diffusion of Protons in Colloidal Systems by the Pulsed-Gradient, Spin-Echo Method". In: *The Journal of Chemical Physics* 49.4, pp. 1768–1777. ISSN: 0021-9606, 1089-7690. DOI: 10.1063/1.1670306.

Thiebaut de Schotten, M. (2005). "Direct Evidence for a Parietal-Frontal Pathway Subserving Spatial Awareness in Humans". In: *Science* 309.5744, pp. 2226–2228. DOI: 10.1126/science.1116251.

Thiebaut de Schotten, M., F. Dell'acqua, S. J. Forkel, A. Simmons, F. Vergani, D. G. M. Murphy, and M. Catani (2011a). "A Lateralized Brain Network for Visuospatial Attention". In: *Nat Neurosci* 14, pp. 1245–1246. DOI: 10.1038/nn.2905.

Thiebaut de Schotten, M., D. H. Ffytche, A. Bizzi, F. Dell'acqua, M. Allin, M. Walshe, R. Murray, S. C. R. Williams, D. G. Murphy, and M. Catani (2011b). "Atlasing Location, Asymmetry and Inter-Subject Variability of White Matter Tracts in the Human Brain with MR Diffusion Tractography". In: *NImg* 54.1, pp. 49–59. DOI: 10.1016/j.neuroimage.2010.07.055.

Thiebaut de Schotten, M., M. Urbanski, B. Batrancourt, R. Levy, B. Dubois, L. Cerliani, and E. Volle (2016). "Rostro-Caudal Architecture of the Frontal Lobes in Humans". In: *Cerebral Cortex*. ISSN: 1047-3211, 1460-2199. DOI: 10.1093/cercor/bhw215.

Thiebaut de Schotten, M., M. Urbanski, R. Valabregue, D. J. Bayle, and E. Volle (2014). "Subdivision of the Occipital Lobes: An Anatomical and Functional MRI Connectivity Study". In: *Cortex* 56, pp. 121–137. DOI: 10.1016/j.cortex.2012.12.007.

Thirion, B., G. Varoquaux, E. Dohmatob, and J.-B. Poline (2014). "Which fMRI Clustering Gives Good Brain Parcellations?" In: *Front. Neurosci.* 8.171, p. 169. DOI: 10.3389/fnins.2014.00167.

Tremblay, P. and A. S. Dick (2016). "Broca and Wernicke Are Dead, or Moving Past the Classic Model of Language Neurobiology". In: 162, pp. 60–71. DOI: 10.1016/j.bandl.2016.08.004.

Uddin, L. Q. (2015). "Salience Processing and Insular Cortical Function and Dysfunction". In: *Nature Reviews Neuroscience* 16.1, pp. 55–61. ISSN: 1471-003X, 1471-0048. DOI: 10.1038/nrn3857.

Uddin, L. Q. and V. Menon (2010). "Introduction to Special Topic – Resting-State Brain Activity: Implications for Systems Neuroscience". In: *Front. Syst. Neurosci.* 4. ISSN: 1662-5137. DOI: 10.3389/fnsys.2010.00037.

Van Gelderen, P., D. Despres, P. C. M. van Zijl, and C. T. W. Moonen (1994). "Evaluation of Restricted Diffusion in Cylinders. Phosphocreatine in Rabbit Leg Muscle". In: 103, pp. 255–260. DOI: 10.1006/jmrb.1994.1038.

Veraart, J., E. Fieremans, and D. S. Novikov (2019). "On the Scaling Behavior of Water Diffusion in Human Brain White Matter". In: *NeuroImage* 185, pp. 379–387. ISSN: 10538119. DOI: 10.1016/j.neuroimage.2018.09.075.

Vogt, B. A., E. A. Nimchinsky, L. J. Vogt, and P. R. Hof (1995). "Human Cingulate Cortex: Surface Features, Flat Maps, and Cytoarchitecture". In: *The Journal of Comparative Neurology* 359.3, pp. 490–506. ISSN: 0021-9967, 1096-9861. DOI: 10.1002/cne.903590310.

Von Economo, C. (1926). "A New Type of Special Cells of the Cingulate and Insular Lobes". In: *Z Ges Neurol Psychiatr* 100, pp. 707–712.

Von Economo, C. F. and G. N. Koskinas (1925). *Die Cytoarchitektonik Der Hirnrinde Des Erwachsenen Menschen*. J. Springer.

Vonsattel, J. P. G. and M. Difiglia (1998). "Huntington Disease". In: *J Neuropathol Exp Neurol* 57.5, pp. 369–384. ISSN: 0022-3069. DOI: 10.1097/00005072-199805000-00001.

Wakana, S., H. Jiang, L. Nagae-Poetscher, P. C. M. van Zijl, and S. Mori (2004). "Fiber Tract–Based Atlas of Human White Matter Anatomy". In: *Radiology* 230, pp. 77–87.

Wakana, S., A. Caprihan, M. M. Panzenboeck, J. H. Fallon, M. Perry, R. L. Gollub, K. Hua, J. Zhang, H. Jiang, P. Dubey, A. Blitz, P. C. van Zijl, and S. Mori (2007). "Reproducibility of Quantitative Tractography Methods Applied to Cerebral White Matter". In: 36.3, pp. 630–644. DOI: 10.1016/j.neuroimage.2007.02.049.

Wang, X., W. E. L. Grimson, and C.-F. Westin (2011a). "Tractography Segmentation Using a Hierarchical Dirichlet Processes Mixture Model". In: 54.1, pp. 290–302. DOI: 10.1016/j.neuroimage.2010.07.050.

Wang, Y., Q. Wang, J. P. Haldar, F.-C. Yeh, M. Xie, P. Sun, T.-W. Tu, K. Trinkaus, R. S. Klein, A. H. Cross, and S.-K. Song (2011b). "Quantification of Increased Cellularity during Inflammatory Demyelination." In: *Brain* 134 (Pt 12), pp. 3590–3601. DOI: 10.1093/brain/awr307.

Ward Jr., J. (1963). “Hierarchical Grouping to Optimize an Objective Function”. In: *J. Am. Stat. Assoc.* 58.301, pp. 236–244.

Wassermann, D. (2010). “Automated In Vivo Dissection of White Matter Structures from Diffusion Magnetic Resonance Imaging”. INRIA Sophia-Antipolis/Université de Nice - France.

Wassermann, D., L. Bloy, E. Kanterakis, R. Verma, and R. Deriche (2010). “Unsupervised White Matter Fiber Clustering and Tract Probability Map Generation: Applications of a Gaussian Process Framework for White Matter Fibers.” In: *NImg* 51.1, pp. 228–241. DOI: 10.1016/j.neuroimage.2010.01.004.

Wassermann, D., N. Makris, Y. Rathi, M. Shenton, R. Kikinis, M. Kubicki, and C.-F. Westin (2016). “The White Matter Query Language: A Novel Approach for Describing Human White Matter Anatomy.” In: *Brain Structure and Function*. DOI: 10.1007/s00429-015-1179-4.

Wassermann, D., V. D. Nguyen, G. Gallardo-Diez, J.-R. Li, W. Cai, and V. Menon (2018). “Sensing Spindle Neurons in the Insula with Multi-Shell Diffusion MRI”. In: Annual Meeting ISMRM-ESMRMB, June 16-21 2018.

Wernicke, C. (1874). *Der Aphasische Symptomencomplex: Eine Psychologische Studie Auf Anatomischer Basis*. Berlin Heidelberg: Springer-Verlag. ISBN: 978-3-540-06905-8.

Wilkins, R. H. (1964). “Neurosurgical Classic-XVII: Edwin Smith Surgical Papyrus”. In: *Journal of Neurosurgery* 21.3, pp. 240–244.

Witelson, S. F. (1989). “Hand And Sex Differences In The Isthmus And Genu Of The Human Corpus Callosum”. In: *Brain* 112.3, pp. 799–835. DOI: 10.1093/brain/112.3.799.

Wu, Y.-C. and A. L. Alexander (2007). “Hybrid Diffusion Imaging”. In: *NeuroImage* 36.3, pp. 617–629. ISSN: 10538119. DOI: 10.1016/j.neuroimage.2007.02.050.

Yarkoni, T., R. A. Poldrack, T. E. Nichols, D. C. Van Essen, and T. D. Wager (2011). “Large-Scale Automated Synthesis of Human Functional Neuroimaging Data”. In: *Nat Meth* 8.8, pp. 665–670. DOI: 10.1038/nmeth.1635.

Yeatman, J. D., R. F. Dougherty, N. J. Myall, B. A. Wandell, and H. M. Feldman (2012). “Tract Profiles of White Matter Properties: Automating Fiber-Tract Quantification”. In: *Plos One* 7.11, e49790. DOI: 10.1371/journal.pone.0049790.

Yeatman, J. D., K. S. Weiner, F. Pestilli, A. Rokem, A. Mezer, and B. A. Wandell (2014). “The Vertical Occipital Fasciculus: A Century of Controversy Resolved by in Vivo Measurements.” In: *Proc. Natl. Acad. Sci. U.S.A.* 111.48, E5214–23. DOI: 10.1073/pnas.1418503111.

Yendiki, A., P. Panneck, P. Srinivasan, A. Stevens, L. Zollei, J. Augustinack, R. Wang, D. Salat, S. Ehrlich, T. E. J. Behrens, S. Jbabdi, R. Gollub, and B. Fischl (2011). “Automated Probabilistic Reconstruction of White-Matter Pathways in Health and Disease Using an Atlas of the Underlying Anatomy.” In: *Front. Neuroinform.* 5, p. 23. DOI: 10.3389/fninf.2011.00023.

Yeo, B. T. T. and S. B. Eickhoff (2016). “Systems Neuroscience: A Modern Map of the Human Cerebral Cortex”. In: *Nature* 536.7615, pp. 152–154. ISSN: 1476-4687. DOI: 10.1038/nature18914.

Zhang, F., Y. Wu, I. Norton, Y. Rathi, A. J. Golby, and L. J. O’Donnell (2019). “Test–Retest Reproducibility of White Matter Parcellation Using Diffusion MRI Tractography Fiber Clustering”. In: *Human Brain Mapping*. ISSN: 1065-9471, 1097-0193. DOI: 10.1002/hbm.24579.

Zhang, F., Y. Wu, I. Norton, L. Rigolo, Y. Rathi, N. Makris, and L. J. O'Donnell (2018). "An Anatomically Curated Fiber Clustering White Matter Atlas for Consistent White Matter Tract Parcellation across the Lifespan". In: *NeuroImage* 179, pp. 429–447. ISSN: 1053-8119. DOI: 10.1016/j.neuroimage.2018.06.027.

Zhang, H., T. Schneider, C. A. Wheeler-Kingshott, and D. C. Alexander (2013). "NODDI: Practical in Vivo Neurite Orientation Dispersion and Density Imaging of the Human Brain". In: 61.4, pp. 1000–1016.

Zhang, Y., J. Zhang, K. Oishi, A. V. Faria, H. Jiang, X. Li, K. Akhter, P. Rosa-Neto, G. B. Pike, A. C. Evans, A. W. Toga, R. Woods, J. C. Mazziotta, M. I. Miller, P. C. M. van Zijl, and S. Mori (2010). "Atlas-Guided Tract Reconstruction for Automated and Comprehensive Examination of the White Matter Anatomy". In: 52, pp. 1289–1301. ISSN: 1053-8119. DOI: doi:DOI:10.1016/j.neuroimage.2010.05.049.

Zilles, K. and K. Amunts (2013). "Individual Variability Is Not Noise." In: *TRENDS in Cognitive Sciences* 17.4, pp. 153–155. DOI: 10.1016/j.tics.2013.02.003.

Zou, H. and T. Hastie (2005). "Regularization and Variable Selection via the Elastic Net". In: 67.2, pp. 301–320. DOI: 10.1111/j.1467-9868.2005.00503.x.

Complete List of Publications

Journals

Fick, R. H., A. Petiet, M. Santin, A.-C. Philippe, S. Lehericy, R. Deriche, and D. Wassermann (2018a). "Non-parametric graphnet-regularized representation of dMRI in space and time". In: *Medical Image Analysis* 43, pp. 37–53.

Filipiak, P., R. Fick, A. Petiet, M. Santin, A.-C. Philippe, S. Lehericy, P. Ciuciu, R. Deriche, and D. Wassermann (2018a). "Reducing the number of samples in spatiotemporal dMRI acquisition design". In: *Magnetic resonance in medicine*.

Gallardo, G., W. Wells III, R. Deriche, and D. Wassermann (2018c). "Groupwise structural parcellation of the whole cortex: A logistic random effects model based approach". In: *Neuroimage* 170, pp. 307–320.

Hong, Y., L. J. O'Donnell, P. Savadjiev, F. Zhang, D. Wassermann, O. Pasternak, H. Johnson, J. Paulsen, J.-P. Vonsattel, N. Makris, et al. (2018). "Genetic load determines atrophy in hand cortico-striatal pathways in presymptomatic Huntington's disease". In: *Human Brain Mapping* 39.10, pp. 3871–3883.

Sydnor, V. J., A. M. Rivas-Grajales, A. E. Lyall, F. Zhang, S. Bouix, S. Karmacharya, M. E. Shenton, C.-F. Westin, N. Makris, D. Wassermann, et al. (2018). "A comparison of three fiber tract delineation methods and their impact on white matter analysis". In: *NeuroImage* 178, pp. 318–331.

Girard, G., A. Daducci, L. Petit, J.-P. Thiran, K. Whittingstall, R. Deriche, D. Wassermann*, and M. Descoteaux* (2017). "AxTract: Toward microstructure informed tractography". In: *Human Brain Mapping*.

Norton, I., W. I. Essayed, F. Zhang, S. Pujol, A. Yarmarkovich, A. J. Golby, G. Kindlmann, D. Wassermann, R. S. J. Estepar, Y. Rathi, et al. (2017). "SlicerDMRI: Open Source Diffusion MRI Software for Brain Cancer Research". In: *Cancer Research* 77.21, e101–e103.

O'Donnell, L. J., A. Daducci, D. Wassermann, and C. Lenglet (2017). "Advances in computational and statistical diffusion MRI". In: *NMR in Biomedicine*, e3805.

Fick, R. H., D. Wassermann, E. Caruyer, and R. Deriche (2016b). "MAPL: Tissue microstructure estimation using Laplacian-regularized MAP-MRI and its application to HCP data". In: *NeuroImage* 134, pp. 365–385.

Wassermann, D., N. Makris, Y. Rathi, M. Shenton, R. Kikinis, M. Kubicki, and C.-F. Westin (2016a). "The white matter query language: a novel approach for describing human white matter anatomy". In: *Brain Structure and Function* 221.9, pp. 4705–4721.

Garyfallidis, E., O. Ocegueda, D. Wassermann, and M. Descoteaux (2015). "Robust and efficient linear registration of white-matter fascicles in the space of streamlines". In: *NeuroImage* 117, pp. 124–140.

Matsui, J., J. Vaidya, D. Wassermann, R. Kim, V. Magnotta, H. J. Johnson, J. S. Paulsen, P.-H. Investigators, and C. o. T. H. S. Group (2015). "Prefrontal cortex white matter tracts in prodromal Huntington disease". In: *Human Brain Mapping*.

Wassermann*, D., D. Jolles*, R. Chokhani, J. Richardson, C. Tenison, R. Bammer, L. Fuchs, K. Supekar, and V. Menon (2015b). "Plasticity of left perisylvian white-matter tracts is associated with individual differences in math learning". In: *Brain Structure and Function*.

Egger, K., C. Clemm von Hohenberg, M. F. Schocke, C. R. Guttmann, D. Wassermann, M. C. Wigand, W. Nachbauer, C. Kremser, B. Sturm, B. Scheiber-Mojdehkar, et al. (2014). "White Matter Changes in Patients with Friedreich Ataxia after Treatment with Erythropoietin". In: *Journal of Neuroimaging* 24.5, pp. 504–508.

Kim, R., J. Matsui, D. Wassermann, J. Vaidya, H. Johnson, V. Magnotta, J. Long, J. Mills, M. Lowe, K. Sakaie, et al. (2014). "E17 Diffusion Weighted Imaging Study Of Prefrontal Cortex White Matter In Prodromal Huntington Disease". In: *Journal of Neurology, Neurosurgery & Psychiatry* 85.Suppl 1, A42–A42.

Makris, N., M. Preti, D. Wassermann, Y. Rathi, G. Papadimitriou, C. Yergatian, B. Dickerson, M. Shenton, and M. Kubicki (2013). "Human middle longitudinal fascicle: segregation and behavioral-clinical implications of two distinct fiber connections linking temporal pole and superior temporal gyrus with the angular gyrus or superior parietal lobule using multi-tensor tractography". In: *Brain imaging and behavior* 7.3, pp. 335–352.

Princich, J. P., D. Wassermann, F. Latini, S. Oddo, A. O. Blenkmann, G. Seifer, and S. P. Kochen (2013b). "Rapid and efficient localization of depth electrodes and cortical labeling using free and open source medical software in epilepsy surgery candidates". In: *Frontiers in neuroscience* 7, p. 260.

Wassermann, D., L. Bloy, E. Kanterakis, R. Verma, and R. Deriche (2010a). "Unsupervised white matter fiber clustering and tract probability map generation: Applications of a Gaussian process framework for white matter fibers". In: *NeuroImage* 51.1, pp. 228–241.

Delmaire, C., M. Vidailhet, D. Wassermann, M. Descoteaux, R. Valabregue, F. Bourdain, C. Lenglet, S. Sangla, A. Terrier, R. Deriche, et al. (2009). "Diffusion abnormalities in the primary sensorimotor pathways in writer's cramp". In: *Archives of neurology* 66.4, pp. 502–508.

Lenglet, C., J. Campbell, M. Descoteaux, G. Haro, P. Savadjiev, D. Wassermann, A. Anwander, R. Deriche, G. B. Pike, G. Sapiro, et al. (2009). "Mathematical methods for diffusion MRI processing". In: *Neuroimage* 45.1, S111–S122.

Wassermann, D., M. Descoteaux, and R. Deriche (2008b). "Diffusion maps clustering for magnetic resonance Q-Ball imaging segmentation". In: *Journal of Biomedical Imaging* 2008, p. 5.

Wainer, G. A., S. Daicz, L. F. De Simoni, and D. Wassermann (2001). "Using the ALFA-1 simulated processor for educational purposes". In: *Journal on Educational Resources in Computing (JERIC)* 1.4, pp. 111–151.

Conference Proceedings

Filipiak, P., R. Fick, A. Petiet, M. Santin, A.-C. Philippe, S. Lehericy, R. Deriche, and D. Wassermann (2019). "Coarse-Grained Spatiotemporal Acquisition Design for Diffusion MRI". In: *ISBI 2019-Proceedings of The IEEE International Symposium on Biomedical Imaging*.

Alimi, A., R. Fick, D. Wassermann, and R. Deriche (2018a). "Dmipy, a Diffusion Microstructure Imaging toolbox in Python to improve research reproducibility". In: *Computational Diffusion MRI 2018*.

Alimi, A., A. Petiet, M. Santin, A.-C. Philippe, S. Lehéricy, R. Deriche, and D. Wassermann (2018b). "Towards the assessment of myelination using time-dependent diffusion MRI indices". In: *International Symposium for Magnetic Resonance in Medicine (ISMRM) 2018*.

Almairac, F., P. Filipiak, L. Slabu, M. Clerc, T. Papadopoulo, D. Fontaine, L. Mondot, S. Chanelet, D. Wassermann, and R. Deriche (2018). "Bridging Brain Structure and Function by Correlating Structural Connectivity and Cortico-Cortical Transmission". In: *2nd C@ UCA meeting*.

Dockès, J., D. Wassermann, R. Poldrack, F. Suchanek, B. Thirion, and G. Varoquaux (2018). "Text to brain: predicting the spatial distribution of neuroimaging observations from text reports". In: *International Conference on Medical Image Computing and Computer-Assisted Intervention*. Springer, Cham, pp. 584–592.

Fick, R., D. Wassermann, and R. Deriche (2018b). "Mipy: An Open-Source Framework to improve reproducibility in Brain Microstructure Imaging". In: *OHBM 2018-Human Brain Mapping*, pp. 1–4.

Filipiak, P., R. Fick, A. Petiet, M. Santin, A.-C. Philippe, S. Lehéricy, R. Deriche, and D. Wassermann (2018b). "Spatio-Temporal dMRI Acquisition Design: Reducing the Number of Samples". In: *ISMRM 2018*.

Frigo, M., G. Gallardo, I. Constantini, A. Daducci, D. Wassermann, R. Deriche, and S. Deslauriers-Gauthier (2018). "Reducing false positive connection in tractograms using joint structure-function filtering". In: *OHBM 2018-Organization for Human Brain Mapping*.

Gallardo, G., N. T. Gayraud, R. Deriche, M. Clerc, S. Deslauriers-Gauthier, and D. Wassermann (2018a). "Solving the Cross-Subject Parcel Matching Problem Using Optimal Transport". In: *International Conference on Medical Image Computing and Computer-Assisted Intervention*. Springer, pp. 836–843.

Gallardo, G., B. Sylvain, and D. Wassermann (2018b). "Diffusion Driven Label Fusion for White Matter Multi-Atlas Segmentation". In: *OHBM 2018-Organization for Human Brain Mapping*.

Gayraud, N., G. Gallardo, M. Clerc, and D. Wassermann (2018). "Solving the Cross-Subject Parcel Matching Problem: Comparing Four Methods Using Extrinsic Connectivity". In: *OHBM 2018*.

Wassermann, D., V. D. Nguyen, G. Gallardo-Diez, J.-R. Li, W. Cai, and V. Menon (2018). "Sensing Spindle Neurons in the Insula with Multi-shell Diffusion MRI". In: *Annual Meeting ISMRM-ESMRMB, June 16-21 2018*. ISMRM-ESMRMB 2018.

Chen, L., D. Wassermann, J. Kochalka, and V. Menon (2017). "Concordance between white-matter pathways and functional circuits linking the VWFA and IPS". In: *Organisation for the Human Brain Mapping*.

Fick, R., A. Petiet, M. Santin, A.-C. Philippe, S. Lehericy, R. Deriche, and D. Wassermann (2017b). "Multi-Spherical Diffusion MRI: An in-vivo Test-Retest Study of Time-Dependent q-space Indices". In: *ISMRM: 25th Annual Meeting & Exhibition*.

Filipiak, P., R. Fick, A. Petiet-Bacarisse, M. Santin, A.-C. Philippe, S. Lehericy, R. Deriche, and D. Wassermann (2017). "Spatio-Temporal dMRI Acquisition Design: Reducing the Number of qτ-Samples Through a Relaxed Probabilistic Model". In: *MICCAI 2017 Workshop on Computational Diffusion MRI (CDMRI 2017)*.

Gallardo, G., R. Deriche, and D. Wassermann (2017a). "A Novel Atlas of Human Cerebral Cortex based on Extrinsic Connectivity". In: *OHBM 2017-Organization for Human Brain Mapping 2017 Annual Meeting*.

Gallardo, G., N. T. H. Gayraud, M. Clerc, and D. Wassermann (2017b). "Matching parcellations using Optimal Transport: a proof of concept". In: *Computational Brain Connectivity Mapping–Winter School Workshop 2017*.

Gallardo, G., D. Wassermann, R. Deriche, M. Descoteaux, and S. Deslauriers-Gauthier (2017c). "Information Flow in the White Matter During a Motor Task: A Structural Connectivity Driven Approach". In: *OHBM 2017 Organization for Human Brain Mapping Annual Meeting*.

Lascano, N., G. Gallardo-Diez, R. Deriche, D. Mazauric, and D. Wassermann (2017). "Extracting the Groupwise Core Structural Connectivity Network: Bridging Statistical and Graph-Theoretical Approaches". In: *International Conference on Information Processing in Medical Imaging*. Springer, Cham, pp. 373–384.

Philippe, A.-C., S. Lavault, R. Fick, D. Wassermann, R. Valabregue, R. Deriche, R. Levy, I. Arnulf, and S. Lehericy (2017). "Brain correlates of apathy in Kleine Levin syndrome: a mean apparent propagator study". In: *International Symposium for Magnetic Resonance in Medicine*.

Wassermann, D., D. Van Nguyen, G. Gallardo, J.-R. Li, W. Cai, and V. Menon (2017b). "Sensing Von Economo Neurons in the Insula with Multi-shell Diffusion MRI". In: *International Society for Magnetic Resonance in Medicine*.

Fick, R. H. J., M. Pizzolato, D. Wassermann, M. Zucchelli, G. Menegaz, and R. Deriche (2016a). "A sensitivity analysis of q-space indices with respect to changes in axonal diameter, dispersion and tissue composition". In: *2016 IEEE 13th International Symposium on Biomedical Imaging (ISBI)*. IEEE, pp. 1241–1244.

Fick, R., M. Daianu, M. Pizzolato, D. Wassermann, R. E. Jacobs, P. M. Thompson, T. Town, and R. Deriche (2016c). "Comparison of Biomarkers in Transgenic Alzheimer Rats Using Multi-shell Diffusion MRI". In: *MICCAI 2016 Workshop on Computational Diffusion MRI (CDMRI'16)*.

Fick, R., A. Petiet, M. Santin, A.-C. Philippe, S. Lehericy, R. Deriche, and D. Wassermann (2016d). "Multi-Spherical Diffusion MRI: Exploring Diffusion Time Using Signal Sparsity". In: *MICCAI 2016 Workshop on Computational Diffusion MRI (CDMRI'16)*.

Gallardo-Diez, G., R. Deriche, and D. Wassermann (2016). “Efficient Population-Representative Whole-Cortex Parcellation Based on Tractography”. In: *Organization for Human Brain Mapping (OHBM)*.

Gallardo, G., R. Fick, W. Wells, R. Deriche, and D. Wassermann (2016). “Groupwise Structural Parcellation of the Cortex: A Sound Approach Based on Logistic Models”. In: *International Conference on Medical Image Computing and Computer-Assisted Intervention*. Springer, pp. 99–112.

Girard, G., A. Daducci, L. Petit, J.-P. Thiran, K. Whittingstall, R. Deriche, D. Wassermann, and M. Descoteaux (2016a). “Reducing Invalid Connections with Microstructure-Driven Tractography”. In: *ISMRM workshops: Breaking the Barriers of Diffusion MRI*.

Girard, G., A. Daducci, K. Whittingstall, R. Deriche, D. Wassermann, and M. Descoteaux (2016b). “Microstructure driven tractography in the human brain”. In: *Organization for Human Brain Mapping (OHBM)*.

Wassermann, D., D. Mazauric, G. Gallardo-Diez, and R. Deriche (2016b). “Extracting the Core Structural Connectivity Network: Guaranteeing Network Connectedness Through a Graph-Theoretical Approach”. In: *International Conference on Medical Image Computing and Computer-Assisted Intervention*. Springer International Publishing, pp. 89–96.

Wassermann, D., A. Petiet, M. Santin, R. Fick, A.-C. Philippe, S. Lehericy, and R. Deriche (2016c). “Quantifying White Matter Microstructure with a Unified Spatio-Temporal Diffusion Weighted MRI Continuous Representation”. In: *International Symposium of Magnetic Resonance in Medicine*.

Fick, R., D. Wassermann, G. Sanguinetti, and R. Deriche (2015). “Laplacian-Regularized MAP-MRI: Improving Axonal Caliber Estimation”. In: *International Symposium on BIOMEDICAL IMAGING: From Nano to Macro*.

Girard, G., R. Fick, M. Descoteaux, R. Deriche, and D. Wassermann (2015). “AxTract: microstructure-driven tractography based on the ensemble average propagator”. In: *Information Processing in Medical Imaging*. Springer.

Scheer, T., F. Mathy, and D. Wassermann (2015). “Sahin et al.(2009) en modalité non-invasive: expérience pilote et perspectives”. In: *Journée de l’axe MTC-NSC*.

Wassermann*, D., R. Fick*, M. Pizzolato, and R. Deriche (2015a). “A Unifying Framework for Spatial and Temporal Diffusion in Diffusion MRI”. In: *Information Processing in Medical Imaging (IPMI)*.

Wassermann*, D., M. Pizzolato*, T. Boutelier, and R. Deriche (2015c). “Exploiting the Phase in Diffusion MRI for Microstructure Recovery: Towards Axonal Tortuosity via Asymmetric Diffusion Processes”. In: *Medical Image Computing and Computer Assited Intervention*.

Fick, R., D. Wassermann, G. Sanguinetti, and R. Deriche (2014). “An Analytical 3D Laplacian Regularized SHORE Basis and Its Impact on EAP Reconstruction and Microstructure Recovery”. In: *Computational Diffusion MRI*.

Garyfallidis, E., D. Wassermann, M. Descoteaux, et al. (2014). “Direct native-space fiber bundle alignment for group comparisons”. In: *International Society for Magnetic Resonance Imaging (ISMRM)*.

Ross, J. C., A. A. Díaz, Y. Okajima, D. Wassermann, G. R. Washko, J. Dy, and R. S. J. Estépar (2014). “Airway labeling using a hidden markov tree model”. In: *2014 IEEE 11th International Symposium on Biomedical Imaging (ISBI)*. IEEE, pp. 554–558.

Wassermann, D., J. Ross, G. Washko, W. M. Wells III, and R. S. Jose (2014a). "Deformable Registration of Feature-Endowed Point Sets Based on Tensor Fields". In: *Computer Vision and Pattern Recognition (CVPR)*.

Wassermann, D., M. Toews, M. Niethammer, and W. Wells III (2014b). "Probabilistic diffeomorphic registration: Representing uncertainty". In: *International Workshop on Biomedical Image Registration*. Springer International Publishing, pp. 72–82.

Princich, J., D. Wassermann, and S. Kochen (2013a). "Methodological Procedure to Identify Anatomical Location of Depth Electrodes in the Clinical Evaluation of Epilepsy Surgery Candidates Based on Open Source Software". In: *EPILEPSIA*. Vol. 54. WILEY-BLACKWELL, pp. 307–307.

Tunç, B., A. R. Smith, D. Wasserman, X. Pennec, W. M. Wells, R. Verma, and K. M. Pohl (2013). "Multinomial Probabilistic Fiber Representation for Connectivity Driven Clustering". In: *Information Processing in Medical Imaging*. Springer, pp. 730–741.

Wassermann, D., N. Makris, Y. Rathi, M. Shenton, R. Kikinis, M. Kubicki, and C.-F. Westin (2013a). "On describing human white matter anatomy: the white matter query language". In: *International Conference on Medical Image Computing and Computer-Assisted Intervention*. Springer, pp. 647–654.

Wassermann, D., J. Ross, G. Washko, C.-F. Westin, and R. S. J. Estépar (2013b). "Diffeomorphic point set registration using non-stationary mixture models". In: *2013 IEEE 10th International Symposium on Biomedical Imaging*. IEEE, pp. 1042–1045.

Wassermann, D., N. Makris, P. Pelavin, M. Shenton, M. Kubicki, C.-F. Westin, and R. Kikinis (2012). "Natural Language Queries for White Matter Identification: the White Matter Query Language (WMQL)". In: *Organization for the Human Brain Mapping*.

Barttfeld, P., J. Calvar, S. Cukier, R. Deriche, R. Leiguarda, S. Navarta, M. Sigman, D. Wassermann, and B. Wicker (2011). "Large-scale network analysis reflects big-world characteristics in ASD". In: *Human Brain Mapping*.

Forsberg, D., Y. Rathi, S. Bouix, D. Wassermann, H. Knutsson, and C.-F. Westin (2011). "Improving registration using multi-channel diffeomorphic demons combined with certainty maps". In: *Multimodal Brain Image Analysis*. Springer Berlin/Heidelberg, pp. 19–26.

Ghosh, A., D. Wassermann, and R. Deriche (2011). "A polynomial approach for maxima extraction and its application to tractography in HARDI". In: *Biennial International Conference on Information Processing in Medical Imaging*. Springer, Berlin, Heidelberg, pp. 723–734.

Wassermann, D., A.-C. Philippe, P. Barttfeld, B. Wicker, M. Sigman, and R. Deriche (2011a). "Tract-based statistical analysis in dMRI in autism spectrum disorder". In: *Human Brain Mapping*.

Wassermann, D., Y. Rathi, S. Bouix, M. Kubicki, R. Kikinis, M. Shenton, and C.-F. Westin (2011b). "White matter bundle registration and population analysis based on Gaussian processes". In: *Biennial International Conference on Information Processing in Medical Imaging*. Springer Berlin Heidelberg, pp. 320–332.

Wassermann, D., P. Savadjiev, Y. Rathi, R. Kikinis, S. Bouix, M. Kubicki, M. Shenton, and C.-F. Westin (2011c). "Cluster-Based Statistics Along White Matter Tracts". In: *International Symposium of Magnetic Resonance in Medicine*.

Wassermann, D., J. Cohen-Adad, S. Lehericy, H. Benali, S. Rossignol, and R. Deriche (2010b). "Fully Automated Straightening of the Spinal Cord using Fiber Tractography". In: *International Symposium of Magnetic Resonance in Medicine*. Vol. 1. 18th.

– (2010c). "Straightening the spinal Cord using fibre tractography". In: *2010 IEEE International Symposium on Biomedical Imaging: From Nano to Macro*. IEEE, pp. 1377–1380.

Wassermann, D., E. Kanterakis, R. C. Gur, R. Deriche, and R. Verma (2010d). "Diffusion-based population statistics using tract probability maps". In: *International Conference on Medical Image Computing and Computer-Assisted Intervention*. Springer, Berlin, Heidelberg, pp. 631–639.

Wassermann, D., L. Bloy, R. Verma, and R. Deriche (2009a). "A gaussian process based framework for white matter fiber tracts and bundles, applications to fiber clustering". In: *Proceedings Medical Image Computing and Computer Aided Intervention (MICCAI Workshop), London*, pp. 200–214.

– (2009b). "Bayesian framework for white matter fibers similarity measure". In: *2009 IEEE International Symposium on Biomedical Imaging: From Nano to Macro*. IEEE, pp. 815–818.

Delmaire, C., M. Vidailhet, M. Descoteaux, D. Wassermann, F. Bourdain, C. Lenglet, S. Sangla, A. Terrier, R. Deriche, and S. Lehéricy (2008). "Diffusion tensor imaging of white matter abnormalities in patients with writer's cramp". In: *Proc. Intl. Soc. Mag. Reson. Med*. Vol. 16, p. 2161.

Wassermann, D., R. Deriche, et al. (2008a). "Simultaneous manifold learning and clustering: Grouping white matter fiber tracts using a volumetric white matter atlas". In: *MICCAI 2008 Workshop-Manifolds in Medical Imaging: Metrics, Learning and Beyond*.

Wassermann, D., M. Descoteaux, and R. Deriche (2007a). "Diffusion maps segmentation of magnetic resonance q-ball imaging". In: *2007 IEEE 11th International Conference on Computer Vision*. IEEE, pp. 1–8.

Wassermann, D. and M. Mejail (2005). "Development and validation of an algorithm for cardiomyocyte beating frequency determination". In: *Iberoamerican Congress on Pattern Recognition*. Springer Berlin Heidelberg, pp. 420–430.

Wassermann, D., A. Katz, J. Gambini, J. Jacobo, and M. Mejail (2004a). "Real Time Object Tracking for the MiroSOT League Robot Football: a B-spline Active Contours Approach". In: *Federation of International Robot-soccer Association*.

Wassermann, D., M. E. Mejail, J. Gambini, and M. E. Buemi (2004b). "Segmentation with active contours: a comparative study of B-Spline and Level Set techniques". In: *Proceedings. 17th Brazilian Symposium on Computer Graphics and Image Processing*. IEEE, pp. 98–105.

Acronyms

AABB axis-aligned boundary box

AHC agglomerative hierarchical clustering

AF arcuate fascicle

CAG cytosine-adenine-guanine

CCA canonical correlation analysis

dAI dorsal-anterior insula

CDT conventional streamline tractography

CST cortico-spinal tract

dMRI diffusion weighted magnetic resonance imaging

DSL domain specific language

DTI diffusion tensor imaging

DWI diffusion weighted image

EAP ensemble average propagator

EC extrinsic connectivity

Ec extreme capsule fascicle

FC functional connectivity

HARDI high angular resolution dMRI

HD Huntington's disease

IOFF inferior occiptio-frontal fascicle

ILF inferior-longitudinal fascicle

fMRI functional MRI

FWHM full witdh at half maximum

GLM generalized linear model

GPA Gaussian phase approximation

HCP human connectome project

MAPL laplacian-regularised mean apparent propagator imaging

MAP mean apparent propagator imaging

MdLF middle longitudinal fascicle

MRI magnetic resonance imaging

MSD mean squared displacement

NMR nuclear magnetic resonance

NPA narrow pulse approximation

PI posterior insula

RTAP return to axis probability

RTOP return to origin probability

RTPP return to plane probability

vAI ventral-anterior insula

VEN Von Economo neuron

WMQL white matter query language

ODF orientation distribution function

ROI region of interest

RT reaction time

SGA standard genetic algorithm optimization

SLF I superior longitudinal fascicle I

SNR signal-to-noise ratio

STD standard deviation

UF uncinate fascicle